



HAL
open science

Polarized positron sources for the future linear colliders

Iryna Chaikovska

► **To cite this version:**

Iryna Chaikovska. Polarized positron sources for the future linear colliders. Other [cond-mat.other].
Université Paris Sud - Paris XI, 2012. English. NNT : 2012PA112358 . tel-00795937

HAL Id: tel-00795937

<https://theses.hal.science/tel-00795937>

Submitted on 1 Mar 2013

HAL is a multi-disciplinary open access archive for the deposit and dissemination of scientific research documents, whether they are published or not. The documents may come from teaching and research institutions in France or abroad, or from public or private research centers.

L'archive ouverte pluridisciplinaire **HAL**, est destinée au dépôt et à la diffusion de documents scientifiques de niveau recherche, publiés ou non, émanant des établissements d'enseignement et de recherche français ou étrangers, des laboratoires publics ou privés.

Université Paris-sud 11

Ecole Doctorale Particules, Noyaux et Cosmos - ED 517
Laboratoire de l'Accélérateur Linéaire - UMR 8607

Discipline: Physique des Particules et Accélérateurs

THÈSE DE DOCTORAT

présentée par

Iryna CHAIKOVSKA

Polarized positron sources for the future linear colliders

Sources de positrons polarisés pour les futurs collisionneurs
linéaires

Soutenue le 10 décembre 2012 devant le Jury composé de:

M.	Alessandro Variola	Directeur de thèse
M.	Achille Stocchi	Président du Jury
Mme.	Maud Baylac	Rapporteur
M.	Frank Zimmermann	Rapporteur
M.	Fabian Zomer	Examineur
M.	Luca Serafini	Examineur
M.	Tsunehiko Omori	Examineur

Abstract

During the next few years experiments at the Large Hadron Collider (LHC) at CERN will continue to explore carefully fundamental high energy physics principles at a an energy domain which has never been reached before. Possible designs for the next-generation lepton Linear Collider (LC) based on $e^+ - e^-$ collisions have already been proposed to perform high precision studies complementary to the LHC. In this framework, there are two large projects: the International Linear Collider (ILC) exploring a centre-of-mass energy range of $\sqrt{s} = 0.5 - 1$ TeV and the Compact Linear Collider (CLIC) expected to operate at $\sqrt{s} = 0.5 - 3$ TeV. The physics programme of the future LC will benefit strongly of colliding both polarised electron and positron beams.

This thesis introduces the polarized positron source as one of the key element of the future LC. In this context, the different schemes of the polarized positron source are described highlighting the main issues in this technology. In particular, the main focus is on the Compton based positron source adopted by the CLIC as a preferred option for the future positron source upgrade. In this case, the circularly polarized high energy gamma rays resulting from Compton scattering are directed to a production target where an electromagnetic cascade gives rise to the production of positrons by $e^+ - e^-$ pair conversion. To increase the efficiency of the gamma ray production stage, a multiple collision point line integrated in energy recovery linac is proposed. The simulations of the positron production, capture and primary acceleration allow to estimate the positron production efficiency and provide a simple parametrization of the Compton based polarized positron source in the view of the future LC requirements.

The storage ring based Compton source option, so-called Compton ring, is also described. The main constraint of this scheme is given by the beam dynamics resulting in the large energy spread and increased bunch length affecting the gamma ray production rate. An original theoretical contribution is shown to calculate the energy spread induced by Compton scattering.

Moreover, an experiment to test the gamma ray production by Compton scattering using a state-of-art laser system developed at LAL has been conducted in the framework of the “MightyLaser” project at the ATF, KEK. The experimental layout as well as the main results obtained are discussed in details.

The studies carried out in this thesis show that the polarized positron source based on Compton scattering is a promising candidate for the future LC polarized positron source. To attain the required performance, further developments and R&D in field of the high power laser systems, optical cavities and high current electron accelerators such as the energy recovery linacs should be pursued in the future.

Keywords : Future Linear Collider, International Linear Collider (ILC), Compact LInear Collider (CLIC), Polarized Positron Source, Compton Scattering.

Résumé

Au cours des prochaines années les expériences au grand collisionneur de hadrons (LHC) au CERN vont explorer méticuleusement les lois fondamentales de la physique des hautes énergies à une énergie qui n'a jamais été atteinte auparavant. Afin de compléter les recherches du LHC, plusieurs projets de collisionneur linéaire (CL) de lepton de prochaine génération utilisant des collisions $e^+ - e^-$ ont été proposés pour permettre des études de haute précision. Dans ce cadre il existe deux grands projets: le collisionneur linéaire international (ILC) pour explorer une plage d'énergie dans le centre de masse de $\sqrt{s} = 0.5 - 1$ TeV et le collisionneur linéaire compact (CLIC) qui devrait fonctionner à $\sqrt{s} = 0.5 - 3$ TeV. Le programme de physique du futur CL profitera grandement de collisions où les deux faisceaux seront polarisés.

Cette thèse présente la source de positrons polarisés qui est un élément clef du futur CL. Dans ce contexte, les différents concepts de source de positrons polarisés sont présentés en mettant en avant les principaux défis technologiques. Plus spécifiquement, le centre d'intérêt principal est sur la source de positrons Compton adoptée par CLIC comme option préférée pour l'amélioration de la future source de positrons. Dans cette source, les rayons gamma de haute énergie produits par diffusion Compton sont envoyés sur une cible où les interactions électromagnétiques produisent des positrons dans des paires $e^+ - e^-$. Pour améliorer l'efficacité de l'étape de production de rayons gamma, une ligne de multiples points de collisions est proposée intégrée à un linac à récupération d'énergie. Les simulations de la production de positrons, de leur capture et de leur accélération initiale permettent d'estimer l'efficacité de production de positrons et de fournir une paramétrisation simple de la source de positrons polarisés basée sur l'interaction Compton dans la perspective des besoins futurs du CL.

L'option d'une source Compton basée sur un anneau de stockage appelé anneau Compton est aussi décrite. La principale contrainte de ce concept provient de la dynamique faisceaux à cause de la grande dispersion en énergie et l'augmentation de la longueur du paquet ce qui affecte le taux de production des rayons gamma. Une contribution théorique originale est présentée pour calculer la dispersion en énergie induite par la diffusion Compton.

De plus, une expérience pour tester la production de rayons gamma par diffusion Compton en utilisant un système laser au fait de la technologie et développ au LAL est en cours dans le cadre du projet "MightyLaser" à l'ATF, KEK. La configuration expérimentale ainsi que les résultats principaux obtenus sont discutés en détails.

Les recherches décrites dans cette thèse montrent que la source de positrons polarisés basée sur la diffusion Compton est un candidat prometteur pour la source de positrons polarisés du futur CL. Pour atteindre les performances requises des travaux supplémentaires et de la R&D sont nécessaires dans le domaine des lasers de puissance, des cavités optiques et des accélérateurs d'électrons à fort courant tels que les linacs à récupération d'énergie.

Mots clés : Le futur collisionneur linéaire, le Collisionneur Linéaire International (ILC), le Collisionneur Linéaire Compact (CLIC), sources de positrons polarisés, diffusion Compton.

Acknowledgements

First and foremost, my utmost gratitude to my thesis adviser. It is with immense gratitude that I acknowledge the support and help of Alessandro Variola. It has been an honor to be his first PhD student. Without his guidance and persistent help this dissertation would not have been possible. I definitely can say that I am glad to work with him as he is a good example of a successful physicist and a very nice personality. Every time I see him, a smile comes on my face, this mystery will always remain unsolved for me. There are still a lot of things that I would like to learn from him.

I would like to thank the reviewers Maud Baylac and Frank Zimmermann who kindly agreed to read this manuscript, their comments were very helpful and very much appreciated. I also grateful to the other members of my committee, Achille Stocchi, Tsunehiko Omori, Luca Serafini and Fabian Zomer whose contribution cannot be overestimated.

I am indebted to my many colleagues who supported me. I would like to express my sincere appreciation to Nicolas Delerue for his help, support, encouragement and friendly guidance. I especially appreciate the discussions and advices of Robert Chehab and Olivier Dadoun. I definitely share the credit of my work with them and I am sorry that sometimes their contribution to my work may seem underestimated.

I would like to thank our japanese colleagues from ATF, KEK for a possibility to use their facilities, consultations, help with experimental set-up and general advices.

I am grateful to all my friends. I am especially indebted to Leonid and Valentyna whose help and support I felt every day.

Last but not the least, I would like to thank my family for all their love and encouragement during all these years. To my parents who supports

me in all my pursuits, thank you. To my sister Olga who is always near and whose support is indispensable to me. To my loving, supportive and patient husband, who was the one who was there for me during the thesis period, whose faithful support especially during the final stage of the PhD is so appreciated... Thank you!!!

Contents

List of Figures	vii
List of Tables	xi
1 Introduction	1
1.1 Physics case for the future linear collider	1
1.2 Polarization as an important tool for the future LC	3
1.3 Future linear collider projects: ILC and CLIC	6
2 Positrons and polarized positrons	11
2.1 Discovery of positron	11
2.2 Polarization formalism. Photon and electron polarization.	12
2.3 Polarized electrons and positrons for ILC/CLIC	17
2.3.1 Polarized electrons	17
2.3.2 Polarized positrons	19
2.4 Radiative polarization (selfpolarization)	22
2.5 Undulator based polarized positron source	23
2.6 Compton based polarized positron source	26
3 Theoretical introduction for innovative schemes	31
3.1 Compton effect	31
3.1.1 Thomson and Compton scattering	31
3.1.2 Kinematics of the Compton scattering	33
3.1.2.1 Feynman diagrams. Scattering amplitude.	33
3.1.2.2 Compton cross section	34
3.1.2.3 Energy boost of the low energy photons	40

CONTENTS

3.1.2.4	Polarized Compton cross section	43
3.2	Low energy applications of the Compton scattering	49
3.2.1	X- and gamma rays	49
3.2.2	Application fields	50
3.3	Production schemes for the polarized positron sources	52
3.3.1	Compton ring. Dynamical and equilibrium energy spread.	55
3.3.2	Compton ring. Polarized and unpolarized equilibrium energy spread by Campbell's theorem.	57
3.3.3	ERL solution. Multiple Interaction Point Line.	61
4	Positron source performance	69
4.1	Why positron sources are critical components of the future linear colliders?	69
4.2	Positron production	71
4.2.1	Positron target effects and limits	71
4.2.2	Positron production simulations. The CLIC case.	73
4.3	Capture system and primary acceleration	78
4.4	Impact of the results on the Compton based polarized positron source	84
5	Experiment: MightyLaser at KEK	87
5.1	Description of the experiment: a gamma ray factory	87
5.2	Accelerator Test Facility at KEK	88
5.2.1	General overview of the ATF	88
5.2.2	Electron beam diagnostics in the ATF DR	90
5.3	State-of-the-art of lasers and Fabry-Perot cavities	93
5.3.1	Laser for the Fabry-Perot cavity	93
5.3.2	Four mirror Fabry-Perot cavity	95
5.4	The IP physics	98
5.4.1	Expected gamma ray flux and energy spectrum	98
5.4.2	Position sensitivity	101
5.5	The gamma ray detector	103
5.5.1	Geant4 simulations	105
5.5.2	Data acquisition system	108
5.5.3	Calibration	110
5.6	Data analysis and results	113

CONTENTS

5.6.1	Scanning procedure and the first data	113
5.6.2	Data taking and an example of the data	115
5.6.3	Data analysis technique	116
5.6.4	Laser power stored in the FPC	121
5.6.5	Results and discussion	124
5.6.6	Data - simulations comparison	130
5.7	Effect of the Compton scattering on the electron beam dynamics at the ATF DR	132
5.7.1	Simulation procedure	132
5.7.2	Results and discussion	133
5.8	Perspectives	137
6	Conclusion	139
	References	143

CONTENTS

List of Figures

1.1	Cross sections for different production mechanisms for 125 GeV Higgs boson	3
1.2	Contour plot of the effective polarization.	5
1.3	A schematic view of the CLIC	6
1.4	A schematic layout of the ILC complex	7
2.1	Undulator radiation properties.	25
2.2	A fundamental scheme of the polarized positron production by Compton scattering.	27
3.1	Geometry for the Thomson and Compton scattering in the rest frame of the electron	32
3.2	Thomson differential cross section	33
3.3	Feynman diagrams for the lowest order terms in the Compton Scattering cross section	34
3.4	Compton differential cross section in the rest frame of reference	36
3.5	The kinematics of the Compton scattering in the center of mass reference frame	37
3.6	The kinematics of Compton scattering in the laboratory frame	38
3.7	Differential Compton cross section versus the observation angle	39
3.8	Total unpolarized Compton cross section	40
3.9	Energy of the scattered high energy photons	42
3.10	Energy of scattered high energy photons for the "head-on" and orthogonal collision geometry	43

LIST OF FIGURES

3.11	Differential Compton cross section for different energies and polarization configurations (energy spectrum)	45
3.12	Differential Compton cross section for different energies and polarization configurations (angular spectrum)	46
3.13	The degree of circular polarization of the scattered photons for different polarization configurations	48
3.14	Multiple Interaction Point Line	61
3.15	Evolution of the betatron function along the MIPL consisting of 5 IPs.	63
3.16	“Statistical card” of the CAIN simulation	64
3.17	Gamma ray flux and the electron energy distribution for the Multiple Interaction Point Line	65
3.18	The collimator efficiency and polarization as a function of the collimator diameter. The computed energy spectrum of the scattered gamma rays.	66
3.19	Polarization distribution of the scattered gamma rays	67
4.1	Gamma ray total cross sections as a function of energy in carbon and lead	72
4.2	Fractional energy loss per radiation length in lead as a function of electron or positron energy	73
4.3	A fundamental scheme of the positron production	74
4.4	Optimization of the target-converter thickness	75
4.5	Energy deposition pattern in the target-converter	75
4.6	Distribution of the positrons produced	76
4.7	A fundamental scheme of the positron capture and primary acceleration	78
4.8	Magnetic and electric field profiles in the ACS	79
4.9	Positron beam emittance taken at the exit of the target, at the exit of the AMD and at the end of the accelerating capture section (ACS)	79
4.10	Longitudinal distributions of the positrons at the end of the pre-injector linac inside the (± 10 MeV, ± 10 mm) window	81
4.11	Layout of the Compton based polarized positron source	83
4.12	Efficiency of the Compton based polarized positron source	86
5.1	Layout of the Accelerator Test Facility at KEK	89
5.2	Illustration of the ATF running conditions	90
5.3	Beam Position Monitor readings during the data taking	92

LIST OF FIGURES

5.4	Optical system used for the laser power amplification and to inject the laser beam to the FPC	94
5.5	Illustration of the rapid advance in power of the fiber lasers	94
5.6	Vacuum vessel for the Fabry-Perot cavity installed at the ATF	96
5.7	Dependence of the number of the gamma rays produced on the collision angle	97
5.8	Expected energy spectrum and production rate of the gamma rays . . .	100
5.9	Dependence of the gamma ray production rate on the laser pulse offset and time delay with respect to the electron bunch for the nominal parameters.	102
5.10	Emission spectrum of BaF ₂ and transmittance of the UV-filter	103
5.11	Development of an electromagnetic shower in the BaF ₂ calorimeter . . .	105
5.12	Interaction of the gamma rays inside the BaF ₂ calorimeter	106
5.13	The distribution of the optical photons produced in the BaF ₂ calorimeter	107
5.14	Energy deposited in the scintillator and the optical photon distribution at the PMT	107
5.15	Layout of the data acquisition system	109
5.16	Schematic layout of the calibration setup	110
5.17	Calibration of the gamma ray detector	111
5.18	Illustration of the correction factors used for the calibration	112
5.19	Example of signal observed on the oscilloscope while scanning the parameters space to find the collision area	113
5.20	Vertical position scan	114
5.21	The typical signal shape for the high energy gamma rays produced by Compton scattering observed at the anode output of the PMT	115
5.22	Example of the stacking of the 924 ns periods	116
5.23	Illustration of the peak height distribution	117
5.24	Illustration of the quality cuts together with their effect on the data sample	119
5.25	Example of the data file having the turn by turn background	120
5.26	Signal waveform of the laser power stored in the FPC	121
5.27	Illustration of the laser power stored in the FPC	122
5.28	Distribution of the laser power stored in the FPC	123
5.29	Spectrum of the gamma rays produced for all laser powers	124

LIST OF FIGURES

5.30	Gamma ray spectrum for different FPC stored laser power	125
5.31	Illustration of the data taken during the multibunch ATF run	126
5.32	Part of the data file containing the highest energy deposited in the calorimeter per one shot which is about 904 MeV	127
5.33	Illustration of three data files containing the highest integrated flux over 0.2 ms for different ATF DR filling modes	129
5.34	Distribution of the number of the optical photons expected in the exper- iment	131
5.35	Comparison between the measured and simulated energy spectra of the gamma rays resulting from the Compton scattering	131
5.36	Evolution of the longitudinal phase space of one electron bunch at the ATF DR with Compton scattering	135
5.37	Results of the longitudinal beam dynamics simulations of the ATF DR .	136

List of Tables

1.1	Main CLIC parameter set	8
1.2	Main ILC parameter set	9
2.1	Comparison of Stokes parameters and electron polarization vector.	18
3.1	The Compton IP parameters used for the MIPL simulation	62
3.2	Parameters of one cell of the Multiple Interaction Point Line	63
3.3	Parameters of the produced gamma ray distribution	67
4.1	The parameters and the results of the positron production simulation	77
4.2	The parameters of the ACS used for the positron capture and primary acceleration simulation	82
4.3	Positron beam parameters at the exit of the AMD and the pre-injector linac	82
5.1	Laser system parameters	98
5.2	ATF DR parameters	99
5.3	Main parameters of the gamma ray detector	104
5.4	Highest integrated gamma ray flux achieved.	128
5.5	Results of the longitudinal beam dynamics simulation of the ATF DR.	134

LIST OF TABLES

1

Introduction

1.1 Physics case for the future linear collider

Nowadays, the experiments at CERN Large Hadron Collider (LHC) are exploring an energy range which has never been reached before. The LHC was built as a discovery machine to investigate the phenomena in the field of Higgs physic and the different scenarios beyond the Standard Model (SM), such as supersymmetry, extra space-time dimensions and quantum gravity, dark matter, superstrings, etc..

As far as the hadron collider is concerned the center-of-mass available energy is not precisely known, the effective energy being lower than that of the initial proton beams. This comes from the fact that the protons are composed by quarks which are bound together by gluons and therefore, during the proton–proton collisions, the initial proton energy is distributed among the constituents by a not well-known ratio. The uncertainty in energy makes such machines versatile for new phenomena searches but also more complex due to the high backgrounds, complicated decay schemes resulting in low precision of the measurements.

Nevertheless, the results obtained have to be studied with the higher precision possible and therefore the High Energy Physics (HEP) community is carrying out an intense research program to propose the next-generation collider, which will use electrons (e^-) and positrons (e^+). In general, an advantage of the lepton machines is that the center-of-mass energy is exactly given by the sum of the two beam energies since the leptons are the elementary particles undergoing the single-particle interactions compared to the hadrons. Furthermore, in this case the low backgrounds allows the

1. INTRODUCTION

comprehensive precise measurements complementary to the LHC.

Nevertheless, according to the experience of the Large Electron Positron circular collider (LEP) operated in CERN, at high e^-/e^+ beam energies the synchrotron radiation starts to be a limit concerning performance and cost of the RF system. Moreover, the high intensity of the emitted radiation has a strong impact on the dynamical vacuum of the machine. In such a way, at LEP for 104 GeV energy, around 3% of the beam energy was lost by synchrotron radiation in one turn of the machine [1]. Recently, a very challenging design of a circular $e^+ - e^-$ collider using the same LHC tunnel or a longer one has been proposed [2].

Knowing that the energy loss by synchrotron radiation increases with the energy ($\Delta E_{SR} \sim E^4$), an extension of $e^+ - e^-$ collider to high energies (~ 1 TeV) should require two linear accelerators to drive the beams to the nominal energy to avoid the significant synchrotron radiation that would occur in a ring.

In this context, the next-generation accelerator should be a Linear Collider (LC). Moreover, the LC brings additional advantage of keeping a very high polarization degree of the initially polarized beams in opposite to the storage ring where the polarization decrease significantly with the increase of the beam energy [3]. The observed energy dependence of radiative spin polarization at LEP showed a transverse beam polarization of 57% at 44.7 GeV and only 8% at 60.6 GeV.

The physics case for the future LC is provided by analyzing the main reactions in different physics scenarios given in details in [4, 5, 6]. It is mainly focused on the discoveries of the LHC experiments, precise measurements of the Higgs sector, precision top quark studies, precision electroweak measurements, New Physics searches. In this context, polarization of both beams at the future LC combined with a clean experimental environment will provide a powerful tool to accomplish a program planned and deepen the knowledge about the fundamental interactions. At present, the observation at the LHC of the new particle compatible with a Higgs boson with mass 125 GeV [7, 8] confirms the physics case for the LC [9].

In this framework, at present, there are two large projects: the International Linear Collider (ILC) [10, 11] with a nominal center-of-mass energy of 500 GeV with a possible upgrade to 1 TeV; and the Compact Linear Collider (CLIC) [12] with a nominal center-of-mass energy of 3 TeV (with a first energy stage at 500 GeV). The centre-of-mass energy range of the future LC projects allows the comprehensive analysis of physics a

1.2 Polarization as an important tool for the future LC

programme planned for the LC to be done. In such a way, for low energy phase (250–500 GeV) it allows the study of ZH , $t\bar{t}$, HHZ thresholds whereas for a high energy scenario (> 500 GeV) it implies the high statistics study of Higgs boson through WW fusion process and other rare Higgs production processes such as $e^+e^- \rightarrow HH\nu_e\bar{\nu}_e$. As an example, the illustration of different production mechanisms for 125 GeV Higgs boson at the future LC can be seen on Fig. 1.1. In such a way, the two major production processes are a Higgs-strahlung $e^+e^- \rightarrow HZ$ and WW fusion $e^+e^- \rightarrow H\nu_e\bar{\nu}_e$. The high energy runs will be also dedicated to the studies of the physics beyond the SM, etc. [9].

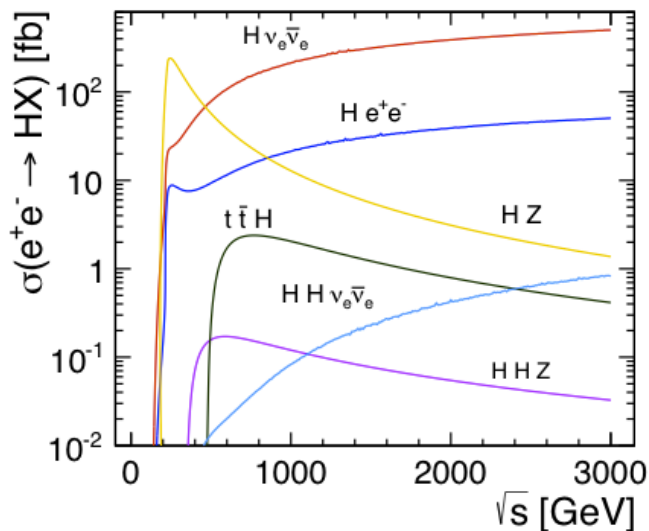


Figure 1.1: Cross sections for different production mechanisms for 125 GeV Higgs boson - given as a function of the electron-positron center-of-mass energy \sqrt{s} [13].

1.2 Polarization as an important tool for the future LC

The necessity of using polarized beams at the future LC, especially the polarized positron beam, has been comprehensively analyzed in [6]. Here, the main issues are summarized and listed:

- *Enhancement of the effective luminosity and the effective polarisation.* With longitudinally polarized beams, when the electron and the positron annihilate into a vector particle (e.g. $e^+e^- \rightarrow \gamma/Z$), cross sections at the future LC can be written

1. INTRODUCTION

as

$$\begin{aligned}\sigma_{P_{e^-}P_{e^+}} &= (1 - P_{e^-}P_{e^+})\frac{\sigma_{RL} + \sigma_{LR}}{4}\left(1 - \frac{P_{e^-} - P_{e^+}}{1 - P_{e^+}P_{e^-}}\frac{\sigma_{RL} - \sigma_{LR}}{\sigma_{RL} + \sigma_{LR}}\right) = \\ &= (1 - P_{e^-}P_{e^+})\sigma_0(1 - P_{eff}A_{LR}),\end{aligned}\quad (1.1)$$

where σ_0 is a unpolarized cross section, $P_{eff} = (P_{e^-} - P_{e^+})/(1 - P_{e^+}P_{e^-})$ is the effective polarization and $A_{LR} = (\sigma_{RL} - \sigma_{LR})/(\sigma_{RL} + \sigma_{LR})$ is the left-right asymmetry. By introducing the effective luminosity as

$$\mathcal{L}_{eff} = \frac{1}{2}(1 - P_{e^-}P_{e^+})\mathcal{L},\quad (1.2)$$

the Eq. 1.1 can be rewritten in the following form:

$$\sigma_{P_{e^-}P_{e^+}} = 2\sigma_0\frac{\mathcal{L}_{eff}}{\mathcal{L}}(1 - P_{eff}A_{LR}).\quad (1.3)$$

As one can see, the term $(1 - P_{e^-}P_{e^+})$ is responsible for the effective luminosity increase. Thus, the enhancement of the cross sections is observed if both beams are polarized and if P_{e^-} and P_{e^+} have different signs. Moreover, from Eq. 1.1 one can see that the large values of P_{eff} can be achieved in the case of the negative sign for the product $(P_{e^+}P_{e^-})$. Fig. 1.2 shows a plot of effective polarization with respect to the polarization of electron and positron beams. For example, the positron polarization of 30% together with the -70% of electron polarization result in $P_{eff} \approx -80\%$ (see Fig. 1.2).

- *Increase in precision of the measurements.* As an experiment, the left-right asymmetry A_{LR} is one of the quantities that should be extracted. Here, by using two polarized beams, the contribution to the error in A_{LR} due to the uncertainty of the polarization measurement can be reduced. In this context, the importance of the polarized electron beam for the SLD experiment at the SLAC LC (e.g. accurate measurement of a weak mixing angle $\sin^2\theta_W$ by using the polarized electron beam) is described in [14]. In this framework, a so-called GigaZ option of the LC is very interesting. It implies a high luminosity Z factory by running the accelerator at the Z boson resonance or at WW threshold. Polarization of the positron and electron beams in this case enhances a precision of the weak mixing angle measurement by two orders of magnitude through studies of the left-right asymmetry [6].

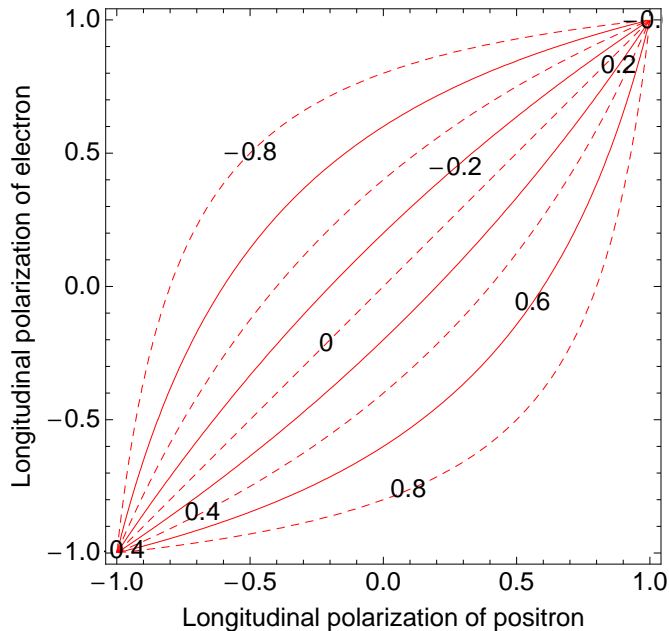


Figure 1.2: Contour plot of the effective polarization. - Contour plot $P_{eff} = \text{const}$ in the (P_{e+}, P_{e-}) plane. In order to maximize the P_{eff} two beam polarizations should have the opposite sign.

- *Suppressing background processes and signal enhancement by choosing the appropriate polarization configuration of two beams.* A signal to background ratio can be increased by using two polarized beams compared with the case of polarized electrons only. As an example of signal enhancement, for the light version of Higgs boson ~ 130 MeV (see Fig. 1.2), the two main production channels could have a similar production cross-sections. In this case beam polarization can help to distinguish between these processes. The separation is improved by a factor of about 4 by using $(P_{e-}, P_{e+}) = (+80\%, -60\%)$ with respect to the case with only right-handed polarized electrons. Moreover, a factor of 2 can be gained from suppression of the WW background by using a right-handed electron polarization [6].
- *An advantages of having both beams polarized simultaneously provides the versatile methods to search for New Physics.* In this case, the possible discoveries made at the LHC can be studied in a clean experimental environment together with the direct discoveries made at the LC. Another possibility to reveal New Physics

1. INTRODUCTION

is the discoveries made through the high precision measurements involving already known particles. New Physics can be observed though the virtual effects in processes involving SM particle only. For such indirect searches the production threshold is not an issue, the main point in this scenario is a high precision [9]. For this, GigaZ operation mode can provide the high precision measurements increasing sensitivity to search for New Physics in a model independent way.

1.3 Future linear collider projects: ILC and CLIC

A common feature of future LC designs (ILC and CLIC) is the requirement to provide a low emittance high current electron and positron beams to reach a high luminosity in the IP. Polarization is mandatory for the electron beam while it is an option for the positron beam. The fundamental schemes of the CLIC and the ILC are respectively shown on Fig. 1.3 and 1.4.

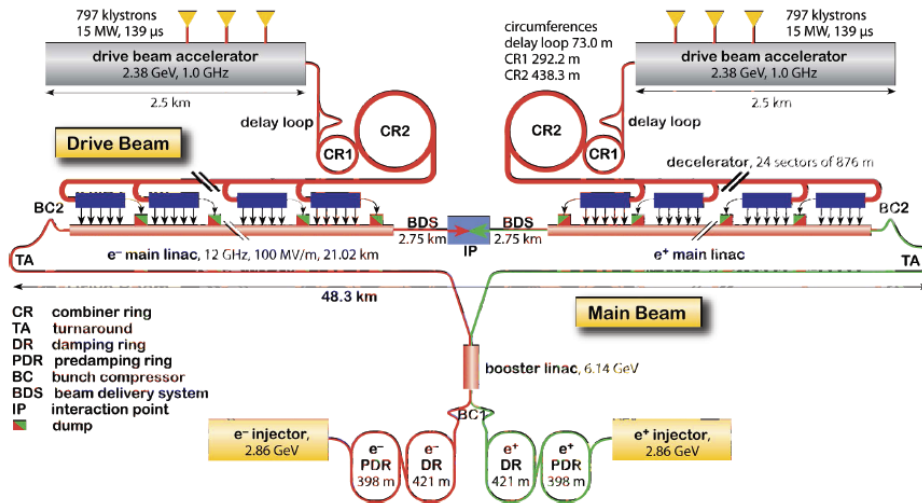


Figure 1.3: A schematic view of the CLIC - the electron and possibly positron beams are produced in the separate injector complexes, accelerated in the main linac to the nominal energy and focused in the IP where the $e^+ - e^-$ collisions take place.

Both LC projects share a similar design scheme: the key point of the two projects is the injector complex, it consists of the electron and the positron sources. First of all, they generate the polarized high current beams. After the production the beams are pre-accelerated and then injected in the main injector linac used to bring the beams to

1.3 Future linear collider projects: ILC and CLIC

the DR energy. The main goal of the DR is to cool the electron and positron beams to the very low emittance required for the collisions during the relatively short time. After being extracted from the DR the two beams are injected to the high gradient main linacs which bring them to the nominal energy preserving the low emittance. The Beam Delivery System (BDS) is then used to focus the electron and positron beams to nanometer transverse size and after the collisions to transport the beams to the main beam dumps.

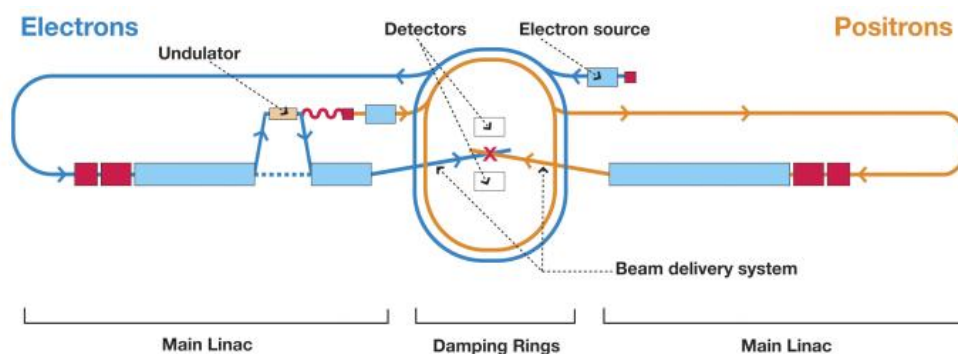


Figure 1.4: A schematic layout of the ILC complex - the electron beam produced and accelerated up to ~ 150 GeV is used in an undulator-based positron source driven by the main electron beam. The damped and accelerated positron beam then collides with the electron beam in the IP.

For both colliders the electron beam is produced by a laser illuminating a strained GaAs photocathode in a DC gun, providing 80-90% polarisation degree. During the pre-acceleration, the beam obtains the proper time structure and is injected in the DR at 5 GeV in the case of ILC and at 2.86 GeV for the CLIC to be injected into the DR. The ILC design foresees the electron and positron DRs with a circumference of 3.2 km each, operated at 5 GeV and housed in a single tunnel. The beam pulses have to be damped (e.g. by five orders of magnitude for the positron vertical emittance) within the 200 ms. The CLIC collaboration includes in the baseline four rings: a Pre-Damping Ring (pre-DR) and a main DR for both the electrons and the positrons. This configuration is needed to damp a large initial emittance (by two orders of magnitudes for the electron vertical emittance and by six orders of magnitude for that of the positrons) at the high repetition rate of 50 Hz [12].

The main differences between the ILC and CLIC projects come from the main accelerating technology and the positron source design. In this context, the ILC accelerating

1. INTRODUCTION

scheme is based on the two 11 km main linacs utilizing the conventional klystrons and superconducting 1.3 GHz RF cavities with a gradient of 31.5 MV/m and a RF pulse length of 1.6 ms while the CLIC allows the accelerating field of 100 MV/m during a pulse of 156 ns by using a novel accelerating scheme of Two-Beam Acceleration (TBA). This technique uses the deceleration of a high intensity beam to produce the RF power for the main linac. In the framework of the $e^+ - e^-$ sources, the CLIC uses two separate injector complexes to produce the electrons and the positrons respectively while the ILC employs the same electron drive beam passing through a helical undulator to produce afterwards the polarized positron beam. This is a very important difference, since as it will be possible to highlight in the following, the positron source has a strong impact on all the main parameters of the future LC. There is another important project LHeC (e^+/e^- - proton collider) in which a role of the positron source is strongly highlighted [15].

The main design parameters of the CLIC and the ILC are shown in Table 1.1 and 1.2 respectively.

Parameter	Symbol	Value	Unit
Center of mass energy	E_{CMS}	3000	GeV
Main linac RF frequency	f_{RF}	12	GHz
Luminosity	L	5.9×10^{34}	$\text{cm}^{-2}\text{s}^{-1}$
Bunch charge	N_{e^-/e^+}	3.72×10^9	e
Number of bunches per train	N_b	312	bunches
Bunch separation	Δt_b	0.5	ns
Bunch length	σ_τ	44	μm
Bunch train length	τ_{train}	156	ns
Hor./vert. normalized emittance	$\gamma\epsilon_x/\gamma\epsilon_y$	660/20	nm rad
Hor./vert. IP beam size	σ_x/σ_y	40/1	nm
Average current in pulse	I_{train}	1	A
Accelerating gradient	G	100	MV/m
Repetition rate	f_{rep}	50	Hz
Total site length	L_{tot}	48.4	km
Total power consumption	P_{wall}	582	MW

Table 1.1: Main CLIC parameter set [12]

1.3 Future linear collider projects: ILC and CLIC

Parameter	Symbol	Value	Unit
Center of mass energy	E_{CMS}	500	GeV
Main linac RF frequency	f_{RF}	1.3	GHz
Luminosity	L	1.8×10^{34}	$\text{cm}^{-2}\text{s}^{-1}$
Bunch charge	N_{e^-/e^+}	2×10^{10}	e^-/e^+
Number of bunches per train	N_b	1312	bunches
Bunch separation	Δt_b	554	ns
Bunch length	σ_τ	300	μm
Bunch train length	τ_{train}	~ 1	ms
Accelerating gradient	G	31.5	MV/m
Repetition rate	f_{rep}	5	Hz
Hor./vert. normalized emittance	$\gamma\epsilon_x/\gamma\epsilon_y$	10/0.035	$\mu\text{m rad}$
Hor./vert. IP beam size	σ_x/σ_y	474/5.9	nm
Total site length	L_{tot}	30.5	km
Total power consumption	P_{tot}	230	MW

Table 1.2: Main ILC parameter set [10, 11]

1. INTRODUCTION

2

Positrons and polarized positrons

2.1 Discovery of positron

The existence of the positron was introduced by the electron theory of the English theoretical physicist Paul Dirac in his papers of the 1928 [16] and 1929 [17] year. According to Dirac's theory, an electron and a positron may be created in pairs, provided there is enough energy available. For the energy and momentum conservation, it should be at least equal to the total rest mass energy of the two particles $2m_e c^2$ (1022 keV), where m_e is the electron rest mass and c is the speed of light.

A Soviet physicist, Dmitri Skobeltsyn, first observed the positron in 1928 [18, 19]. He was the first who used a Wilson cloud chamber immersed in a magnetic field. Using it, he studied the Compton effect and cosmic radiation. While conducting this experiment he detected particles that behaved like the electrons but bended in the opposite direction in an applied magnetic field. An American physicist, Carl David Anderson finally discovered the positron in 1932 [20] by studying the cosmic radiation passing through a cloud chamber and a lead plate. He noticed the particle tracks in his cloud chamber photographs created by a particle with the same mass as the electron, but with the opposite electrical charge. Later in 1933, a direct proof that the gamma rays from the natural radioactive nuclide ThC'' (^{208}Tl) can produce the positrons was first given by Carl Anderson and his graduate student Seth Neddermeyer, and independently by Irène Curie and Frédéric Joliot, and by Lise Meitner and Kurt Philipp [19]. The performed experiments demonstrated the positron production from a non-cosmic source and showed also that positrons are produced in pairs together with

2. POSITRONS AND POLARIZED POSITRONS

electrons as predicted by Paul Dirac. For this discovery Carl Anderson was awarded a Nobel Prize for Physics in 1936 [19].

In addition to the methods of creating positrons already mentioned, i.e. by absorption of cosmic rays or sufficiently high energy gamma rays emitted by radioactive sources, positrons can be also produced during the disintegration of certain radioactive substances. Positron emission resulting from β^+ decay, was first observed in radioactive decay by Irène Curie and Frédéric Joliot in 1934. The experiment consisted in bombarding Aluminum ^{27}Al with alpha particles. Eventually a radioactive isotope of phosphorous ^{30}P has been produced, which underwent the positron emission by transmutation into Silicon ^{30}Si [21, 22].

Nowadays, the phenomenon of positron emission is of great use in nuclear medicine. It is employed for an imaging method known as Positron Emission Tomography (PET).

Since a long time, in the HEP domain positrons are often used in particle accelerator experiments involving colliding beams. For such an application, the pair creation process $\gamma \rightarrow e^- + e^+$, where the gamma rays are produced by bremsstrahlung in the field of a nucleus¹ in a target, is used to produce the beam of positrons in practical amounts.

At present polarized electron and positron beams are considered to be used at modern accelerator facilities such as the future LC. The polarization phenomenon as well as the general schemes of polarized electron and positron production is discussed in the following sections.

2.2 Polarization formalism. Photon and electron polarization.

Polarization can be seen as a property of an electromagnetic wave or an elementary particle (e.g. electrons or positrons, etc.) resulting respectively from a preferred orientation of the electric field vector or the spin, i.e. the intrinsic angular momentum.

Let's first describe the classical representation of the polarization in the case of an electromagnetic radiation. It is directly connected with the experimentally observable

¹In fact, the electron-electron and the electron-nucleus bremsstrahlung are possible. But since, the contribution of the electron-electron process to the total emission from the electron is small, the electron-electron bremsstrahlung is normally ignored.

2.2 Polarization formalism. Photon and electron polarization.

quantities such as intensities.

Polarization of the electromagnetic radiation is usually described by the oscillation of the electric field vector. For an electromagnetic plane wave of frequency ω and wave vector \vec{k} this can be expressed by two physically independent components of orthogonal polarization [23]:

$$\vec{E}(\vec{r}, t) = \mathcal{E}_1 e^{i\vec{k}\vec{r}} e^{-i(\omega t + \delta_1)} \vec{\epsilon}_1 + \mathcal{E}_2 e^{i\vec{k}\vec{r}} e^{-i(\omega t + \delta_2)} \vec{\epsilon}_2 \quad (2.1)$$

or in simplified version:

$$\vec{E}(\vec{r}, t) = a_1 \vec{\epsilon}_1 + a_2 \vec{\epsilon}_2 \quad (2.2)$$

where \mathcal{E}_i are the real amplitudes and $\vec{\epsilon}_i$ are the perpendicular unit vectors characterizing the polarization state and chosen in the plane orthogonal to the direction of propagation defined by the vector \vec{k} . In Eq. 2.2, a_i are, in general, complex coefficients describing the amplitude and the phase of the two oscillations forming a 2×2 density matrix.

One can consider the following cases to define polarization of the electromagnetic radiation :

- If the phase difference $\phi = \delta_1 - \delta_2 = 0$, the electromagnetic wave is linearly polarized.
- If $\mathcal{E}_1 = \mathcal{E}_2$ and the phase difference $\phi = \pm\pi/2$, the electromagnetic wave has left or right circular polarization.
- If $\mathcal{E}_1 \neq \mathcal{E}_2 \neq 0$ and $\phi \neq 0$, the electromagnetic wave has elliptical polarization.

Usually, the observable quantities are the squares of the field components (e.g. intensity $I \sim |\vec{E}(\vec{r}, t)|^2$). In this context, a convenient description of the polarization which directly relates it to the measurable properties is given by the Stokes parameters, introduced by Sir George Stokes in 1852 [24, 25]. Thus, experimentally, polarization states of the electromagnetic radiation can be determined by doing four intensity measurements. Hence, the Stokes parameters (P_1, P_2, P_3) can be obtained from the following measurements:

1. The intensity of the beam, I_0 ;
2. The degree of plane polarization with respect to two orthogonal axes defined by $\{\vec{\epsilon}_1, \vec{\epsilon}_2\}$, $P_1 = (I_1 - I_2)/I_0$;

2. POSITRONS AND POLARIZED POSITRONS

3. The degree of plane polarization with respect to a set of axis oriented at 45° to the right of the previous one, $P_2 = (I_{45^\circ} - I_{135^\circ})/I_0$;
4. The degree of circular polarization expressed by the difference of the Left and Right intensity components of the circular polarization, $P_3 = (I_L - I_R)/I_0$;

Each Stokes parameter P_i gives the normalized difference of the intensity measurements of the pure states defined by the $\{\vec{\epsilon}_1, \vec{\epsilon}_2\}$ orthogonal basis. The other normalizations can be employed as well in this context. Practically, the second and third measurement can be made with a polarizer like Nicol prism while the fourth requires the additional use of a quarter wave plate. The Stokes parameters satisfy the relation $P_1^2 + P_2^2 + P_3^2 \leq 1$ and often can be written in the form of the Stokes four-vector (I_0, \vec{P}) .

The polarization states of the electron (positron) are specified otherwise by the direction of the spin vector. Unlike the photon, polarized properties of the electron are usually defined in its rest reference frame. One can speak of transverse or longitudinal polarization of the electron if the direction of the spin is respectively perpendicular or parallel/antiparallel to the momentum.

In quantum mechanics, in a case of the nonrelativistic Pauli spin theory, the electron state is described by a two-component wave function i.e. by a spinor ϕ . In the case of pure states ϕ can be represented as the superposition of the eigenfunctions ϕ_i for the spin quantum number $+1/2$ and $-1/2$:

$$\phi = c_1\phi_1 + c_2\phi_2, \quad (2.3)$$

where c_i are, in general, complex coefficients forming a 2×2 density matrix and the wave functions describing pure states may be chosen in the form:

$$\phi_1 = \begin{pmatrix} 1 \\ 0 \end{pmatrix}, \quad \phi_2 = \begin{pmatrix} 0 \\ 1 \end{pmatrix}. \quad (2.4)$$

On the other side, in the relativistic Dirac electron theory, the wave function has four components (bispinor), instead of the two-component wave function of the Pauli theory. They correspond to two independent solutions for the electron (so-called positive energy states) and two for the positron (negative energy states). However, in the rest frame of the electron, a polarization state of the electron can still be specified by Eq. 2.3 if one

2.2 Polarization formalism. Photon and electron polarization.

considers only positive (negative) energy states. A brief description of the polarization effects using 4×4 representation can be found e.g. in [26].

The wave function given by Eq. 2.3 characterizes a totally polarized pure state. But if we have a beam of electrons or photons which is unpolarized or partially polarized this should be considered as a mixed quantum state that is a statistical ensemble of several pure states. Therefore, the states of partial polarization of the photon and the electron beam are given by a density matrix ρ .

The density matrix is defined as the outer product of the wave function and its conjugate $\rho \equiv |\phi\rangle\langle\phi|$ and considered as an alternative way to represent the state of the quantum system. In the case of two fundamental states, the density matrix is 2×2 Hermitian matrix normalized in such a way that $\text{Tr}\rho = \rho_{11} + \rho_{22} = 1$.

For electrons (positrons) the average spin orientation is specified by the direction and magnitude of the vector $\vec{\zeta}$, called the *polarization vector* [27]. Knowledge of $\vec{\zeta}$ is sufficient to identify the density matrix. It can be represented by a linear combination of Pauli matrices $\vec{\sigma}$ and the unit matrix I [28]:

$$\rho = \begin{pmatrix} c_1^*c_1 & c_2^*c_1 \\ c_1^*c_2 & c_2^*c_2 \end{pmatrix} = \frac{1}{2}(I + \vec{\zeta}\vec{\sigma}), \quad \vec{\zeta} = \text{Tr}(\rho\vec{\sigma}) \quad (2.5)$$

The polarization vector is defined as the expectation values of the Pauli matrices $\vec{\sigma} = (\sigma_3, \sigma_1, \sigma_2)$ ¹. Total intensity in this case is given as the expectation value of the unit matrix in the rest frame of the electron [30]:

$$\begin{aligned} I_0 &= \langle\phi|1|\phi\rangle = \begin{pmatrix} c_1^* & c_2^* \end{pmatrix} \begin{pmatrix} 1 & 0 \\ 0 & 1 \end{pmatrix} \begin{pmatrix} c_1 \\ c_2 \end{pmatrix} = c_1^*c_1 + c_2^*c_2 \\ \zeta_1 &= \langle\phi|\sigma_z|\phi\rangle = \begin{pmatrix} c_1^* & c_2^* \end{pmatrix} \begin{pmatrix} 1 & 0 \\ 0 & -1 \end{pmatrix} \begin{pmatrix} c_1 \\ c_2 \end{pmatrix} = c_1^*c_1 - c_2^*c_2 \\ \zeta_2 &= \langle\phi|\sigma_x|\phi\rangle = \begin{pmatrix} c_1^* & c_2^* \end{pmatrix} \begin{pmatrix} 0 & 1 \\ 1 & 0 \end{pmatrix} \begin{pmatrix} c_1 \\ c_2 \end{pmatrix} = c_1^*c_2 + c_2^*c_1 \\ \zeta_3 &= \langle\phi|\sigma_y|\phi\rangle = \begin{pmatrix} c_1^* & c_2^* \end{pmatrix} \begin{pmatrix} 0 & -i \\ i & 0 \end{pmatrix} \begin{pmatrix} c_1 \\ c_2 \end{pmatrix} = i(c_2^*c_1 - c_1^*c_2). \end{aligned} \quad (2.6)$$

In the rest reference frame of the electron, for pure states polarization vector $\vec{\zeta}$ is a unit vector in the direction of the electron spin where $|\vec{\zeta}| = 1$ while $|\vec{\zeta}| < 1$ for mixtures.

¹The order of the Pauli matrices depends on the convention used [29]. Sometimes the basis with natural ordering $\vec{\sigma} = (\sigma_1, \sigma_2, \sigma_3)$ can be employed.

2. POSITRONS AND POLARIZED POSITRONS

The polarization vector of the electron beam is then obtained as the average of all individual polarization vectors ζ_i :

$$\vec{\zeta} = \begin{pmatrix} \zeta_1 \\ \zeta_2 \\ \zeta_3 \end{pmatrix} = \frac{1}{N} \sum_{i=1}^N \vec{\zeta}_i \quad (2.7)$$

Length of the polarization vector $\zeta = |\vec{\zeta}|$ is called the *degree of polarization* in a given direction. The state of random spin orientation has $\zeta = 0$. In such a way, the unpolarized electron beam can be considered as the ensemble of electrons with spin pointing isotropically in all directions.

For the longitudinally polarized electron (positron) beam which is indeed a major concern for the future LC, the degree of the effective polarization is given by the normalized difference of the number of electrons having their spins parallel and antiparallel to the momentum, that is

$$P_e = \frac{\zeta_3}{I_0} = \frac{i(c_2^*c_1 - c_1^*c_2)}{c_1^*c_1 + c_2^*c_2} = \frac{N_+ - N_-}{N_+ + N_-} \quad (2.8)$$

where N_+ is the number of particles with the spin in the momentum direction with its value of $+1/2$ and N_- is the number of particles having the spin antiparallel to the momentum direction with its value of $-1/2$ corresponding to the helicity ± 1 for photons.

As for the light, where the polarization can be studied with the Nicol prism, the polarization state of the electron (positron) beam can be determined in a scattering experiments. These experiments generally involve the measurement of a counting rate asymmetry Δ for two different spin configurations. Thus, the longitudinal beam polarization is defined as

$$P_e = \frac{1}{A} \frac{R_+ - R_-}{R_+ + R_-} = \frac{1}{A} \Delta, \quad (2.9)$$

where A is the cross section asymmetry or so-called analyzing power, $A = \frac{d\sigma^- - d\sigma^+}{d\sigma^- + d\sigma^+}$, usually estimated from the Monte-Carlo simulations, R_+ and R_- are the measured counting rates, where sign $+$ and sign $-$ denote opposite and like sign spin configuration of two beams involved in the experiment.

A similar approach is used for the photon polarization. In this case, using Eq. 2.2 the density matrix for pure state in $\{\vec{\epsilon}_1, \vec{\epsilon}_2\}$ is

$$\rho = \begin{pmatrix} a_1^*a_1 & a_2^*a_1 \\ a_1^*a_2 & a_2^*a_2 \end{pmatrix} = \frac{1}{2}(I + \vec{\xi}\vec{\sigma}), \quad \vec{\xi} = Tr(\rho\vec{\sigma}), \quad (2.10)$$

2.3 Polarized electrons and positrons for ILC/CLIC

where $\vec{\xi} = (\xi_1, \xi_2, \xi_3)$ is the polarization vector for the photons, the components of which are called the *Stokes parameters* in analogy to the Stokes parameters (P_1, P_2, P_3) defined in the classical optics. From Eq. 2.10 it follows that

$$\begin{aligned}
 I_0 &= a_1^* a_1 + a_2^* a_2 \\
 \xi_1 &= a_1^* a_1 - a_2^* a_2 \\
 \xi_2 &= a_1^* a_2 + a_2^* a_1 \\
 \xi_3 &= i(a_2^* a_1 - a_1^* a_2)
 \end{aligned}
 \tag{2.11}$$

In this case, the degree of linear polarization is defined as $P_l = \sqrt{\xi_1^2 + \xi_2^2}$ while the degree of the circular polarization is $P_c = \xi_3$.

Table 2.1 gives the meanings of both the Stokes parameters for the photons and the components of the polarization vector for the electrons. So, the polarized states of the photon and electron (positron) are fully defined by the vectors $\vec{\xi}$ and $\vec{\zeta}$.

As one can see, there is a direct analogy between the polarization description of electromagnetic radiation (photons) and electrons (positrons) except for one issue. In the case of electrons, the polarization vector (spin direction) is fixed by the choice of coordinate system without regarding the motion of the particle. For photons only the spin projection (helicity) in the \vec{k} direction is invariant. Therefore for the photon spin to be observable property, the coordinate system should be chosen in a way that $\{\vec{\epsilon}_1, \vec{\epsilon}_2\}$ are perpendicular to the direction of propagation \vec{k} [31]. It means that a_1 and a_2 in Eq. 2.2 defined with respect to $\{\vec{\epsilon}_1, \vec{\epsilon}_2\}$ should be fixed with respect to \vec{k} . Thus, one can state that spin of the photon is always oriented in the direction of propagation and that the spin orthogonal to the direction of propagation does not exist [32]. Hence, photon as a massless particle which travels at the speed of light always has a helicity ± 1 . While the helicity of the massive particle (e.g. electron, etc.) depends on the chosen frame of reference.

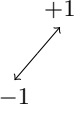
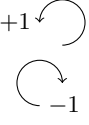
2.3 Polarized electrons and positrons for ILC/CLIC

2.3.1 Polarized electrons

High intensity low emittance positron beams are required in HEP to be used both for the circular and linear colliders (see Chapter 1). Moreover, a full exploitation of the

2. POSITRONS AND POLARIZED POSITRONS

Table 2.1: Comparison of Stokes parameters and electron polarization vector.

Stokes parameters		Photon		Electron
I_0		Intensity		Intensity
P_1 or ξ_1		Plane polarization along $\vec{\epsilon}_1$ (+1) and $\vec{\epsilon}_2$ (-1)	$-1 \longleftrightarrow +1$	Transverse polarization ζ_1 orthogonal to the momentum direction
P_2 or ξ_2		Plane polarization at 45° to the right of $\vec{\epsilon}_1$ and $\vec{\epsilon}_2$		Transverse polarization ζ_2 orthogonal to the momentum direction
P_3 or ξ_3		Left (+1) and Right (-1) circular polarization		Longitudinal polarization ζ_3 parallel (+1) or antiparallel (-1) to the momentum direction

physics potential of a future linear collider (ILC and CLIC) requires the development of a polarized positron beam in addition to the polarized electron beam [6]. The necessary intensive sources of polarized positrons have not existed yet since obtaining high energy polarized particles in general is a challenge.

As for the polarized electron source for the future LC, extensive studies on high current and high polarization electron sources for the ILC and the CLIC are ongoing mainly at SLAC and JLAB in the United States. Photoemission from the negative electron affinity (NEA) GaAs photocathode illuminated by the circularly polarized laser beam as a method to generate the polarized electrons was proposed in 1970s [33, 34]. Due to the symmetry of GaAs crystal the maximum electron polarization achievable is limited to 50% [35]. However, the depolarizing effects, like lattice imperfections and electron scattering during the photoemission limit the polarization to around 37% with a quantum efficiency of about 10%. It was observed at the first accelerator polarized electron source (PEGGY) in SLAC [36]. The enhancement of the spin polarization from GaAs photocathode can be accomplished by lowering the crystalline symmetry of GaAs lattice: create deformation in the lattice [37] (strained lattice GaAs cathode) or create structure with a lower symmetry [38] (superlattice GaAs cathode). The polarization of these new electron sources has increased to the level of 70% while a theoretical

2.3 Polarized electrons and positrons for ILC/CLIC

polarization can reach 100%. The polarization measured experimentally is lower than the theoretically predicted one because the initial polarization of the excited electrons in the conduction band of GaAs is deteriorated due to several depolarization effects during the photoemission process. Later, strained superlattice structures, consisting of thin GaAs layers alternating with layers having lattice mismatch (e.g. GaAsP) have been found to be more preferred to achieve a higher polarization. In such a way, the polarization increased from about 25% in 1992 to over 80% in 1994 at SLC polarized electron source by using thin, strained superlattice photocathodes [39].

The high polarization cathodes nowadays consist of GaAs layer grown on a sublayer of GaAsP, whose different lattice constant provides the mechanical strain. At the same time, a superlattice structure that is the alternating layers of GaAs and GaAsP is used for these cathodes to increase the polarization and the photoelectron yield. For such photocathodes, Maruyama et al. at SLAC reported an electron polarization as high as 86% with a quantum efficiency of over 1% [40]. Recently, strained InAlGaAs/AlGaAs structures designed and manufactured at St. Petersburg in Russia have shown excellent performance with 90% polarization and about 1% of quantum efficiency [41]. M. Kuwahara et al. at Nagoya reported in [42] a maximum achieved polarization of 92% with a quantum efficiency of 0.5% for the strained-layer superlattice GaAs/GaAsP structures. In such a way, recent developments of the semiconductor photocathodes show a feasibility of highly polarized electron source at the future LC. The degree of polarisation of the electron beam is expected to be at least 80%.

2.3.2 Polarized positrons

The positrons are the antiparticles and to fit the future LC requirements have to be generated in a more sophisticated manner. The classical or so-called conventional method to produce positrons for the accelerator applications is to send a high intensity electron beam, usually originated from a linear accelerator (linac), to a thick (typically many radiation lengths) target-converter of a high Z material to increase the electromagnetic shower generation [43]. The electrons traversing the target lose energy both by atom excitation, ionization and by bremsstrahlung. The photons produced during the development of the electromagnetic shower inside the target interact with the nucleus and are converted into the $e^- - e^+$ pairs. A focusing system after the target collects the emitted positrons and guides them to the acceleration section. More details about

2. POSITRONS AND POLARIZED POSITRONS

the positron production process and the capture systems see in sections 4.2 and 4.3. This approach was and continues to be a typical positron production system for the accelerator applications.

A common feature of the future LC projects is the requirement to generate a large number of electrons and positrons confined in short pulses and, as far as possible, with an important degree of polarization for both. Thus, the intensity required for the positron source is a few orders of magnitude higher than that delivered by the existing ones. This would be difficult to realize by the conventional scheme using electrons which are converted into the positrons because of the high heat load inside the target as well as a thermal shock wave caused by the inhomogeneity in energy deposition. On the other hand, this method is also not attractive due to the lack of positron polarization unless a polarized electron beam is used to generate the positrons.¹ The polarized bremsstrahlung [44] as a method to produce polarized positrons is considered to be not very efficient in a framework of the future LC. It is mainly due to the low positron capture efficiency at high energy part of the positron spectrum where the population characterized by a high degree of polarization is located.

As a better solution, a two-stage process was proposed for the positron production at the LC. The first stage is a generation of gamma rays. In the second stage the electron and gamma ray beams are separated and the latter is sent to the target where the gamma rays are converted into $e^- - e^+$ pairs. This relaxes the large energy losses given by the low energy population of the drive beam leading to the heating of the target. The major difference now between the different methods to produce positrons is how these gamma rays are generated.

In 1978-1979 V. E. Balakin and A. A. Mikhailichenko proposed to use a helical undulator for the Russian Linear Collider project (VLEPP) as the source of circular polarized photons [45]. Now, this solution is the baseline for the ILC positron source. A main feature of this method is that the positrons generated in the target-converter are longitudinally polarized as requested by the physics to be done at the future LC. Another idea came up in Orsay and was proposed by R. Chehab et al. [46]. They

¹In this case, the polarization transfer from the electron to the bremsstrahlung photon takes place that results into the polarized positron production. This method of positron production usually is called polarized bremsstrahlung [44].

2.3 Polarized electrons and positrons for ILC/CLIC

suggested to use channeling effect¹ to generate the photons to be subsequently converted into the positrons. Later, this idea as an alternative was proposed to be employed at the future LC [48] and now it became a baseline for the unpolarized positron source for the CLIC project [12].

During the 1990s, the Compton scattering of the laser photons off the relativistic electron beam had been suggested in [49, 50] and proposed by T. Omori et al. as a method to generate circular polarized high energy photons [51]. Presently, a Compton based polarized positron source is considered to be used in the design of the CLIC polarized positron source [12].

The polarization degree of the positron beam in the case of the ILC is expected to be 30% with the possibility to be improved to 60% after the machine upgrade. As for the CLIC, the baseline design consists of unpolarized positron source while the polarization is considered as an upgrade option.

To summarize, the following classes of positron sources in the context of future LC are considered:

1. **Conventional positron source:** initial photons are produced within the target by bremsstrahlung. *Not feasible for the future LC requirements. However, with modified pulse time structure of the electron beam impinging on the target and sophisticated target cooling system it seems possible to sustain the ILC unpolarized positron source requirements [52].*
2. **Positron source using channeling:** initial photons are produced by channeling effect within the target or two separate targets are used. In this case, so-called hybrid positron source employs a crystal target as a radiator of high energy photons followed by the amorphous target-converter. *CLIC baseline and one of the option for the unpolarized positron source at the ILC.*
3. **Undulator based positron source:** initial photons are produced by helical undulator. *ILC baseline for the polarized positron source.*
4. **Compton based positron source:** initial photons are produced by Compton scattering. *Preferred scheme of the polarized positron source for the CLIC.*

¹ High energy electrons impinging at sufficiently small angles to a major crystallographic axes of an oriented crystal will be trapped in orbits spiraling around that atomic row, meanwhile radiate a large number of photons [47].

2.4 Radiative polarization (selfpolarization)

Both electron and positron beams stored in a storage ring can become polarized due to emission of synchrotron radiation.

By means of spin flips caused by a small fraction of synchrotron radiation in the magnetic field of bending dipoles the spin of the stored particles align parallel or antiparallel to the transverse magnetic field. Theoretically it was shown that the beam polarization emerges due to the probability of the transition in a state where the spin is aligned antiparallel to the magnetic field which is higher than the probability of the inverse transition. In such a way, the transverse polarization is gradually built up. This so-called radiative polarization was firstly pointed out by Sokolov and Ternov [53] and described in [54].

In an ideal storage ring the build up of the radiative polarization proceeds according to:

$$P(t) = P_{max} \left(1 - e^{-t/\tau} \right), \quad (2.12)$$

where the maximum possible equilibrium polarization P_{max} in the absence of depolarizing effects is $P_0 = \frac{8}{5\sqrt{3}} = 92.4\%$ and the characteristic time constant for the polarization build up is

$$\tau_0 = \left[\frac{5\sqrt{3}}{8} \frac{e^2 \hbar \gamma^5}{m^2 c^2 \rho^3} \right]^{-1} \quad (2.13)$$

depending on the energy of the stored particles through γ and the ring bending radius ρ . At HERA the time constant is 40 minutes at 27 GeV, at LEP at 46 GeV the time constant is about 300 minutes and at TRISTAN at 29 GeV it is about 2 minutes [55].

In the real storage rings the selfpolarization mechanism due to Sokolov-Ternov effect is strongly affected by several depolarization processes leading to the reduction of the maximal achievable polarization and build-up time. For example at HERA at 27 GeV, with a depolarization time of $\tau_{dep} = 10$ min (τ_{dep} is a time constant describing the strength of the depolarization) the build-up time $\tau = 8$ min and $P_{max} = 0.18$ [56].

In the case of the future LC the storage time of the positron beam in a Damping Ring (DR) is too small (about 20 or 200 ms) to consider the selfpolarization as a method to polarized the positron beam.

2.5 Undulator based polarized positron source

The usage of undulator radiation allowing to obtain both polarized positrons and electrons has been proposed [45, 57] and studied in [58]. The radiation from helical undulator is circularly polarized. This makes it especially attractive in the context of polarized positron sources. Since there is a well-defined correlation between the photon energy, its emission angle and polarization, by performing an energy selection of the undulator photons, one can choose a desirable degree of photon polarization.

Helical undulator consists in a pair of conductors which are wound in a form of double helix. These two helices are shifted in the longitudinal direction by half of the period. Direction of the helical winding (left/right handed) defines the helicity of emitted photons in the undulator. Each helix is carrying an equal current but in opposite directions. Due to longitudinal shift of the helices, the solenoid axial magnetic field is cancelled out. Thus, the helical undulator is characterized by the sinusoidal horizontal and vertical magnetic field components with the same peak field and with the identical periods: $\vec{B}(z) = B_0[\cos(\frac{2\pi z}{\lambda_u}), \sin(\frac{2\pi z}{\lambda_u}), 0]$, where λ_u is the period of the undulator. Electrons traversing the undulator undergo helical oscillations and emit photons.

The main parameters defining the properties of the undulator radiation are so-called the *undulator strength parameter*:

$$K = 0.934B_0[T]\lambda_u[cm] \tag{2.14}$$

and the *energy cutoff of the first harmonic radiation*:

$$E_{c1} = \frac{2\gamma^2 hc/\lambda_u}{1 + K^2 + 2\gamma\lambda_C/\lambda_u}, \tag{2.15}$$

where B_0 is the magnetic field on the axis of the undulator, λ_u is the period of the undulator, over which the magnetic field rotates through 360° , γ is the Lorentz factor of the electron beam energy and $\lambda_C = h/mc = 2.4 \times 10^{-12}$ m is the Compton wavelength of the electron. The radiation spectrum peaks at the energy of the first harmonic. For the higher K value, the number of the harmonics which contribute to the radiation is bigger i.e. the number of high energy photons is getting larger and the photon spectrum becomes broader.

2. POSITRONS AND POLARIZED POSITRONS

There is a fixed kinematic relation between energy E_γ and angle of emission θ of the photons due to n -th order multipole radiation (in this case the small angles θ with respect to the electron beam are assumed):

$$E_\gamma(n, \theta) = \frac{nE_{1c}}{1 + (\gamma\theta)^2/(1 + K^2)} \quad (2.16)$$

The radiation of the helical undulator is emitted over a narrow cone of the angle $\sim 1/\gamma$ around the electron motion direction. Different emission cones correspond to the specific harmonics. For the higher harmonic number n , the cone angle is larger. Eq. 2.16 also shows that by varying the geometrical acceptance of the photon beam, one can select the energy distribution required. The details and kinematics of undulator radiation are described in [59, 60].

The photon number spectrum of the helical undulator radiation is given by [61, 62]:

$$\begin{aligned} \frac{dN_\gamma}{dE_\gamma} \left[\frac{1}{\text{m MeV}} \right] &= \frac{10^6 e^3}{4\pi\epsilon_0 c^2 \hbar} \frac{K^2}{\gamma^2} \sum_{n=1}^{\infty} \left(J_n'^2(x_n) + \left(\frac{\alpha_n}{K} - \frac{n}{x_n} \right)^2 J_n^2(x_n) \right) \Theta(\alpha_n^2), \\ \alpha_n^2 &= n \frac{E_{1c}(1 + K^2)}{E_\gamma} - 1 - K^2, \\ x_n &= 2K \frac{E_\gamma}{E_{1c}(1 + K^2)} \alpha_n, \end{aligned} \quad (2.17)$$

where ϵ_0 is the vacuum permittivity, \hbar is the Planck constant, K is the undulator strength parameter, n is the harmonic number, J_n and J_n' are the n -th order Bessel functions and their derivatives, Θ is the Heaviside function, E_{1c} is the energy cutoff of the first harmonic radiation. The photon number spectrum $\frac{dN_\gamma}{dE_\gamma}$ (Eq. 2.17) is shown on Fig. 2.1a. As one can see the emission of photons due to higher harmonics of radiation is strongly suppressed for low values of K . An approach developed in reference [63] is used for polarization calculation.

As far as the first harmonic is concerned, the undulator photons produced on axis ($\theta = 0$) have maximum polarization $\xi_3 = +1$ but it drops for larger angles what corresponds to the low energy part of the spectrum. This behavior is illustrated in Fig. 2.1b. The polarization of higher harmonic radiation approaches unit at the corresponding cutoff energies but the photon emission rate there is very low (see Fig. 2.1).

The average polarization of all undulator photons is nearly zero but since higher energy photons have higher polarization and are produced at small angles, it is possible

2.5 Undulator based polarized positron source

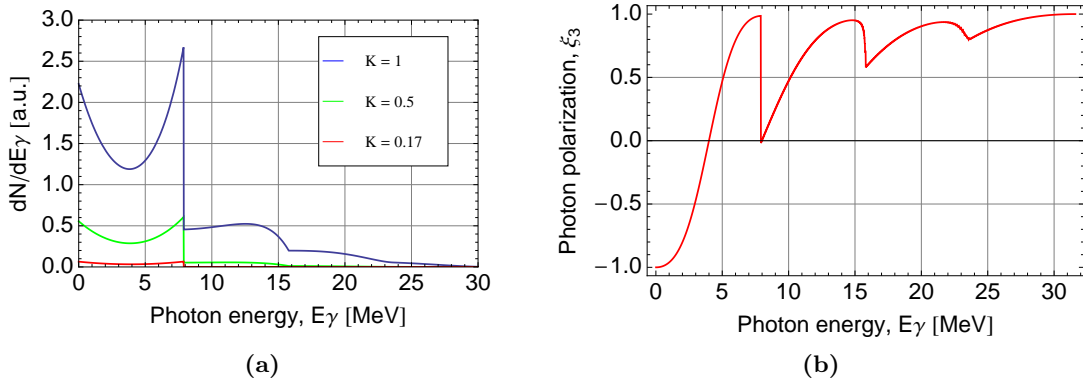


Figure 2.1: Undulator radiation properties. - Photon number spectrum integrated over angle of helical undulator is shown on Fig. 2.1a for electron energy $E_e = 46.6$ GeV and different values of the undulator strength parameter K . The energy cutoff E_{c1} of the first harmonic radiation is 7.9 MeV. Fig. 2.1b shows the circular polarization of the undulator radiation (Stokes parameter ξ_3) as a function of the energy for the undulator period $\lambda_u = 2.54$ mm and $K = 0.17$ (parameters correspond to the E-166 experiment). Note, only the first four harmonics are shown.

to enhance the average polarization by collimating the photon beam. Collimators can be used to cut the low energy part of the first harmonic photon energy spectrum and at the same time they serve to cut the higher orders harmonics since they have zero intensity in forward direction for helical undulator.

In this context, the undulator based positron source driven by the main 150 GeV electron beam is conceived as part of ILC baseline design [10]. The electron beam passes through a ~ 150 meter helical undulator producing the high energy ($E_{c1} \sim 10$ MeV) circularly polarized photons. The undulator photons then are directed onto a rotating target where they are converted to polarized positrons.

A proof of principle experiment E-166 [64] has been performed in the Final Focus Test Beam (FFTB) at SLAC to demonstrate production of polarized positrons for a further implementation in the undulator scheme at the ILC [65]. One meter long pulsed helical undulator of 2.54 mm period and strength 0.71 T on axis corresponding to an undulator strength parameter of $K = 0.17$ has been installed in FFTB at SLAC in 2004. This undulator produced circularly polarized photons with the energy cutoff of the first harmonic of 7.9 MeV when traversed by a 46.6 GeV electron beam. The calculated photon number spectrum and the circular polarization of the undulator radiation for

2. POSITRONS AND POLARIZED POSITRONS

the experimental parameters of E-166 are shown on Fig. 2.1a and 2.1b respectively. The polarized photons have been converted to the polarized positrons in a $0.2 X_0$ Tungsten target. The measurements of the positron polarization have been performed at five positron energies from 4.5 to 7.5 MeV with a peak value above 80%.

Although experiment E-166 has successfully demonstrated a feasibility of undulator based polarized positron source for the ILC, some of its major elements still require extensive R&D studies. Among the most challenging parts of the positron source are the production and the alignment of the ~ 150 meters long superconducting (SC) helical undulator with a ~ 6 mm inner diameter vacuum chamber. The complete undulator would be built from the shorter modules. Recently, a fully working high field, short period 4 meters long prototype SC helical undulator cryomodule suitable for use in the future ILC positron source has been designed, manufactured and successfully tested [66]. The required on-axis peak field of 0.86 T has been achieved with $\lambda_u = 11.5$ mm and beam aperture of 5.85 mm. Another challenging part is the production target which must operate in severe conditions: all the photon beam power is concentrated into a small spot size and is deposited in a 1 ms time scale. Such an energy deposition would induce a mechanical stress in the target material and eventually destroy the target. Therefore, a new sophisticated target concept implying a rotating Titanium wheel that has a diameter of 1 m and rotates at 2000 RPM is envisaged [67].

Other important issues, like photon beam collimators, the design of a positron capture system based either on a pulsed flux concentrator capable to maintain a 1 ms flat top field during the ILC bunch train or SC coils and the radiation environment near the target, are under the study.

2.6 Compton based polarized positron source

The Compton Scattering method to produce polarized positrons is based on the production of polarized gamma rays by Compton Scattering of the circular polarized laser light (usually with laser photon wavelength $\lambda = 1 - 10 \mu\text{m}$) off the electron beam with the energy of about 1-3 GeV. A simplified scheme of the Compton positron source is illustrated in Fig. 2.2.

The main advantages of the Compton scheme are that the positron source is imposed independently with respect to the main linac and the required drive electron

2.6 Compton based polarized positron source

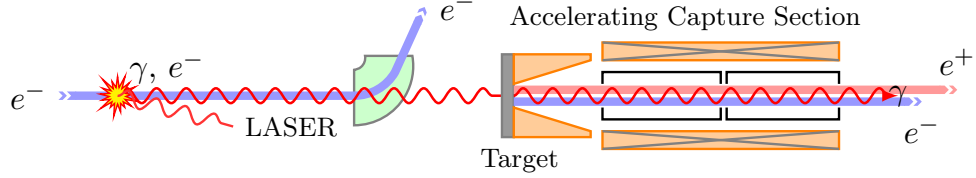


Figure 2.2: A fundamental scheme of the polarized positron production by Compton scattering. - Polarized laser photons are scattered off the electron beam producing the high energy polarized gamma rays. The later is directed to the target converter resulting in production of the polarized positrons which are collected and further accelerated by Accelerating Capture Section (ACS).

beam energy is much lower as compared to the undulator scheme. Moreover, since the angular momentum is conserved, the photon and consequently the produced $e^- - e^+$ pair helicities are conserved in the scattering event and so to reach a high degree of positron polarization in principle is straightforward. Furthermore, one can easily switch the positron polarization just by changing the polarization of the laser light. At the same time this kind of positron source suffers from the relative low value of the scattering cross section ($\sigma_{Compton} \approx \sigma_{Thomson} \sim 6 \times 10^{-29} \text{ m}^2$) resulting in the low number of positrons produced per one electron beam crossing. Eventually, the challenge of the Compton based positron source is that, despite the low value of the cross section, to have enough gamma rays to produce enough positrons per second, that is $\sim (1 - 3) \times 10^{14} e^+ \text{ s}^{-1}$ as required by the future LC. For this, a flux of at least $\sim 10^{16}$ circular polarized gamma rays per second being required. Thus, it is important to find solutions to increase the number of gamma rays produced per one electron bunch crossing and optimize the positron production and capture stages to ensure the positron flux required.

For the first time, a possible design of the polarized positron source based on the Compton scattering for the future LC employing 6.7 GeV electron linac and 85 CO₂ lasers producing the gamma rays with energies $\leq 80 \text{ MeV}$ was proposed by T. Omori et al. [51]. Later, the first proposal of such positron source for the ILC has been presented in 2005 during Snowmass (Colorado, USA) workshop¹. The principle scheme of the proposed system is given in [68]. The electrons are accelerated to 1.3 GeV in a linac and injected into the 277 meters long Compton Ring, that is an electron storage ring

¹Later on, the corresponding scheme was named after this conference.

2. POSITRONS AND POLARIZED POSITRONS

in which optical cavities are installed for multiple laser–electron collisions. The beam consists of the 10 trains, each with 280 bunches ($6.2 \times 10^{10} e^-/\text{bunch}$). The scheme comprises 30 optical cavities which are installed along the electron storage ring. Two different solutions for the complex optical system using YAG and CO₂ lasers have been explored. The angle between the laser and the electron beam in the Compton scattering was set to be 8 degrees. Approximately 2×10^8 polarized positrons were estimated to be produced from polarized photons generated in the 30 Compton IPs. After the target, positrons are collected and accelerated by the linac to 5 GeV. Recently, A. Variola proposed a new solution to provide the electron beam for the Compton IP [69]. This proposal implies using the Energy Recovery Linac (ERL) which is a continuous electron linac working at high repetition frequency.

Nevertheless, despite the increasing the gamma ray flux produced, the positrons accepted per one bunch crossing does not fit the high CLIC and ILC requirements. For this reasons, stacking of the positron bunches was proposed [70]. So the low single positron bunch population could be compensated by the multiple injections in the same Damping Ring (DR) bucket. Thus, the parameterization and performance of the polarized positron sources based on Compton interaction is rather complicated and under study now. It still requires a lot of R&D and simulation works.

To summarize, several concepts for the ILC and CLIC positron source based on Compton scattering have been proposed. Today, they can be classified according to the electron source used for the Compton scattering as following:

- **The linac scheme.** Initiated by the Brookhaven National Laboratory (BNL). Polarized positron source based on the Compton scattering of CO₂ laser beam and 4 GeV electron beam produced by linac is proposed in [71]. This proposal came out after the successful Compton experiment at Brookhaven accelerator facilities using CO₂ laser system delivering a 5 ps pulses of 1 TW and a 60 MeV high brightness photocathode Radio Frequency (RF) electron linac. By measuring the number of scattered photons which in this case belong to the soft X-ray region (~ 6.5 keV), the production of one X-ray photon per every electron was demonstrated [71, 72].
- **The storage ring scheme or so-called Compton Ring.** A conceptual design of a polarised positron source based on the Compton scattering was initially

2.6 Compton based polarized positron source

propose for the ILC. A lot of studies and improvements have been made since then [73]. At present, it has been promoted to be the polarized positron source baseline for the CLIC project [74]. In this case, given the requirements of the CLIC positron source, the feasibility of the Compton Ring seems to be more realistic. However, it should be pointed out that the main constraint of the Compton Ring is given by the electron beam dynamics. During the collision between electrons and laser photons, energy is transferred. This results in an increased energy spread for the electron bunch. In the storage ring this increases the energy spread turn by turn and may have significant effect on the electron beam dynamics, reducing the gamma ray flux despite the synchrotron damping.

The first experimental studies for a Compton positron source was carried out in the Japanese Linear Collider (JLC) framework and reported in [75]. In 2005, an experiment was performed at the KEK Accelerator Test Facility (ATF) in order to proof the Compton based scheme for polarized positron generation and to develop the polarimetry of short pulses of photons and positrons with a time duration of a few tens of picoseconds [76]. In this experiment, a 1.28 GeV electron beam with a typical beam intensity of $1.8 \times 10^{10} e^-/\text{bunch}$, a repetition rate of 3.12 Hz, a bunch length of 31 ps from the ATF and the second harmonic of a Nd:YAG laser of 532 nm with a pulse length of 110 ps, and an average energy of 400 mJ/pulse were used to produce polarized photons with a maximum energy of 56 MeV. After the laser optics optimization a flux of $2 \times 10^4 e^+/\text{bunch}$ was obtained. The polarization of the positrons has been measured by means of the gamma ray polarimetry to be at the level of $73 \pm 15(\text{stat}) \pm 19(\text{syst})\%$.

Due to this set of experiments it was demonstrated for the first time the feasibility of the polarized positron beam production scheme based on the Compton scattering and its possible realization for the future linear collider projects.

- **The energy recovery linac scheme.** As an option, the ERL configuration can be applied instead of the electron storage ring. The ERL consists in a superconducting linac, whose electron bunches are recirculated once to restore the energy to the RF structure what makes the ERL scheme very efficient in regard to the power consumption. At the same time, the beam dump requirements are diminished since due to the energy recovery concept, the electrons are dumped

2. POSITRONS AND POLARIZED POSITRONS

at the energy close to their injection energy. The electron bunch characteristics are preserved for each new collision with the photon pulses.

This scheme is very attractive since the electron bunch after the interaction with the laser pulse is renewed. This allows to have a not degraded bunch for each collision. The ERL feasibility for the Compton polarized positron sources is discussed in [69]. It is shown that to fulfill all the requirements, in the case of the ILC and CLIC, the thousands of bunches should be stacked into the same DR bucket. This is very difficult to achieve but, in the ERL case, it is possible to increase the number of the collision points with negligible impact on beam dynamics in contrast to the Compton Ring scheme. At present the main limitation is given by the weak charge per bunch. The maximum ERL current achieved is now about 10 mA (a few hundreds of pC per bunch) [77]. But, obtaining higher average current seems feasible and together with a repetition frequency adjustment makes it possible to parametrize the ERL based Compton positron source for the ILC and CLIC.

It should be emphasized that a common technological constraint of all the above mentioned schemes is also given by the average laser power of the optical systems. Usually these systems are based on high-gain Fabry-Perot cavities¹ [78] coupled with either a high average power fiber amplifier or a conventional bulk amplifier. The main limitations concern the high reflectivity mirror coatings able to sustain the accumulated high power density, the technology of high power fibers and the laser-cavity locking system. At present, the best results are achieved using the fiber technology and different R&D programs are ongoing to improve the performance of such laser systems [79].

¹Fabry-Perot cavity is a passive optical resonator where the enhancement of the laser pulse energy is achieved by the continuous stacking of laser pulses.

3

Theoretical introduction for innovative schemes

3.1 Compton effect

3.1.1 Thomson and Compton scattering

An electron interacting with an electromagnetic wave can be described by a representation where the electromagnetic radiation accelerates the electron and the accelerated electron in turn emits radiation, according to Larmor's equation. But it can be also seen as a scattering process. In such a way, it is convenient to introduce a scattering cross section which gives the probability to observe a scattered particle in a given quantum state. The differential cross section for the unpolarized incident radiation is given by [23]:

$$\frac{d\sigma}{d\Omega} = \left(\frac{e^2}{m_e c^2} \right)^2 \frac{1}{2} (1 + \cos^2 \theta). \quad (3.1)$$

A term $r_e = \frac{e^2}{m_e c^2} \approx 2.82 \times 10^{-15}$ m is called classical electron radius and θ is the photon scattering angle with respect to its initial momentum as shown on Fig. 3.1. This formula is valid only at low incident photon energies ($w_1 \ll m_e c^2$) when the recoil of the charged particle can be neglected (see Fig. 3.1). When the incident photon energy becomes comparable to or larger than the electron energy, quantum-mechanical effects should be taken into account.

3. THEORETICAL INTRODUCTION FOR INNOVATIVE SCHEMES

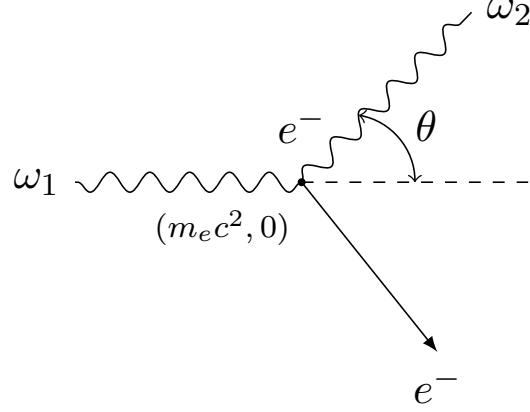


Figure 3.1: Geometry for the Thomson and Compton scattering in the rest frame of the electron - The energy of the initial and the scattered photon is ω_1 and ω_2 respectively. The rest mass energy of the electron is $m_e c^2$. In the case of the Compton scattering, the recoil of the scattered electron takes place.

The angular distribution is shown on Fig. 3.2. As one can see from Eq. 3.1 the differential scattering cross section is independent of the energy of the incident photon and is also symmetric with respect to forward and backward scattering. The energy of the scattered photon is the same of the incident's one.

The total scattering cross section, therefore is obtained by integrating over the entire solid angle:

$$\sigma_T \equiv \frac{8\pi}{3} \left(\frac{e^2}{m_e c^2} \right)^2 = \frac{8\pi}{3} r_e^2 \approx 6.65 \times 10^{-29} m^2. \quad (3.2)$$

This type of scattering is called *Thomson Scattering* and the cross sections given by Eq. 3.2 gives the typical scale of the electromagnetic interactions. The Thomson scattering describes photon scattering by free electrons in classical electromagnetism. When the recoil of the charged particle takes place, the Thomson formula is not valid anymore.

Firstly, this phenomenon was experimentally observed in 1923 year by Arthur Holly Compton. He found that the energy of the scattered photon is less than the incident energy because the charged particle recoils during collision [80]. The difference between the photon wavelength before and after interaction is called the *Compton shift* and the process, accordingly *Compton scattering*. Later, the generalization of Eq. 3.1 for relativistic case was derived by Oskar Klein and Yoshio Nishina [81].

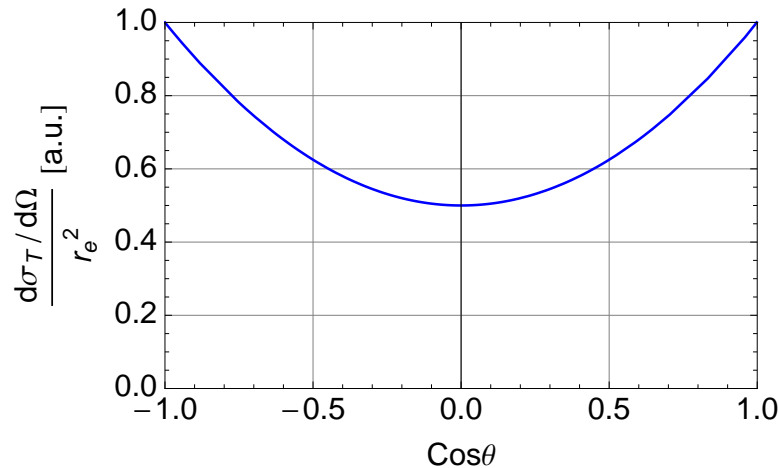


Figure 3.2: Thomson differential cross section - Thomson differential cross section.

Usually, Compton scattering refers to the interaction involving the electrons of an atom while the scattering, in which the low energy photons receive energy boost during a collision with the high energy electrons is called *Inverse Compton Scattering* (ICS)¹.

Thus, the Thomson Scattering is an approximation of Compton Scattering in the low energy limit when the quantum effects are not significant anymore.

3.1.2 Kinematics of the Compton scattering

The emission spectrum can be calculated analytically for single scattering only. For multiple scattering, where the produced gamma ray is scattered many times by the electrons, numerical simulations are usually necessary.

The notation used throughout this write-up is the following: the initial photon and electron energy is expressed as ω_1 and $E_e = \gamma m_e c^2$, respectively; the energy of the scattered photon is ω_2 and that of electron is E_{2e} (see Fig. 3.6).

For some of the further calculations we will use the so-called "God-given" units, where $\hbar = c = 1$.

3.1.2.1 Feynman diagrams. Scattering amplitude.

Compton scattering as a Quantum ElectroDynamics (QED) process involves two diagrams in the lowest order in α_{QED} , see Fig. 3.3. The reaction could be given in the

¹For simplicity reason, in the rest of the manuscript "Compton scattering" is used to describe indifferently Compton scattering or Inverse Compton Scattering.

3. THEORETICAL INTRODUCTION FOR INNOVATIVE SCHEMES

following form:

$$e^- \gamma \rightarrow e^- \gamma \quad (3.3)$$

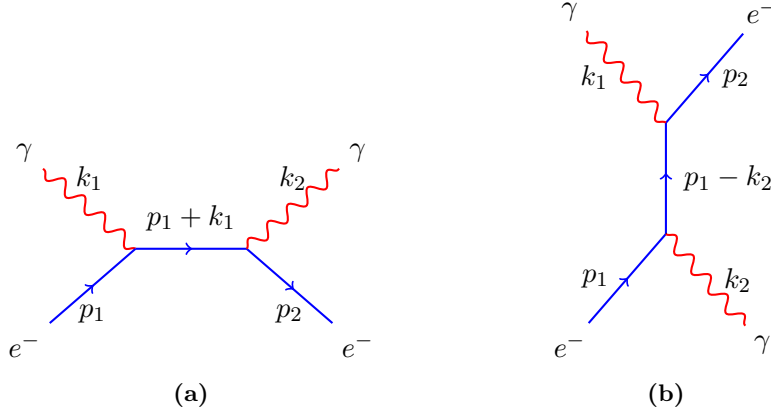


Figure 3.3: Feynman diagrams for the lowest order terms in the Compton Scattering cross section - Fig. 3.3a shows a s-channel diagram and Fig. 3.3b shows an u-channel diagram.

The first diagram describes the absorption of the incoming photon by the electron followed by the emission of the final photon. The second diagram corresponds to the process in which the electron emits the final photon before absorbing the incoming photon. They present two contributions to the amplitude of the reaction $\mathcal{M} = \mathcal{M}_s + \mathcal{M}_u$.

Using the Feynman rules one can write down an expression for quantum mechanical amplitude \mathcal{M} [82]:

$$i\mathcal{M} = \bar{u}(p_2)(-ie\gamma^\mu)\epsilon_\mu^*(k_2)\frac{i(\not{p}_1 + \not{k}_1 + m)}{(p_1 + k_1)^2 - m^2}(-ie\gamma^\nu)\epsilon_\nu(k_1)u(p_1) + \\ + \bar{u}(p_2)(-ie\gamma^\nu)\epsilon_\nu(k_1)\frac{i(\not{p}_1 + \not{k}_2 + m)}{(p_1 - k_2)^2 - m^2}(-ie\gamma^\mu)\epsilon_\mu^*(k_2)u(p_1), \quad (3.4)$$

where p_i and k_i are the four-momenta of the electron and photon respectively, $u(p_i)$ are the Dirac spinors, γ^μ are the Dirac matrices, $\epsilon_\mu(k_i)$ stands for the polarization vector of the initial or final state of the photon and $\not{p} = \gamma_i p^i$ is the Feynman slash notation.

3.1.2.2 Compton cross section

Starting from the Eq. 3.4 it is possible to obtain the expression for the squared amplitude [82]

$$\frac{1}{4} \sum_{spins} |\mathcal{M}|^2 = 2e^4 \left[\frac{p_1 k_2}{p_1 k_1} + \frac{p_1 k_1}{p_1 k_2} + 2m^2 \left(\frac{1}{p_1 k_1} - \frac{1}{p_1 k_2} \right) + m^4 \left(\frac{1}{p_1 k_1} - \frac{1}{p_1 k_2} \right)^2 \right] \quad (3.5)$$

To turn this expression into a cross section we must calculate an element of the two-body phase space:

$$d\Phi_2 = \delta^4(p_1 + k_1 - p_2 - k_2) \frac{d^3 p_2 d^3 k_2}{(2\pi)^6 4E_2 e w_2} \quad (3.6)$$

and then substitute it into the following expression for the cross section:

$$d\sigma = \frac{(2\pi)^4 |\mathcal{M}|^2}{4\sqrt{(p_1 k_1)^2}} d\Phi_2. \quad (3.7)$$

At this point we should decide on a frame of reference and draw a picture of the kinematics. In this context, it is very useful to employ the variables that are the Lorentz invariants. A useful choice is given by the Mandelstam variables [82, 83] denoted by s , t , u . For the Compton scattering the Mandelstam variables are given by

$$s = (p_1 + k_1)^2 = (p_2 + k_2)^2 = m^2 + 2p_1 k_1 = m^2 + 2p_2 k_2 \quad (3.8)$$

$$t = (p_1 - p_2)^2 = (k_1 - k_2)^2 = 2(m^2 - p_1 p_2) = -2k_1 k_2 \quad (3.9)$$

$$u = (p_1 - k_2)^2 = (p_2 - k_1)^2 = m^2 - 2p_1 k_2 = m^2 - 2p_2 k_1 \quad (3.10)$$

$$s + t + u = 2m^2 \quad (3.11)$$

In the Center of Mass reference frame (CMS), the invariant variable s has the physical meaning which is the square of the total energy of the colliding particles $s = E_{cm}^2 = (E_1 + E_2)^2 = (E_3 + E_4)^2$, where E_i is the energy of the i - particle.

Writing Eq. 3.7 in terms of the Mandelstam variables s , t and u , one eventually obtains:

$$d\sigma = 8\pi r_e^2 \frac{m^2 dt}{(s - m^2)^2} \left[\left(\frac{m^2}{s - m^2} + \frac{m^2}{u - m^2} \right)^2 + \left(\frac{m^2}{s - m^2} + \frac{m^2}{u - m^2} \right) - \frac{1}{4} \left(\frac{s - m^2}{u - m^2} + \frac{u - m^2}{s - m^2} \right) \right]. \quad (3.12)$$

Compton scattering is most often analyzed either in the frame in which the electron is initially at rest or in the center of mass frame.

3. THEORETICAL INTRODUCTION FOR INNOVATIVE SCHEMES

Rest frame: the cross section can be expressed in terms of energy of the incident photon ω'_1 and scattered angle θ' (see Fig. 3.1). A prime sign refers to the variables in the rest frame of the electron. The four-momentum conservation $p_1 + k_1 = p_2 + k_2$ implies

$$\omega'_2 = \frac{\omega'_1}{1 + \frac{\omega'_1}{m_e}(1 - \cos \theta')}, \quad (3.13)$$

which is a formula for Compton shift as well as a relation between the energy of scattered photon and angle of observation. For scattering of unpolarized light by unpolarized electrons, the differential cross section is given by

$$\frac{d\sigma}{d\Omega'} = \frac{r_0^2}{2} \left(\frac{\omega'_2}{\omega'_1} \right)^2 \left(\frac{\omega'_1}{\omega'_2} + \frac{\omega'_2}{\omega'_1} - \sin^2 \theta' \right). \quad (3.14)$$

This is the so-called *Klein-Nishina formula* which gives the differential cross section of photons scattered from a single electron (see Fig. 3.4). As it was expected, for low photon energies $w'_1 \ll m_e$, from Eq. 3.13 it is clear that $w'_2 \rightarrow w'_1$ and cross section approximately equals to the classical Thomson cross section Eq. 3.1.

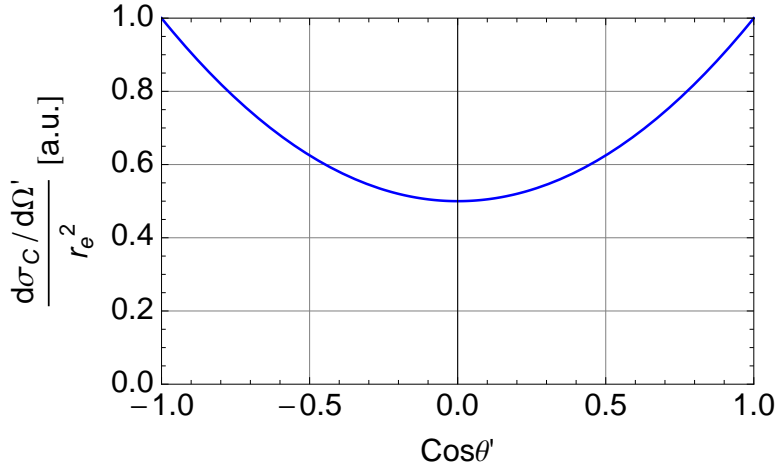


Figure 3.4: Compton differential cross section in the rest frame of reference - Differential cross section for Compton scattering of $w_1 = 1.17$ eV photons by electrons which are initially at rest.

Center of mass frame: The kinematics of the reaction is shown on Fig. 3.5.

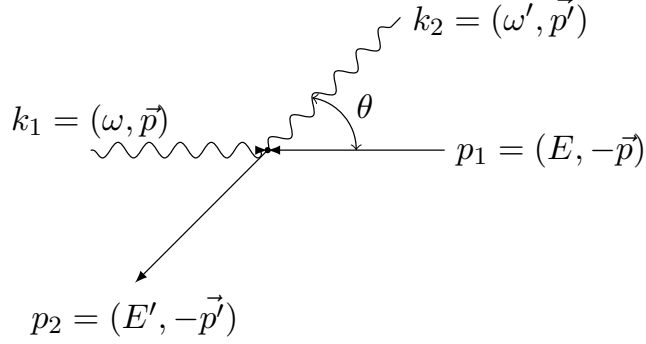


Figure 3.5: The kinematics of the Compton scattering in the center of mass reference frame - A total center of mass energy $\sqrt{s} = (E + \omega)$.

Evaluating spin averaged squared amplitude given by Eq. 3.4 considering $E \gg m_e$ and $\theta \approx \pi$ (high energy behavior), one can obtain:

$$\frac{1}{4} \sum_{spins} |\mathcal{M}|^2 \approx 2e^4 \left(\frac{p_1 k_1}{p_1 k_2} \right). \quad (3.15)$$

Then, calculating the phase-space integral using Eq. 3.6 and plugging it into Eq. 3.7, one get the expression for differential cross section in the CMS frame:

$$\frac{d\sigma}{d\Omega} \approx \frac{1}{2} \frac{1}{2E} \frac{1}{2\omega} \frac{\omega}{(2\pi)^4(E + \omega)} \frac{2e^4(E + \omega)}{E + \omega \cos \theta}. \quad (3.16)$$

Finally, the total cross section:

$$\sigma_C \approx \frac{2\pi\alpha^2}{s} \log \frac{s}{m^2}, \quad (3.17)$$

where s is the square of the total energy of the colliding particles in the CMS, i.e. $s = (E + \omega)^2$.

Scattering from electrons in motion: In our case (laser-electron collisions inside the accelerator), electrons are not at rest, they are moving with relativistic velocities. Whenever a moving electron has energy much greater than that of an incident photon, the energy transfer occurs from electron to photon. This is called the *Inverse Compton scattering*.

According to the intelligent choice of geometry of the collisions (see Fig. 3.6), the Mandelstam variables given by Eq. 3.8, Eq. 3.9, Eq. 3.10 could be readily derived and given by the following expressions:

3. THEORETICAL INTRODUCTION FOR INNOVATIVE SCHEMES

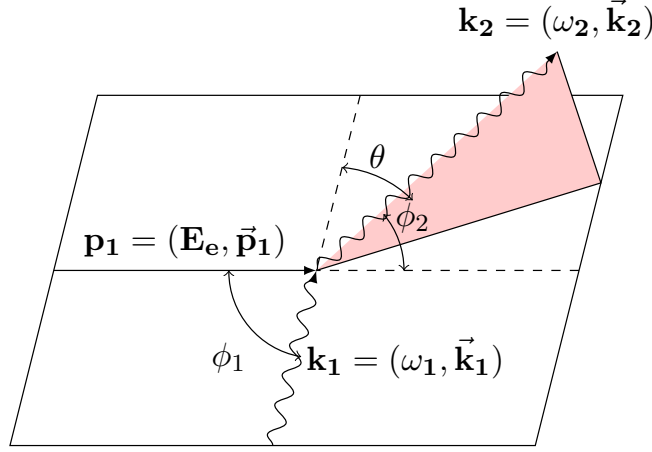


Figure 3.6: The kinematics of Compton scattering in the laboratory frame - The laser photon with the energy ω_1 scatters off the relativistic electron having energy E_e . As a result of the relativistic boost, the high energy photon of energy ω_2 is produced. The scattered electron is not shown.

$$s = m_e^2 + 2\gamma m_e \omega_1 (1 - \beta \cos \phi_1) \quad (3.18)$$

$$t = -2\omega_1 \omega_2 (1 - \cos \theta) \quad (3.19)$$

$$u = m_e^2 - 2\gamma m_e \omega_2 (1 - \beta \cos \phi_2). \quad (3.20)$$

where $\beta = \frac{v}{c}$ is a velocity of the electrons scaled by the speed of light c , $\gamma = \frac{1}{\sqrt{1-\beta^2}}$ is a Lorentz factor (the electron energy in units of the electron rest energy). Introducing the new dimensionless variables as

$$x_1 = \frac{s - m_e^2}{m_e^2} = 2\gamma \frac{\omega_1}{m_e} (1 - \beta \cos \phi_1) \quad (3.21)$$

$$x_2 = \frac{u - m_e^2}{m_e^2} = -2\gamma \frac{\omega_2}{m_e} (1 - \beta \cos \phi_2) \quad (3.22)$$

$$y_{12} = \frac{1}{x_1} + \frac{1}{x_2}, \quad (3.23)$$

for unpolarized states of initial particles and when the spin of the final electron and polarization of the final photon are not observed, the differential cross section Eq. 3.12 in terms of the relativistic invariants is given by

$$\frac{d\sigma}{dt} = 2\pi r_0^2 \frac{1}{(m_e x_1)^2} \left\{ 4y_{12}(1 + y_{12}) - \frac{x_1}{x_2} - \frac{x_2}{x_1} \right\}. \quad (3.24)$$

By using the previous equation, the differential Compton cross section per unit solid angle is obtained as (see [83])

$$\frac{d\sigma}{d\Omega} = 2r_0^2 \left(\frac{\omega_2}{m_e x_1} \right)^2 \left\{ 4y_{12}(1 + y_{12}) - \frac{x_1}{x_2} - \frac{x_2}{x_1} \right\}. \quad (3.25)$$

Fig. 3.7 shows that in the laboratory frame, the Lorentz transformation concentrates the photon flux at small angles ϕ_2 of the order of $1/\gamma$, increasing therefore the photon flux in the forward direction.

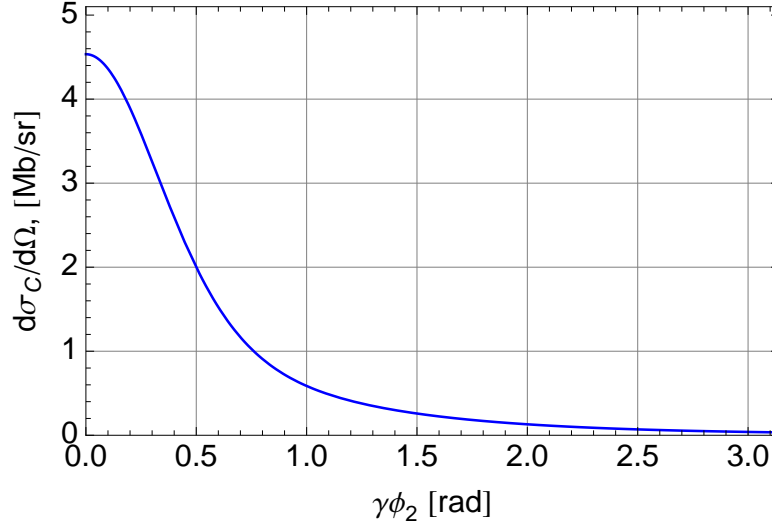


Figure 3.7: Differential Compton cross section versus the observation angle - Differential cross section for the Compton scattering of $w_1 = 1.17$ eV laser photons by $E_e = 2$ GeV electrons at incident angle $\phi_1 = \pi$ as the function of the observation angle ϕ_2 expressed in the units of $\frac{1}{\gamma}$.

In real experiments, when the laser pulse scatters off the electron beam and not a single electron, the resulting angular aperture of the scattered photons is given by the convolution between the $1/\gamma$ aperture cone and electron beam angular spread.

Finally, making the substitution of variables using Eq. 3.21, Eq. 3.22, Eq. 3.24, remembering that x_1 is fixed by initial conditions and integrating over x_2 the total cross section is obtained in the following form:

$$\sigma_C = 2\pi r_0^2 \frac{1}{x_1} \left[\left(1 - \frac{4}{x_1} - \frac{8}{x_1^2} \right) \ln(1 + x_1) + \frac{1}{2} + \frac{8}{x_1} - \frac{1}{2(1 + x_1)^2} \right]. \quad (3.26)$$

3. THEORETICAL INTRODUCTION FOR INNOVATIVE SCHEMES

For the Compton scattering of the laser light, one usually has $x_1 \ll 1$ that corresponds $\gamma w_1 \ll m_e$. Then, the total cross section as a function of x_1 can be expanded into Taylor Series and so

$$\sigma_C \approx 2\pi r_0^2 \frac{4}{3}(1 - x_1) \approx \sigma_T(1 - x_1) \quad (3.27)$$

the total Compton cross section is nearly equal to the classical Thomson cross section. In the opposite case, when $x_1 \gg 1$, i.e. ultrarelativistic case, the expansion of the Eq. 3.26 gives the following asymptotic solution:

$$\sigma_C \approx 2\pi r_0^2 \frac{1}{x_1} \left(\ln x_1 + \frac{1}{2} \right). \quad (3.28)$$

The behavior of the total Compton cross section in the low and high energy limit can be observed on Fig. 3.8. The overall effect caused by quantum corrections comes out in the reduction of the scattering cross section relative to the Thomson cross section at high energies and thus at high energies Compton scattering becomes less efficient.

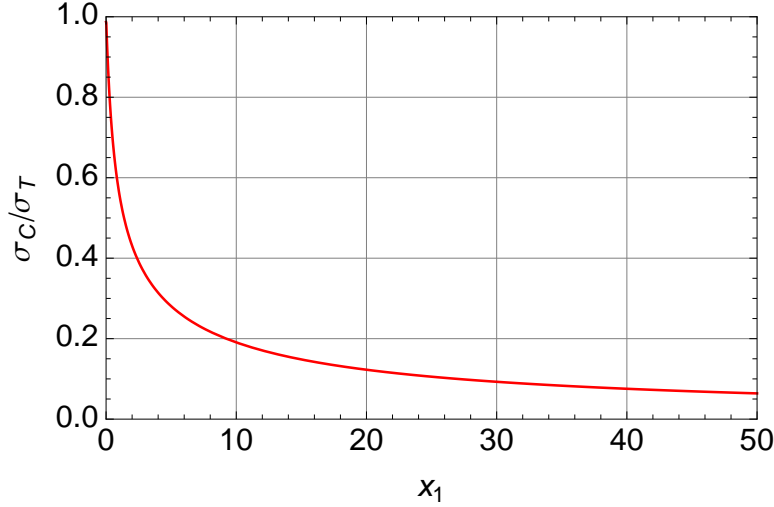


Figure 3.8: Total unpolarized Compton cross section - Total Compton cross section as a function of the dimensionless parameter x_1 , given by the Eq. 3.21. Compton cross section trends toward the classical Thomson cross section at small x_1 (low energies) and significantly decreases in the ultrarelativistic limit.

3.1.2.3 Energy boost of the low energy photons

The Inverse Compton Scattering is an important physical process used in several contexts to generate high energy photons, in our case for polarized positron production.

In this process, relativistic electrons ($\beta \approx 1$) transfer part of their kinetic energy to the low energy photons. This situation occurs when the electron momentum $p_e \gg m_e c$, the angular distribution of the scattered photons in this case is strongly concentrated within a cone of an opening angle $\sim 1/\gamma$ around the direction of motion of the initial electrons (see Fig. 3.7). Since, in the observer frame, *i.e.* laboratory frame, the photons are backscattered with a significant energy boost, this process is also known as *Compton backscattering*. The maximum energy of the scattered photons is reached in the “head-on” collision geometry (see Fig 3.9b).

The kinematics of the considered process in the laboratory frame is shown on Fig. 3.6. On Fig. 3.6, the initial photon and the electron energies are expressed as ω_1 and $E_e = \gamma m_e c^2$, respectively; ϕ_1 is an angle between the momentum of the incident electron and the photon’s one; ϕ_2 is an angle between the momentum of the scattered photon and the incident electron; θ is an angle between the momentum of the scattered and the incident photons.

According to the principle of four-momentum conservation, the energy of the scattered photons ω_2 is given by [47]

$$\omega_2 = \frac{\omega_1(1 - \beta \cos \phi_1)}{1 - \beta \cos \phi_2 + \frac{\omega_1}{E_e}(1 - \cos \theta)} \quad (3.29)$$

For the electron at rest in the laboratory frame, this expression takes again the form Eq. 3.13.

In the case of Compton scattering of low energy photons (laser light) by relativistic electrons ($\gamma \gg 1$), the energy of the scattered photons at the small angles ϕ_2 in forward direction becomes rather large:

$$\omega_2 \approx \frac{2\gamma^2 \omega_1 (1 - \cos \phi_1)}{1 + (\gamma \phi_2)^2 + 2\gamma \frac{\omega_1}{m_e} (1 - \cos \theta)} \quad (3.30)$$

For “head-on” collisions, where $\phi_1 = \pi$, $\theta = \pi - \phi_2 \approx \phi_1$, the scattered photons follow the incident electron direction, as it was mentioned before and their energy becomes:

$$\omega_2 \approx \frac{4\gamma^2 \omega_1}{1 + (\gamma \phi_2)^2 + 4\gamma^2 \frac{\omega_1}{E_e}}, \quad (3.31)$$

3. THEORETICAL INTRODUCTION FOR INNOVATIVE SCHEMES

and when $\phi_2 = 0$, i. e. backscattering, w_2 will reach the maximum value:

$$\omega_2 \approx \frac{4\gamma^2\omega_1}{1 + 4\gamma^2\frac{\omega_1}{E_e}}. \quad (3.32)$$

When it is possible to neglect the recoil term which is $4\gamma^2\frac{\omega_1}{E_e} \ll 1$, one can obtain a frequently used expression for the highest possible scattered photon energy (so-called energy cutoff or Compton edge):

$$\omega_2^{max} \approx 4\gamma^2\omega_1. \quad (3.33)$$

Eq. 3.33 illustrates how the relativistic electrons eventually boost the energy of the low energy photons. It should be pointed out, that a maximum gain in energy of the scattered photons is proportional to $\sim 4\gamma^2$, therefore by using the relativistic electrons ($\gamma \gg 1$) with laser light ($\gamma\omega_1 \ll m_e c^2$), it is possible to produce the high energy photons well in a range starting from keV (X-ray domain) and up to the MeV scale (gamma ray domain) (see Fig. 3.9).

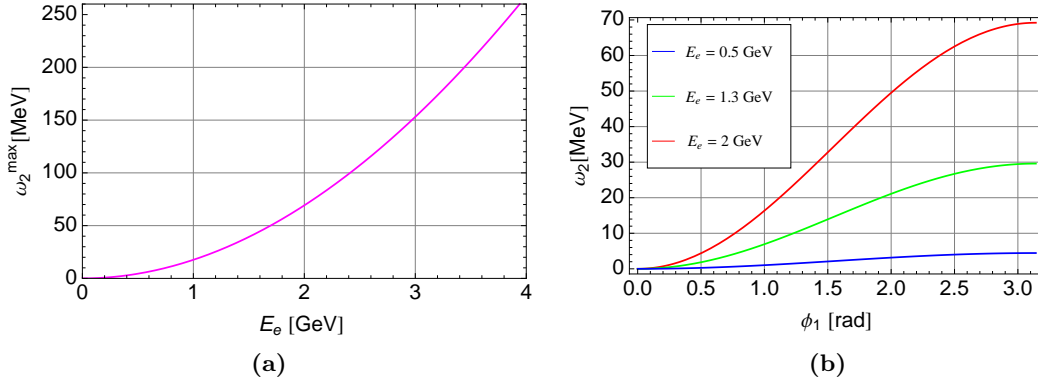


Figure 3.9: Energy of the scattered high energy photons - Fig. 3.9a shows the dependence of the energy cutoff of scattered high energy photons on the electron energy. For the electron energy of 2 GeV it is equal to ~ 72 MeV. For a fixed observation angle $\phi_2 = 0$, the scattered photon energy as a function of the incident angle ϕ_1 for different electron energies is shown on Fig. 3.9b. The maximum of the photon energy is reached in the "head-on" geometry where $\phi_1 = \pi$.

The effect of angular shrinking given by the relativistic boost is illustrated on Fig. 3.10 where the angular dependence of the scattered photons for different electron energies is shown. One can see that the emission cone shrinks as the electron

energy increases. Concerning the energy of the scattered photons, it decreases rapidly with the increasing of the observation angle ϕ_2 as illustrated on Fig. 3.10.

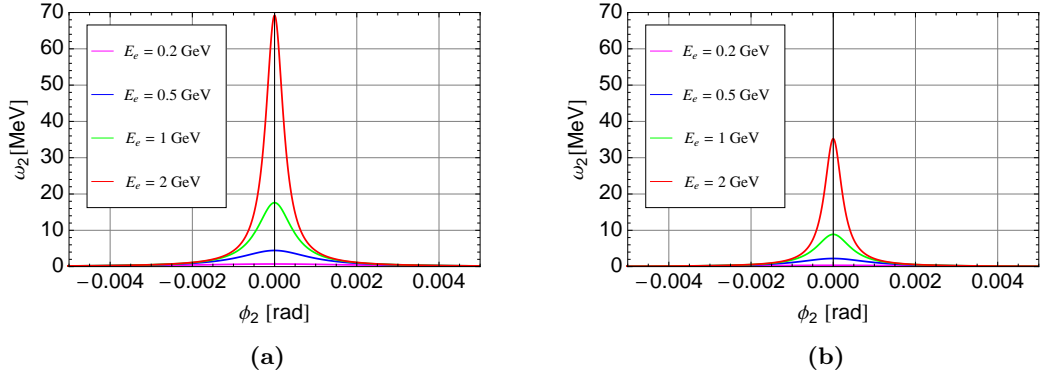


Figure 3.10: Energy of scattered high energy photons for the "head-on" and orthogonal collision geometry - Scattered photon energy for different values of the electron energy at incident angle $\phi_1 = \pi$ (Fig. 3.10a) and $\phi_1 = \frac{\pi}{2}$ (Fig. 3.10b). As expected, a factor of two in the scattered photon energy is visible by comparing the two collision geometries. As the result of the relativistic boost, for the higher electron energies the emission cone is getting narrower.

3.1.2.4 Polarized Compton cross section

Let's consider the "head-on" collision geometry of an electron with the laser photon where $\phi_1 = \pi$ (see Fig. 3.6). A reference system where z-axis is directed along the electron momentum is chosen. The initial polarization state of the electron is described by the polarization vector $\vec{\zeta}$ in such a way that its longitudinal components $\zeta_3 = 2\lambda_e \equiv P_z$, where λ_e is the mean electron helicity ($|\lambda_e| \leq \frac{1}{2}$). The initial polarization state of the laser photon is determined by the photon polarization vector (Stokes vector) $\vec{\xi}$. In this case, $P_c = \xi_3$ stands for the degree of the circular polarization and $P_l = \sqrt{\xi_1^2 + \xi_2^2}$ is the degree of linear polarization. In the framework of the polarized positron sources, the high energy photons produced by the Compton scattering should have circular polarization in order to produce the longitudinally polarized positrons [83].

The total Compton cross section can be written then as a sum of two terms [84]:

$$\sigma_c = \sigma_c^{np} + 2\lambda_e P_c \sigma_1, \quad (3.34)$$

3. THEORETICAL INTRODUCTION FOR INNOVATIVE SCHEMES

where σ_c^{np} is the Compton cross section for unpolarized particles given by Eq. 3.26 and σ_1 given as

$$\sigma_1 = \frac{2\sigma_0}{x_1} \left(\left(1 + \frac{2}{x_1}\right) \ln(1 + x_1) - \frac{5}{2} + \frac{1}{x_1 + 1} - \frac{1}{2(1 + x_1)^2} \right), \quad (3.35)$$

where σ_0 is given by

$$\sigma_0 = \pi \left(\frac{e^2}{mc^2} \right) = 2.5 \times 10^{-25} \text{ cm}^2. \quad (3.36)$$

The variable x_1 is given by Eq. 3.21 and in the case of the “head-on” collisions when $\phi_1 = \pi$ is equal to $4\gamma^2 \frac{\omega_1}{E_e}$.

As one can see from Eq. 3.34, the total Compton cross section for the polarized initial states differs from the unpolarized case only if the laser photons are circularly polarized and the electrons have non zero longitudinal component of the polarization vector ($\zeta_3, \xi_3 \neq 0$). For the intermediate electron energy, e.g. below 2 GeV ($\omega_1=2.41$ eV), the total cross section depends slightly on the polarization state of the initial particles what can be seen by the ratio σ_1/σ_c^{np} which is in this case $|\sigma_1/\sigma_c^{np}| < 0.02$. However, the energy spectrum does experience quite strong dependence on the initial polarization states.

The energy spectrum of the scattered gamma rays is given by the differential scatter cross section as [84]:

$$\frac{1}{\sigma_c} \frac{d\sigma_c}{dy} = \frac{2\sigma_0}{x_1\sigma_c} \left(\frac{1}{1-y} + 1 - y - 4r(1-r) + 2\lambda_e P_c r x_1 (1-2r)(2-y) \right), \quad (3.37)$$

where λ_e is a mean electron helicity and P_c stands for the laser photon degree of the circular polarization and

$$y = \frac{\omega_2}{E_e} \leq y_m = \frac{x_1}{x_1 + 1} \quad (3.38)$$

$$r = \frac{y}{x_1(1-y)} \leq 1. \quad (3.39)$$

The differential cross section dependence on the energy of the scattered high energy photons and polarization states is shown on Fig. 3.11 for different electron energies. At higher electron energies, the asymmetry between $\zeta_3\xi_3 = \pm 1$ states becomes very large. In such a way, according to Fig. 3.11b for the $\zeta_3\xi_3 < 0$ case the number of the scattered photons in the Compton edge is higher in respect of the $\zeta_3\xi_3 > 0$ case. For the relatively low electron energy (< few GeV), the impact of the polarization on the

3.1 Compton effect

scattered photon energy spectrum is quite low (see Fig. 3.11a). Thus, in the case of 2 GeV electron energy, the different states of the initial polarization introduce $\sim 7\%$ variation in the differential cross section taken at the Compton edge energy ω_2^{max} .

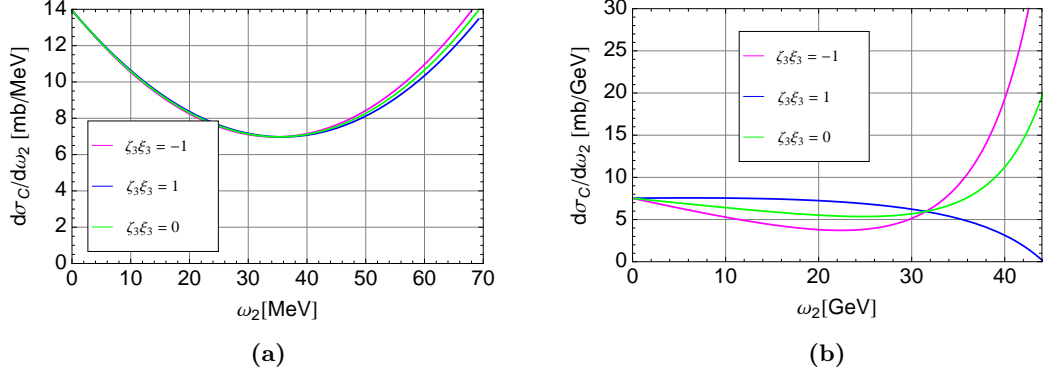


Figure 3.11: Differential Compton cross section for different energies and polarization configurations (energy spectrum) - Energy spectra of the scattered high energy photons for different electron and laser photon energies. Fig. 3.11a shows the energy spectrum in the case of the laser photon energy $w_1 = 1.17$ eV and electron energy $E_e = 2$ GeV whereas for a Fig. 3.11b $w_1 = 2.41$ eV and $E_e = 60$ GeV have been used. At energy 2 GeV and smaller the energy spectrum depends slightly on the polarization of the initial states, nevertheless it does strongly depends for the higher electron energies.

The angular distribution of the scattered photons $d\sigma/d\Omega$ is derived from the Eq. 3.37 – 3.39 and illustrated on Fig. 3.12a and Fig. 3.12b. Therefore,

$$\frac{d\sigma}{d\Omega} = \frac{2\sigma_0 y_m}{\pi\phi_{02}^2 x_1 \left(1 + \left(\frac{\phi_2}{\phi_{02}}\right)^2\right)^2} \left(\frac{1}{1 - y(\phi_2)} + 1 - y(\phi_2) - 4r(1 - r) + \right. \\ \left. + 2\lambda_e P_e r x_1 (1 - 2r)(2 - y(\phi_2)) \right) \quad (3.40)$$

where

$$y(\phi_2) = \frac{y_m}{1 + \left(\frac{\phi_2}{\phi_{02}}\right)^2}. \quad (3.41)$$

At energies lower than a few GeV (Fig. 3.12a), regardless of the polarization state of the initial particles, the distribution has a sharp peak in the vicinity of $\phi_2 = 0$ in the direction of the incident electron momentum. For the higher energies as shown on Fig. 3.12b, the asymmetry between $\zeta_3\xi_3 = \pm 1$ states becomes more important.

3. THEORETICAL INTRODUCTION FOR INNOVATIVE SCHEMES

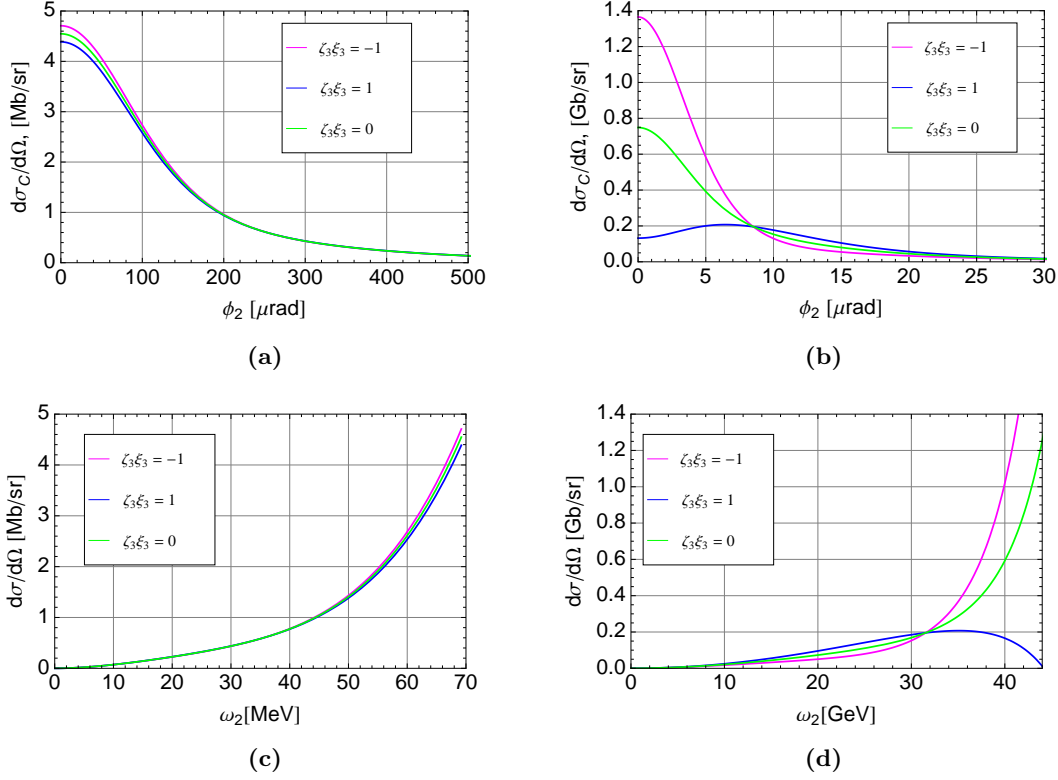


Figure 3.12: Differential Compton cross section for different energies and polarization configurations (angular spectrum) - Fig. 3.12a and 3.12b show the angular spectra of the scattered high energy photons whereas the energy spectra per unit solid angle are presented on Fig. 3.12c and 3.12d. The spectra are plotted for different electron and laser photon energies. In the case of Fig. (3.12a, 3.12c) the laser photon energy $w_1 = 1.17$ eV and electron energy $E_e = 2$ GeV while for Fig. (3.12b, 3.12d), $w_1 = 2.41$ eV and $E_e = 60$ GeV.

By using the following dependence of the scattered photon energy on the emission angle:

$$\omega_2 = \frac{\omega_2^{max}}{1 + \left(\frac{\phi_2}{\phi_{02}}\right)^2} \quad (3.42)$$

$$\phi_{02} = \frac{m_e c^2}{E_e} \sqrt{x_1 + 1} \quad (3.43)$$

and plugging it into Eq. 3.40 one can get the energy spectrum of the scattered photons per unit solid angle. It is presented on Fig. 3.12c and Fig. 3.12d for different electron energies and polarization states.

Eq. 3.42 and Eq. 3.43 give the meaning of the ϕ_{02} angle as well. In such a way, the scattered photons emitted at the angles $\phi_2 < \phi_{02}$ have the energies which are $\omega_2 > \omega_2^{max}/2$. In the case of $E_e = 2$ GeV and $E_e = 60$ GeV electron energy, the angle ϕ_{02} is equal to 260 μ rad and 15.3 μ rad respectively. According to Fig. 3.12 one can, to a good approximation, assume that a half or more of the scattered photons are emitted within a solid angle with the aperture of $\phi_2 \lesssim \phi_{02} \sim 1/\gamma$ [85].

The degree of circular polarization of the scattered photons ξ_{3f} is given in [86] and can be written as

$$\xi_{3f} = \frac{\left(2\lambda_e r x_1 \left(1 + (1-y)(1-2r)^2\right) + P_c(1-2r)\left(\frac{1}{1-y} + 1-y\right)\right)}{\left(\frac{1}{1-y} + 1-y - 4r(1-r) + 2\lambda_e P_c r x_1(1-2r)(2-y)\right)}, \quad (3.44)$$

where λ_e is the mean electron helicity, P_c is the laser photon degree of the circular polarization and x_1 , y , r are given by Eq. 3.21, Eq. 3.38, Eq. 3.39 respectively.

If the electron beam or laser light are polarized, the scattered photons have a considerable degree of polarization. Therefore, when electrons have the longitudinal polarization or laser photons are circularly polarized, the scattered high energy photons have circular polarization as well (see Fig. 3.13) what is indeed required for the polarized positron source.

The energy dependence of the scattered photon degree of circular polarization is shown on Fig. 3.13. The asymmetry between $\zeta_3 \xi_3 = \pm 1$ states is more significant at higher electron energies. Fig. 3.13 also illustrates that at intermediate electron energies (in our case ~ 2 GeV) in the absence of laser photon circular polarization, that is $\xi_3 = 0$,

3. THEORETICAL INTRODUCTION FOR INNOVATIVE SCHEMES

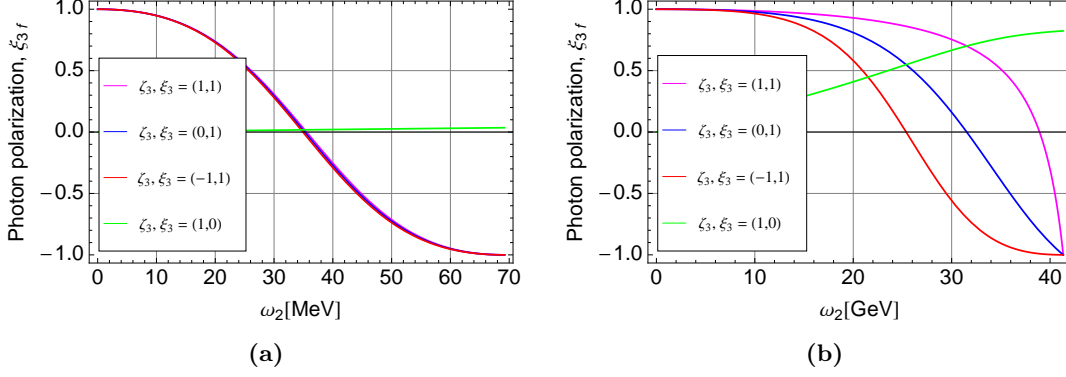


Figure 3.13: The degree of circular polarization of the scattered photons for different polarization configurations - Fig. 3.13a shows the energy dependence of the degree of circular polarization of the scattered photons in the case of the laser photon energy $w_1 = 1.17$ eV and electron energy $E_e = 2$ GeV whereas for Fig. 3.13b $w_1 = 2.41$ eV and $E_e = 60$ GeV have been used.

the Compton scattering does not result in the production of circularly polarized high energy photons.

It should be pointed out that for the boundary case when the degree of the circular polarization $\xi_3 = \pm 1$, the degree of the circular polarization of the scattered photons taken at ω_2^{max} energy is $\xi_{3f} = -\xi_3$.

However, in the real experiments, the electron bunch interacts with the laser pulse producing the total energy spectrum of the scattered photons having energies from ω_1 up to ω_2^{max} as shown e.g. on Fig. 3.11. In this case, at electron energies suitable for the polarized positron production¹, the average polarization of all the scattered photons is nearly zero (see Fig. 3.13a). But kinematics of the Compton scattering sets well-defined relations between the scattered photon energy, its scattering angle and polarization (see Eq. 3.29 and Eq. 3.44). Therefore, by collimating the distribution of scattered photons (i.e. by doing an angular and so the energy selection) one can reach a certain degree of scattered photon polarization.

¹Usually, the electron energy required for the Compton polarized positron sources is chosen relying on the positron accelerating capture system and lies in the range of 1–3 GeV.

3.2 Low energy applications of the Compton scattering

3.2.1 X- and gamma rays

X-rays and gamma rays as a tool for scientific investigations are extremely useful in the fields of medicine, material studies, cultural heritage preservation and archeology as well as in fundamental and applied physics, chemistry and biology. The experiments with synchrotron radiation sources already confirmed that the use of narrowband X-ray beams extends substantially the capabilities of these applications in medicine [87], material studies [88] etc.. Numerous modern attractive methods of X-ray diagnostics are emerging. However, further development and practical applications of these methods depend on the availability of a compact X-ray sources suitable for installation in medical centers, hospitals, museums, scientific laboratories.

In this framework, an accelerator driven Compton based photon sources generate a lot of interest since the rapid advancement in laser and accelerator technologies allows envisaging their utilisation for ultra-compact photon sources. Usually, two different energy regimes are distinguished for the Compton source operation:

1. **X-ray regime:** a laser pulse is scattered off the relatively low energy electron beam (usually tens of MeV) what results in the production of photons in X-ray energy range (1–200 keV). This allows the design of compact, inexpensive, brilliant and narrowband X-ray sources. Moreover, the univocal dependence between the emitted photon energy and its scattering angle (see Eq. 3.29) gives the possibility to obtain a quasi-monochromatic beam by a simple collimation system. For the most ambitious projects the envisaged performances take into account a rate of $10^{12} - 10^{13}$ photons per second, an angular divergence of a few mrad, an X-ray energy cutoff of few tens of keV with a bandwidth of $\Delta E/E \sim 1 - 10\%$. Even if the integrated rate cannot compete with the synchrotron radiation sources, the cost and the compactness of these Compton based machines make them attractive for a wide spectrum of applications. One such machine, ThomX [89] will be built in Orsay (France) in the very near future and will demonstrate the interest of these compact Compton sources for a wide scientific community.
2. **Gamma ray regime:** due to the quadratic dependence of the Compton energy cutoff on the electron beam energy (see Eq. 3.33), it is easy to imagine harder

3. THEORETICAL INTRODUCTION FOR INNOVATIVE SCHEMES

photon production. In this case, a laser pulse is scattered off the middle energy electron beam (from hundreds of MeV to a few GeV) what results in the production of photons in the gamma ray energy range (above 1 MeV). This allows one to envisage different applications in the nuclear waste management and treatment industry [90] and in the field of nuclear isotope detection applied to infrastructures security. In this framework the atomic number identification by means of hard X- or gamma rays allows for nuclear application of the Compton scattering [91]. As an example, an Extreme Light Infrastructure - Nuclear Physics (ELI-NP) facility [92] now is under construction in Magurele (near Bucharest/Romania). It will focus on nuclear phenomena and their practical applications. The gamma source of ELI-NP will produce a very intense and brilliant gamma ray beam (≤ 19 MeV), which is obtained by Compton scattering of a high power laser beam off a very intense electron beam (≤ 0.7 GeV).

3.2.2 Application fields

Cultural heritage Compton compact sources are extremely interesting as far as the chemistry component analysis field is concerned. One of the most promising applications is the cultural heritage preservation and associated domains. Nowadays the main research activities, carried out in the laboratories working in the cultural heritage field, focus on the identification of materials from a chemical and structural point of view (mineral, organic, hybrid, condense matter), the study of processes used for the elaboration of the works of art (origin of the materials, recipes of chemical synthesis, metallurgy, mechanical treatments and thermal annealing) and the study of alteration and ageing behavior, including the issues concerning the preventive conservation and the restoration. The applied techniques provide precious information for the dating of the work of art, the employed techniques and the attribution [93]. Carbon detection can show the primitive sketch of the original drawing thus revealing the modifications during its realisation. Non destructive analysis of paintings permits also to reveal underlying drawings. A painting from Vincent Van Gogh has been recently revealed by X-rays analysis [94]. A size of the Compton compact X-ray machine gives the possibility to place it in an integrated laboratory inside the Museums. This gives to the experts the direct access to the masterpieces and the possibility to avoid external facilities, which involve extremely important insurance, security and transportation costs.

3.2 Low energy applications of the Compton scattering

Medical science As far as the medical science applications are concerned an important benefit is, first of all given in the imaging field by the development of the phase contrast method. Other applications are possible [95, 96, 97], for example, in static and dynamic imaging, 3D compression-less mammography [98] and bronchography. Another very important developing field is the K-edge radiography and therapy. In this framework an important feature of Compton sources is the tunability to a specific wavelength obtainable by varying the energy of the electron beam (quadratic dependence) or the wavelength of the impinging laser (linear dependence). This is attractive since a resonant reaction can be triggered by the interaction between X-rays with a specific energy, and an electronic shell of a contrast agent (like K-shell extraction with a subsequent energy release by Auger cascade).

Imaging applications The K-edge digital subtraction imaging (KEDSI) method utilizes the sharp rise in a given element photoelectric component of the attenuation coefficient at the binding energy of the K-electrons (e.g. 33.17 keV for *I*, 34.56 keV for *Xe*, 50.25 keV for *Gd*). Depending on the specific needs and constraints, experiments can be carried out either using two beams of energies bracketing the K-edge or by a single beam set at energy above the K-edge. In the first case, the technique is indicated as “energy subtraction” and the map of the contrast agent concentration is obtained by logarithmically subtracting the two energy images. In the second case, indicated as “temporal subtraction mode”, the map is obtained by logarithmically subtracting the images taken at energy above the K-edge, before and after the injection of the contrast agent.

The phase contrast imaging technique based on the recording of the phase variations occurring when X-rays pass through matter, has been demonstrated as an extremely powerful method since it permits contrast resolution of soft tissues (even if the elemental composition is almost uniform and the density variations are small) with far lower absorbed dose levels than with a conventional system. This is in particular the case for breast, lung and articular cartilage tissues.

Therapy applications The Stereotactic Synchrotron Radiation Therapy (SSRT) consists in irradiating a tumour loaded with a contrast agent with quasi-monochromatic X-rays tuned at the energy above the K_{α} line of the contrast agent. The requested

3. THEORETICAL INTRODUCTION FOR INNOVATIVE SCHEMES

bandwidth is not a tight constraint and is naturally achieved with Inverse Compton Scattering without the need of a monochromator. The photoelectric interactions generate photoelectrons, X-ray fluorescence and Auger electrons with the consequent cascade, which in turn increases the local radiation dose. In the energy range of medical imaging (15–120 keV), the photoelectric effect plays a dominant role. As it displays a Z^{3-5} -dependency, where Z is the atomic number, heavy elements absorb X-rays more strongly than the biological tissue light elements. This technique can be slightly optimized by loading the tumour with cisplatinum. The X-ray beam will induce a dose enhancement due to the high Z value of Pt in parallel with direct DNA damage as the usual effect of cisplatinum [99, 100]. In SSRT, the best survival curves were obtained by Biston et al. [99].

Nuclear applications Gamma rays play an important role in Nuclear Physics, in particular for security applications and nuclear waste treatment. One of the methods to eliminate (decrease) the radioactivity of nuclear waste is its transmutation via a nuclear reaction to produce shorter-lived or more stable nuclides. Gamma rays can induce these nuclear reactions, which will shorten the radioactive life of nuclear waste [101]. Using the gamma rays, generated by Compton scattering, the efficiency of the nuclear reactions can be significantly improved. Due to the relatively high monochromaticity degree and the high brightness of the gamma rays produced by the Compton scattering, the coupling between these gamma rays and the giant resonance of nuclei is better than that of the bremsstrahlung method [102]. This topic is extremely important, especially during this period following the 2011 Tōhoku earthquake in Japan, where the nuclear waste field is revealing its fundamental role in applied sciences.

3.3 Production schemes for the polarized positron sources

In the previous section the main characteristics of the Compton scattering process have been illustrated. This allow to estimate the gamma ray flux produced, the polarization effects and the recoil of the scattering electrons in the context of the polarised positron sources. The recoil effect is extremely important, since due to the quadratic dependence of the scattered photon energy with the electron energy, for ultra-relativistic beams it can strongly deteriorate the beam quality in the longitudinal phase space. This does

3.3 Production schemes for the polarized positron sources

not represent a bottleneck for the “single pass” sources where the electron beam is discarded immediately after the Compton interaction. Nevertheless, it is the main limitation factor for the “multi pass” systems, like the Compton rings or the ERL sources already described in section 2.6.

In this framework we should recall that the main challenge of the LC’s Compton based polarized positron source is to produce the gamma ray flux sufficient to obtain the positron charge required. In this context there are three different options.

The first one, assuring the high instantaneous gamma ray production rate is a so-called Compton Linac production scheme. It employs collisions between high charge electron bunches from a linac and high power laser pulses. This scheme does not require a positron stacking since the designed positron charge per bunch can be produced in every collision [71]. This discussion is beyond the scope of this thesis.

The other two proposed options concern high repetition rate electron accelerators coupled with high average laser power systems. The two proposals are based on the Compton ring and the ERL production schemes [69, 73]. Both of them represent a “multi pass” system since in the first case the beam is continuously recirculated, in the second the electron beam needs a Multiple Interaction Point Line (MIPL) to compensate for the low ERL electron bunch charge.

Both are good solutions limited by the necessity to stack the positron bunches in the Damping Ring (DR) to reach the requested positron charge. In fact, the stacking efficiency is limited by the size of the RF bucket and the emittance of the injected positrons. Therefore, the turn by turn production of gamma rays should be maximized.

In this context, it is possible to estimate the expected number of scattered gamma rays. Neglecting the divergence of the electron and laser beam at the IP and assuming a Gaussian profile for both, the luminosity \mathcal{L} for the Compton collisions is given by the following equation from [103]:

$$\mathcal{L} = N_e N_{ph} f \frac{\cos(\phi/2)}{2\pi} \frac{1}{\sqrt{\sigma_{ye}^2 + \sigma_{yph}^2} \sqrt{(\sigma_{xph}^2 + \sigma_{xe}^2) \cos^2(\phi/2) + (\sigma_{ze}^2 + \sigma_{zph}^2) \sin^2(\phi/2)}}, \quad (3.45)$$

where N_e , N_{ph} are the number of the electrons in the bunch and number of the photons in the laser pulse respectively, f is the repetition frequency, ϕ is the angle of the collisions, $\sigma_{\vec{r}_e}$ and $\sigma_{\vec{r}_{ph}}$ indicates respectively the RMS sizes of the electron bunch and

3. THEORETICAL INTRODUCTION FOR INNOVATIVE SCHEMES

the laser pulse. The luminosity is independent of the nature of the physical reaction and depends only on the intensities and geometrical dimensions of the colliding beams.

Once the luminosity of the process is defined, the flux of gamma rays (or emitted rate) is given by

$$\mathcal{F} = \frac{dN_\gamma}{dt} = \sigma_c \cdot \mathcal{L}, \quad (3.46)$$

where σ_c is the total Compton scattering cross section which is determined by the momenta of the incident electron and laser photon.

Formulas 3.45 and 3.46 show that the emitted rate is inversely proportional to the electron and laser beam sizes. These formulas shows also that a collision angle reduces the gamma ray flux especially in the case of long electron bunches and laser pulses.

The main scientific objective of Compton based polarized positron source research therefore can be accomplished by using firstly a high average power laser amplified in a Fabry–Perot cavity and a high intensity electron beam. In the second place, as it could be seen from Eq. 3.45 and 3.46, the important parameters are also the sizes of the electron and laser pulses at the Interaction Point (IP) and the collision crossing angle. Thus, a strong laser and electron beam focusing in the IP¹ as well as the smallest possible crossing angle is preferable [104, 105].

Nevertheless, the maximization of the laser power has to take into account the recoil effect on the beam dynamics in the Compton Ring. The recoil of the scattering electrons results in a degradation of the energy spread and in the consequent bunch lengthening reducing the gamma ray production [73, 106]. So, an attempt to increase the gamma ray flux by e.g. increasing the laser power leads immediately to a new equilibrium state between the radiation damping and the laser quantum excitations characterized by the higher value of the longitudinal emittance. This will in turn require a larger longitudinal acceptance to avoid the possible electron beam losses.

To avoid the Compton ring difficulties concerning the longitudinal beam dynamics, the ERL production scheme can be used [69]. In this case the recoil effect is still a

¹The minimum electron and laser beam sizes are limited by hourglass effect. For the electrons, it is given by the relation between the electron bunch length σ_{ze} and the beta function β^* whereas for the laser pulse this relation is defined for the laser pulse length σ_{zph} and Rayleigh length Z_R . One should keep the following relations to avoid the Hourglass effect $\sigma_{ze} \leq \beta^*$, $\sigma_{zph} \leq Z_R$ and $\max(\sigma_{ze}, \sigma_{zph}) < \min(\beta^*, Z_R)$.

3.3 Production schemes for the polarized positron sources

limiting factor due to the MIPL. In every collision point the energy spectrum is deteriorated and the chromatic effect impacts on the gamma production from the following IPs .

In the following, the equilibrium energy spread of the Compton ring and the polarized gamma ray production using the ERL as electron source are going to be discussed.

3.3.1 Compton ring. Dynamical and equilibrium energy spread.

During a revolution an electron loses a fraction of its energy by synchrotron radiation. This energy loss has to be compensated by the energy given by the radio frequency (RF) cavities. The acceleration process by itself results in damping of the longitudinal oscillations limited due to the continuous excitation, so-called quantum excitation. The balance between the radiation damping and quantum excitation is reached at equilibrium defining an area occupied by the electrons in the RF bucket where the particle oscillations are stable.

In general the longitudinal beam dynamics can be described by two coupled variables related to the RF acceleration process and defined with respect to the synchronous particle:

- the energy deviation, $\delta E_j = E_j - E_s$, where E_j and E_s are the energies of any given electron in the bunch and that of the synchronous particle respectively.
- the longitudinal displacement of the electron j from the synchronous particle expressed by the time difference $\delta\tau_j = \tau_j - \tau_s$ ¹.

Since the synchronous particle has zero time difference and has the nominal energy, it is possible to use it as a reference system.

In this context, the motion of the electrons in the longitudinal phase space is described by a second order non linear differential equation [108]. In general, for the electron phase ϕ as one of the canonical variables, it can be written as

$$\ddot{\delta\phi} + \frac{\Omega_s^2}{\cos\phi_s} (\sin\phi_s \cos\phi_s + \sin\delta\phi \cos\phi_s - \sin\phi_s) = 0, \quad (3.47)$$

¹Alternatively the phase of the electron can be used as the second canonical variable to describe the longitudinal motion $\delta\phi_j = \phi_j - \phi_s = \omega_{RF}(\tau_j - \tau_s) = \omega_{RF}\delta\tau_j$, where ω_{RF} is the RF frequency [107].

3. THEORETICAL INTRODUCTION FOR INNOVATIVE SCHEMES

where $\delta\phi = \phi - \phi_s$, ϕ_s is a synchronous phase, Ω_s is the synchrotron frequency. The solutions indicate that electrons oscillate in longitudinal position (phase) and in energy with respect to the synchronous particle [109].

However, the presence of Compton collisions in the ring affects this dynamics by acting on the electron beam energy deviation on the turn by turn basis.

In general, the Compton dynamics of the longitudinal phase space can be evaluated only by the numerical computation. To find the oscillation amplitudes, a numerical solution of the equations of motion is used in which the energy change and the time displacement per revolution are given by

$$\begin{aligned}\delta E_{i,n+1} &= \delta E_{i,n} - U_{synchRad} + V_0 \sin(\omega_{RF}t + \phi_s) - \delta E_{damp} + \delta E_{qe} - \delta E_{compt} \\ \delta \tau_{i,n+1} &= \tau_{i,n} - \alpha \frac{\delta E_{i,n}}{E},\end{aligned}\tag{3.48}$$

where $\delta E_{i,n}$ and $\tau_{i,n}$ are respectively the energy deviation and time displacement of the i -th electron on the n -th turn, $U_{synchRad}$ is the energy loss per turn due to synchrotron radiation, V_0 is the peak voltage of RF cavity, ϕ_s is the synchronous phase, δE_{damp} is the fraction of energy deviation due to damping, δE_{compt} is the fraction of energy deviation due to Compton scattering, δE_{qe} is the fraction of energy deviation given by the quantum excitations, α is the first order momentum compaction factor and E is the electron energy. Reference [109] contains a full description of each term in these equations while the possible calculation of the δE_{compt} term which was done for the longitudinal dynamics studies of the ATF DR at KEK will be discussed in Chapter 5. For this purpose, the direct calculation of the Compton energy spectrum given by Eq. 3.37 is used. The collective effects such as intrabeam scattering, coherent synchrotron radiation, space charge and wakefields certainly also contribute to the dynamics of the electron beam. They can be responsible for the additional energy spread and beam instabilities. Nevertheless, these effects are not taken into account in this study.

The two coupled Eq. 3.48 given the energy oscillations and the associated oscillations of the longitudinal displacement from the bunch center expressed by the correspondent time displacement should be solved together. Thus, it will provide the dynamics and equilibrium of the energy spread and the electron bunch length in the Compton ring.

3.3 Production schemes for the polarized positron sources

The analytical solution for the equilibrium energy spread in the Compton ring is given in [110]. The authors treated the laser field as a static wiggler. In this case, the average energy loss of the electron after passing through the laser pulse is

$$(\Delta E)_\gamma = \frac{32\pi}{3} r_e^2 \gamma^2 \frac{E_L}{z_R \lambda_L} \quad (3.49)$$

where r_e is the classical electron radius, γ is a Lorentz factor or the electron energy in units of the electron rest energy $m_e c^2$, E_L is the laser pulse energy, z_R is the laser Rayleigh length and λ_L is the wavelength of the laser.

In such a way, the equilibrium electron beam energy spread in the Compton ring is given by

$$(\delta E)_{min} \equiv \frac{\sigma_E}{E} = \sqrt{\frac{7}{5} \frac{\lambda_C}{\lambda_L}} \gamma, \quad (3.50)$$

where $\lambda_C = h/m_e c \approx 2.43 \times 10^{-12}$ m is the Compton wavelength of the electron.

For example, when the 1.3 GeV electron beam and 1 μ m wavelength laser is used for the high energy gamma rays generation, it requires the momentum acceptance of $\sim 9\%$ in the Compton ring which is impossible to achieve.

In the same way, the balance between the damping rate and the quantum excitations also leads to the equilibrium value of the transverse emittance:

$$(\epsilon_{x,y}^n)_{min} = \frac{3}{10} \frac{\lambda_C}{\lambda_L} \beta_{x,y}^*, \quad (3.51)$$

where $\beta_{x,y}^*$ is the electron betatron function in the x/y direction at the interaction region. In this case, a small value of the betatron function is preferable to obtain the low emittance electron beam and to focus better the electron beam in the Compton IP.

Therefore, due to the recoil of the scattering electrons during the Compton scattering, the longitudinal dynamics of the electron beam is considered to be a critical point of the Compton ring design.

3.3.2 Compton ring. Polarized and unpolarized equilibrium energy spread by Campbell's theorem.

In this section, a new method to evaluate the equilibrium energy spread in the Compton ring will be introduced. Its main advantage is that it allows easily to extend the calculations for the case of polarized Compton scattering.

3. THEORETICAL INTRODUCTION FOR INNOVATIVE SCHEMES

The essence of the method is that the Compton scattering may be considered as the shot noise process and therefore treated by the Campbell's theorem [111, 112]. The shot noise can be seen as the random fluctuations in the output of the linear systems activated by a sequence of the impulses, e.g. photon emission, occurring at the random time. In general, the Campbell's theorem gives the information about the average value and the variance of the certain probability distribution describing such a process.

It can be demonstrated also that the energy deviation with time will approach a certain distribution (in the absence of the Compton scattering it is a Gaussian distribution [109]). In this case the parameter σ_E that is the standard deviation of this distribution is the energy spread. In such a way, the Campbell's theorem is a tool which gives the energy spread by means of the variance of the energy distribution.

Let's assume that we have a linear system and know its response to a δ -function excitation that in our case is the photon emission (scattering).

$$x(t) = ag(t - t_0), \quad g(\tau) = 0 \text{ for } \tau < 0, \quad (3.52)$$

with a - amplitude of the δ -pulse excitation and $g(t - t_0)$ - response of the system to a δ -pulse excitation.

If such excitations occur randomly in time with the amplitude which has random distribution of the form $\dot{n}(a)$, the variance of the process, given by the Campbell's theorem is

$$\langle x^2 \rangle = \int_0^\infty a^2 \dot{n}(a) da \int_{-\infty}^{+\infty} g^2(t - t_0) dt. \quad (3.53)$$

Firstly, let's find the response of the electron to a δ -pulse excitation, setting the initial energy deviation to the loss due to the emission of the photon $\Delta E_0 = -\omega_2$ and assume weak damping:

$$g(t - t_0) = \Delta E = -\omega_2 e^{-\alpha_E t} \cos(\Omega_s(t - t_0)), \quad (3.54)$$

where ω_2 is the scattered photon energy, α_E is the damping rate and Ω_s is the synchrotron frequency.

Plugging it into Eq. 3.53 and evaluating the integral over the square of the response function by making two times integration by parts, one can obtain

3.3 Production schemes for the polarized positron sources

$$\int_{t_0}^{\infty} g^2(t-t_0)dt = \int_0^{\infty} g^2(t)dt = \int_0^{\infty} (e^{-\alpha_E t} \cos \Omega_s t)^2 dt = \frac{\alpha_E}{4(\Omega_s^2 + \alpha_E^2)} + \frac{1}{4\alpha_E}. \quad (3.55)$$

Usually the damping is relatively small, so $\alpha_E \ll \Omega_s$ and therefore one can neglect the first term in Eq. 3.55.

Now, one can define the damping rate. The inverse of the damping rate can be understood as the time it takes for the electron to radiate its total energy. In such a way,

$$\alpha_E = \frac{\langle P_\gamma \rangle}{E_e} = \frac{\langle E_\gamma \rangle \mathcal{F}}{E_e} = \frac{\langle E_\gamma \rangle \mathcal{L} \sigma_c}{E_e} = \frac{h \langle \nu \rangle \mathcal{L} \sigma_c}{E_e}, \quad (3.56)$$

where $\langle P_\gamma \rangle$ is the average rate of the electron energy loss, E_e is the electron energy, \mathcal{F} is the flux of the scattered photons, \mathcal{L} is the luminosity of the Compton collisions, σ_c is the total Compton scattering cross section and ν is the frequency of the emitted photon. It was used that the total flux of scattering photons $\mathcal{F} = \mathcal{L} \sigma_c$ i.e. the emitted rate can be evaluated as a product of the Compton cross section by the luminosity. Knowing the average frequency of the emitted photon being equal $\langle \nu \rangle = \frac{4}{3} \nu_0 \gamma^2$, where ν_0 is the frequency of the incident photon, one can readily obtain the damping rate:

$$\alpha_E = \frac{h \langle \nu \rangle \mathcal{L} \sigma_c}{E_e} = h \frac{4}{3} \nu_0 \gamma^2 \frac{\mathcal{L} \sigma_c}{E_e} = \frac{4 \omega_1 \mathcal{L} \sigma_c}{3 E_e} \gamma^2. \quad (3.57)$$

In order to get the variance of the electron energy distribution, what one might do is to plug the obtained result for the damping rate into Eq. 3.55 and then insert it into Eq. 3.53 knowing that

$$\int_0^{\infty} a^2 \dot{n}(a) da = \int_0^{\omega_2^{max}} \omega_2^2 \dot{n}(\omega_2) d\omega_2 = \int_0^{\omega_2^{max}} \omega_2^2 \mathcal{L} \frac{d\sigma_c}{d\omega_2} d\omega_2, \quad (3.58)$$

where the $\dot{n}(\omega_2)$ is the spectral distribution in scattered photon energy ω_2 .

In such a way, the variance of the electron beam energy distribution is

$$\sigma_E^2 = \int_0^{\omega_2^{max}} \omega_2^2 \dot{n}(\omega_2) d\omega_2 \int_0^{\infty} g^2(t) dt = \frac{3}{16} \frac{E_e}{\omega_1 \sigma_c \gamma^2} \int_0^{\omega_2^{max}} \omega_2^2 \frac{d\sigma_c}{d\omega_2} d\omega_2, \quad (3.59)$$

where

$$\sigma_{\omega_2}^2 = \int_0^{\omega_2^{max}} \omega_2^2 \frac{d\sigma_c}{d\omega_2} d\omega_2. \quad (3.60)$$

3. THEORETICAL INTRODUCTION FOR INNOVATIVE SCHEMES

At this point, one needs to calculate the total Compton scattering cross section σ_c and the variance of the scattered photon energy spectrum $\sigma_{\omega_2}^2$. It should be immediately pointed out that according to Eq. 3.59 this method based on the Campbell's theorem gives the possibility to calculate the electron beam energy spread in the case of the polarized Compton scattering just by knowing the appropriate scattered photon energy distribution $d\sigma_c/d\omega_2$.

To accomplish the calculations, let's take the unpolarized Compton scattering as an example. The initial expression for the differential Compton cross section is taken from [56]. The first step is to convert the differential scatter cross section per unit solid angle $d\sigma_c/d\Omega$ to the differential scatter cross section per unit scattered photon energy $d\sigma_c/d\omega_2$ by using the relation $d\Omega = \sin\theta d\theta d\phi = -d\cos\theta d\phi$. Eventually, after the integration over the azimuthal scattering angle ϕ and assuming the Compton scattering being unpolarized, the differential cross section reads:

$$\frac{d\sigma_c}{d\omega_2} = \frac{\pi r_0^2 \left(\frac{\omega_2^2 E_e^3}{\gamma^2} - 4\omega_1\omega_2 E_e^3 + 4E_e\gamma^2\omega_1^2 (E_e^2 + (E_e - \omega_2)^2) \right)}{8\gamma^4 E_e^3 \omega_1^3}. \quad (3.61)$$

To simplify the final expression a reasonable assumption in the computations is to assume that the $E_e - \omega_2 \approx E_e$ which implies a moderate electron beam energy. The final thing that one needs to do is integrate Eq. 3.60 over ω_2 and substitute the result into Eq. 3.59.

In such a way the electron beam energy spread obtained by Campbell's theorem can be written as:

$$\delta_E \equiv \frac{\sigma_E}{E_e} = \sqrt{\frac{21}{20} \frac{\omega_1 \gamma^2}{E_e}} \quad (3.62)$$

As in the previous case, let's assume the Compton ring working at the 1.3 GeV electron beam energy together with the 1 μm (1.17 eV) wavelength laser. Using Eq. 3.62 it corresponds to the 7.8% of the equilibrium energy spread comparing to 9% of that calculated by Eq. 3.50. It shows a reasonable agreement within the assumption made.

In this context, Campbell's theorem provides a comprehensive technique to compute the equilibrium electron beam energy spread in the Compton ring what is the one of the most critical issue of the positron source design.

3.3.3 ERL solution. Multiple Interaction Point Line.

As it was discussed before, the ERL production scheme has some advantages over the Compton ring. Nevertheless, the disadvantage of insufficient electron bunch charge still remains. In this case, one of the solution to overcome this problem of insufficient number of the polarized positrons per beam crossing is to design a Multiple Interaction Point Line (MIPL), that should allow an important increase of the emitted gamma ray flux. This requires a system of focusing triplets to focalise the electron beam on a laser pulse stored in the Fabry–Perot cavities. Fig. 3.14 shows the schematic view of such MIPL. From this moment, let’s consider the case where two lasers cross symmetrically in respect to the beam propagation axis. The parameters of the Compton IP used for this study are summarized in Table 3.1.

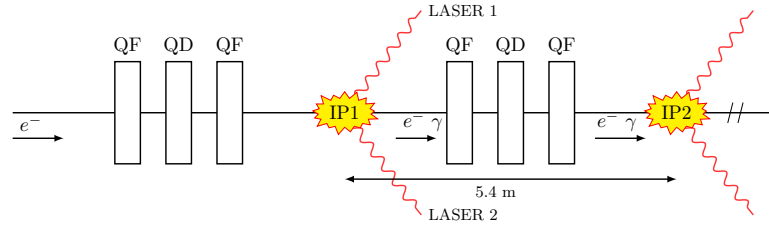


Figure 3.14: Multiple Interaction Point Line - Schematic view. QF and QD denotes focusing and defocusing quadrupoles respectively. A set of QF-QD-QF separated by the drifts forms a quadrupole triplet to focalise the electron beam at each IP. Two lasers cross symmetrically in respect to the beam propagation axis. The parameters of the MIPL are given in Table 3.1 and 3.2.

For given Twiss parameters at the first IP, the PBO Lab TRANSPORT Application Module [113] has been used to find the parameters of the quadrupole triplet in order to preserve the same Twiss parameters for the subsequent IP. The results obtained are listed in Table 3.2. In such a way, the MIPL can be modeled in first approximation by translating this structure (cell) a certain number of times. Fig. 3.15a shows the evolution of beta function (β_x, β_y) along the 5 IP MIPL.

However, the previous method does not take into account the effect of the Compton recoil at each IP. The Compton collisions introduce an additive variation of the average electron energy as well as an increase of the energy spread (see e.g. Fig. 3.17b).

Since the strength of the quadrupole force depends on the field gradient g and the

3. THEORETICAL INTRODUCTION FOR INNOVATIVE SCHEMES

Description	Value
Electron energy, E_e	2 GeV
Electron bunch charge, C_e	0.5 nC
Electron bunch length, τ_e	3 ps
Electron IP β_x/β_y	0.1 m/rad
RMS energy spread, δ_E	0.002
Electron emittance, $\gamma\epsilon_x/\gamma\epsilon_y$	10 $\mu\text{m rad}$
Electron IP beam size, σ_x/σ_y	16 μm
LASER photon energy, E_{ph}	1.17 eV
LASER beam waist, $\omega_L = 2\sigma_L$	30 μm
LASER pulse length, τ_L	5 ps
LASER pulse energy, E_L	0.6 J
Crossing angle, θ	2°

Table 3.1: The Compton IP parameters used for the MIPL simulation - Parameters defining the electron and laser beam at the Compton IP.

particle momentum p ($p = \beta E_{tot}$):

$$K_1 = \frac{eg}{p}, \quad (3.63)$$

where e is the electron charge, the electrons with different energy get different focusing (chromatic aberrations). This results in the degradation of the transverse electron beam size at the IPs and a reduction of the luminosity (see Eq. 3.45). Fig. 3.15 shows the evolution of the betatron function ($\beta_x^{Com}, \beta_y^{Com}$) along the 5 IPs MIPL together with the final phase space ellipse taking into account the average electron energy loss at each IP due to the Compton scattering.

In this framework, it appears efficient to adjust the magnetic field gradient of the quadrupoles according to the average energy change, to match the 5IP MIPL and have the same focalization for each IP.

The simulations of the Compton MIPL are done by means of the CAIN code [114] and show a good increase of the gamma ray flux (see Fig 3.17a).

CAIN is a Fortran Monte-Carlo code modeling interactions involving high energy electrons, positrons and photons. It was several times bench-marked for different Compton sources e.g. in [85, 115]. In our case CAIN is used to simulate the laser-Compton

3.3 Production schemes for the polarized positron sources

Parameter	Symbol	Value	Unit
QF quadrupole coefficient	K_1	5.890693	m^{-2}
QD quadrupole coefficient	K_1	-4.745558	m^{-2}
QF effective length	l_{eff}	0.2	m
QD effective length	l_{eff}	0.3	m
Drift between QF-QD	$d_{\text{QF-QD}}$	0.3	m
Drift to the IP	$d_{\text{QF-IP}}$	2	m
Length of one IP	L_{cell}	5.4	m

Table 3.2: Parameters of one cell of the Multiple Interaction Point Line - One cell is defined as one comprised from the drift of 2 m+ QF + drift of 0.3 m + QD + drift of 0.3 m + QF + drift of 2 m.

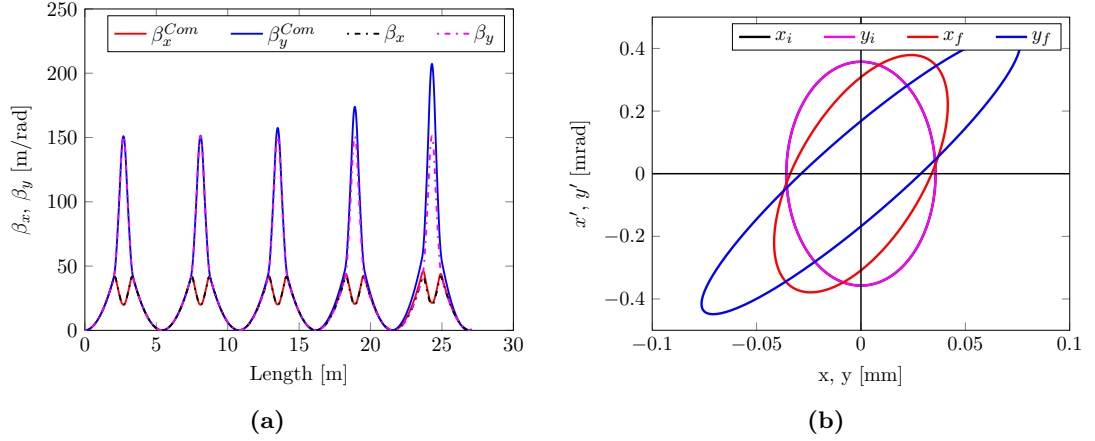


Figure 3.15: Evolution of the betatron function along the MIPL consisting of 5 IPs. - Fig. 3.15a illustrates the betatron function increase due to the Compton collisions at each IP whereas Fig. 3.15b shows the initial and final electron phase space ellipse for the 5 IP MIPL.

3. THEORETICAL INTRODUCTION FOR INNOVATIVE SCHEMES

scattering process and to obtain the spatial and energy distribution of the gamma rays produced.

For our simulations, an essential difference between the Monte-Carlo code and the physical reality is that the former generally uses less particles than the real physical problem. This often causes significant statistical errors. The most important aspect is making sure that the number of macro-particles in the simulation is large enough to minimize the statistical error. Therefore, Fig. 3.16 shows the “statistical card” of the simulation made by CAIN. Eventually, it was decided to use a sample composed by 500000 macro-particles which introduces a statistical error of less than 1%.

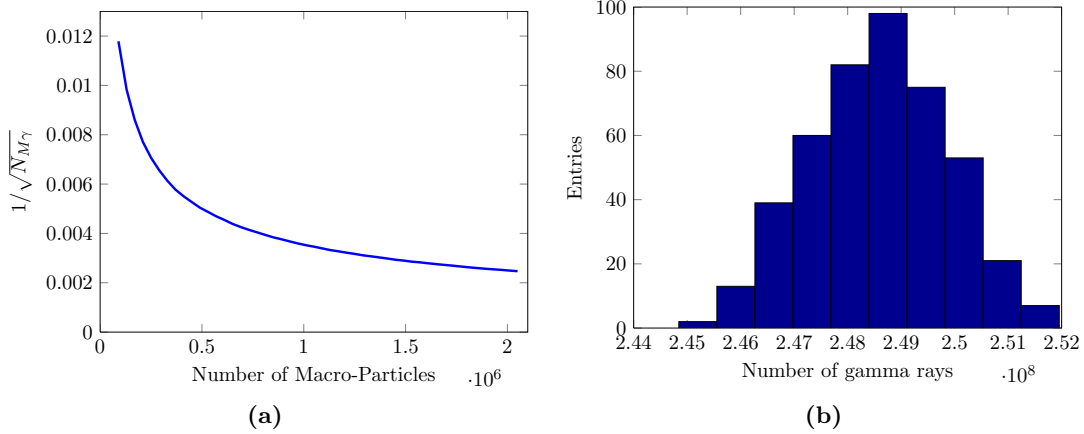


Figure 3.16: “Statistical card” of the CAIN simulation - The results presented are simulated for one IP with two crossed laser configuration. The parameters used for the simulation are summarized in Table 3.1. Fig. 3.16a shows the evolution of the statistical error versus the initial number of macro-particles used in CAIN simulation. Fig. 3.16b illustrates the number of the scattered gamma rays distribution given by several successive runs (500000 macro-particles each). So, the result can be given as $N_\gamma = (2.49 \pm 0.01) \times 10^8$.

From Fig. 3.17a one can see also that after a few IPs, chromatism of the electron beam caused by the electron energy spectrum degradation due to the Compton collisions start to reduce the gain given by the MIPL and the increase of the gamma ray flux is not linear. The effect is magnified by the losses due to the collimation system of the gamma rays installed to reach the degree of polarization required. It is still efficient to consider five IPs where we assumed two crossed laser configuration. In this case a factor four of the gain in the total gamma ray flux is obtained. The effect of the electron energy spectrum degradation can be observed in Fig. 3.17b. It is interesting to

3.3 Production schemes for the polarized positron sources

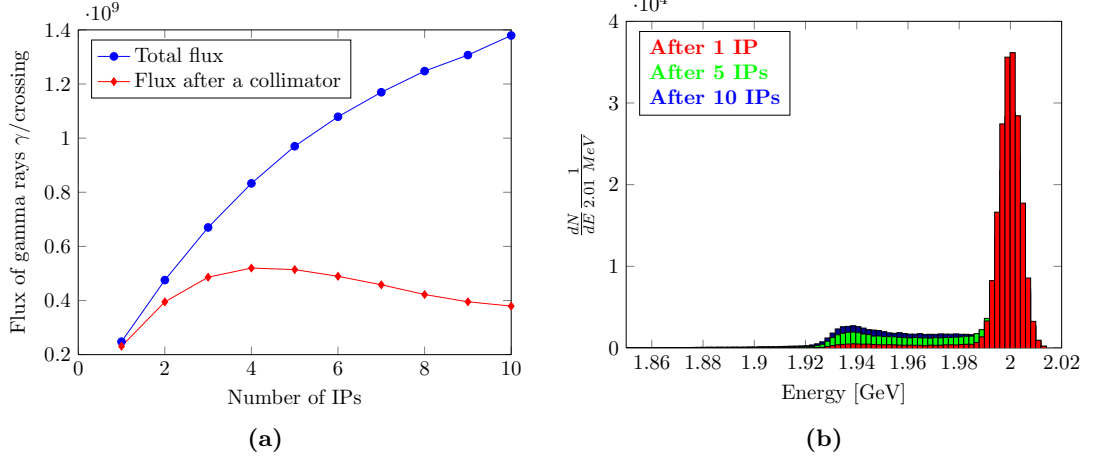


Figure 3.17: Gamma ray flux and the electron energy distribution for the Multiple Interaction Point Line - It is clear from Fig. 3.17a that after a certain point chromatism of the electron beam and losses due to the natural system diaphragmisation of the gamma rays starts to reduce the gain. So after a few IPs the electron energy spectrum degradation shown on Fig. 3.17b due to the Compton collisions reduces the efficiency of the MIPL.

notice, that with an increasing number of Compton collisions (number of IPs), the low energy tail given by the recoil of the scattered electrons takes the form of the scattered gamma ray energy spectrum.

As it was discussed before, angular (energy) selection of the scattered gamma rays is needed to reach the requested degree of polarization. Fig. 3.18a shows the collimator efficiency and polarization as a function of the collimator diameter for the gamma rays travelled five meters downstream the last IP.

The collimator acts as a selector of the gamma ray polarization. This is also illustrated in Fig. 3.19 where the Stokes parameters are drawn for the gamma rays produced by 100% circularly polarized laser photons obliquely colliding with the unpolarized electron beam. It is worth to notice that the angular selection affects strongly the circular polarization represented by the ξ_{3f} Stokes parameter (see Fig. 3.19a) while the linear polarization (see Fig. 3.19b) remains statistically unchanged.

Increase in the polarization accompanies the reduction of the gamma rays available for the positron production. Eventually, the trade-off between the polarization and collimator efficiency should be made to define the collimator size. In our case the

3. THEORETICAL INTRODUCTION FOR INNOVATIVE SCHEMES

diameter of 12 mm has been chosen to ensure a sufficient degree of polarization and number of gamma rays.

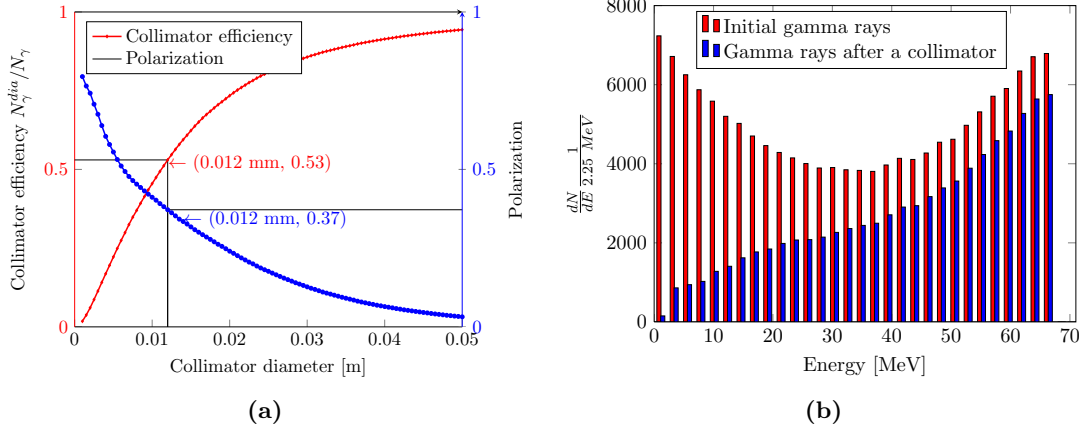


Figure 3.18: The collimator efficiency and polarization as a function of the collimator diameter. The computed energy spectrum of the scattered gamma rays. - The collimator is placed five meters downstream the last IP. The collimator diameter of 12 mm has been chosen to provide $\sim 40\%$ degree of circular polarization together with a collimation efficiency of 0.53. Fig. 3.18b shows the energy distribution of the gamma rays before and after the collimator.

The computed energy spectrum of the gamma rays produced after the 5 IPs is shown on Fig. 3.18b together with the spectrum selected by the collimator to be used for the polarized positron generation. The collimated gamma ray beam gets rid of the low energy part having the “worse” polarization. The gamma ray mean energy after the collimator is 45 MeV while the gamma ray polarization equals 37.9%.

The main results of the gamma ray production simulation are presented in Table 3.3.

3.3 Production schemes for the polarized positron sources

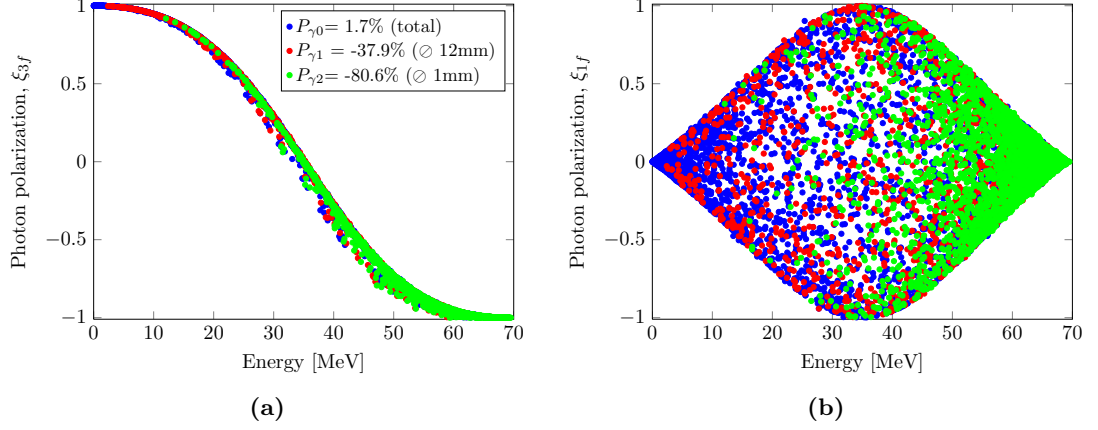


Figure 3.19: Polarization distribution of the scattered gamma rays - Fig. 3.19a shows the circular polarization distribution while Fig. 3.19b presents one of the cases of the linear polarization distribution of the gamma rays. Blue dots denote all the scattered gamma rays, red and green dots are tagg the gamma rays selected by a collimator of 12 mm and 1 mm diameter respectively.

Description	Value
Gamma ray peak energy	69.7 MeV
Mean gamma ray energy	34.2 MeV
Diaphragm diameter after 5m of drift , \varnothing	0.012 m
Mean gamma ray energy after diaphragm	45.2 MeV
Mean gamma ray polarization	37.9 %
Diaphragm efficiency($N_{\gamma}^{dia}/N_{\gamma}^{tot}$)	0.53
Gamma ray production efficiency ($N_{\gamma}^{tot}/N_{e^{-}}$)	0.079 (0.31)
Gamma ray accepted efficiency ($N_{\gamma}^{dia}/N_{e^{-}}$)	0.042 (0.16)

Table 3.3: Parameters of the produced gamma ray distribution - In the case of the gamma ray production and accepted efficiencies the values in parentheses correspond to the 5 IP MIPL .

3. THEORETICAL INTRODUCTION FOR INNOVATIVE SCHEMES

4

Positron source performance

4.1 Why positron sources are critical components of the future linear colliders?

Positron sources are critical components of the future Linear Collider (LC) projects. This is essentially due to the very high beam intensity required to achieve a high luminosity.

Positrons are generated in a target by $e^+ - e^-$ pair conversion of high energy gamma rays. Nevertheless, the target thermo-mechanical stresses given by the Peak Energy Deposition Density (PEDD) and the average heating impose a physical limit on the number of positrons produced in a bunch and in a train. Moreover, the positron production in a target implies after pair creation, bremsstrahlung and multiple scattering a wide angular and energy distribution of the positron bunch. As the result, the positron source 6D emittance at the production is orders of magnitude bigger with respect to the one from an electron source. It has also to be considered that being limited in intensity, it is impossible to perform a phase space selection by a diaphragm to reduce the emittance at the source.

In addition, the positron emittance at the production and the accelerating capture chain define the positron emittance at the injection into the Damping/pre-Damping Ring (DR) and so the main DR parameters. The request for a polarized positron beam results in an additional degree of complexity, which makes the polarized positron sources rather large and expensive facilities.

4. POSITRON SOURCE PERFORMANCE

These aspects have a strong impact on the injector complex design and performance parameters, such as the repetition frequency, injector current, DR acceptance, DR cooling time, etc..

Summarizing, the most important features and difficulties of the positron sources are the following:

- To increase the luminosity, the future LC requires high average and peak flux. This strongly reduces the possibility to provide a design based on the so-called “conventional source”, where a relativistic electron beam impinges on an amorphous target and the high energy gamma rays are produced by bremsstrahlung and converted in $e^+ - e^-$ pairs in the target. The target heating and thermo-mechanical stresses due to the particle energy losses are extremely high. Therefore, new schemes of positron production where only gamma rays are impinging on the target have been proposed and studied.
- After the target, positrons are highly scattered in space and have a broad energy distribution. Thus due to the large 6D phase space at the production, a low positron capture efficiency is expected.
- The positron yield can be improved by employing a thicker target-converter. However, this will increase the amount of multiple scattering within the target and energy deposited inducing the higher heat load in the target. The optimum target thickness should be found.
- The thermal constraints of the target-converter define the positron bunch charge and possible current of the positron bunch train.
- The positron emittance at the production and the accelerating capture chain determine the positron emittance at the DR injection. Consequently, this fixes the number of the damping times needed as well as the dynamic and physical apertures for the positron beam in the DR to achieve the emittance required at the final IP. This establishes the repetition frequency of the accelerator.
- The future LC requires polarized beams. It exists a well motivated physics case to have not only the electron beam, but also the positron beam polarized [5, 12]. This represents additional technological challenges for the positron sources design.

All these issues show that the polarized positron source is a challenging facility and that the final luminosity of the future LC is constrained by the positron source design setting the main accelerator parameters such as the repetition frequency, the bunch and the train current, etc..

4.2 Positron production

4.2.1 Positron target effects and limits

The gamma rays impinging on a target-converter initiate an electromagnetic shower. The gamma rays interact with matter mainly by means of three processes: photoelectric effect, Compton scattering and $e^+ - e^-$ pair creation. The other processes such as the photonuclear interactions, Rayleigh scattering occur also but with a lower probability (see Fig. 4.1). At low gamma ray energies the photoelectric effect dominates whereas at medium energies the gamma rays interact mainly by Compton scattering. At high energies the pair production is the most probable outcome.

The total cross section of each of the process is a function of the gamma ray energy and the atomic number Z of the target material ($\sigma_{p.e.} \sim Z^{3-5}$, $\sigma_{Compton} \sim Z$, $\sigma_{pair} \sim Z^2$). Given the dependence on the atomic number, the materials with high Z like Tungsten ($Z=74$) are preferable for the positron converters.

In such a way, the gamma rays with energies greater than a few MeV undergo pair production. The created $e^+ - e^-$ pairs generate bremsstrahlung radiation which in turn produces more particles with lower energy (electromagnetic cascade). Furthermore, the charged particles traversing the target undergo multiple scattering. They lose energy mainly by ionization at low energies and by the radiation losses (bremsstrahlung) at higher energies (see Fig. 4.2).

The average energy deposited in the target-converter by the electromagnetic shower provokes a temperature rise. The impact of the temperature on the positron yield has been studied in [116] for a crystal target. The authors show that according to simulations made for a 4 mm thick crystal tungsten target, the positron yield is decreasing by an amount of 10-20% when the temperature grows from the ambient to 600°C. The positron yield of the amorphous converter remains unchanged with such temperature increase [116]. The melting point of the target-converter limits the possible temperature increase.

4. POSITRON SOURCE PERFORMANCE

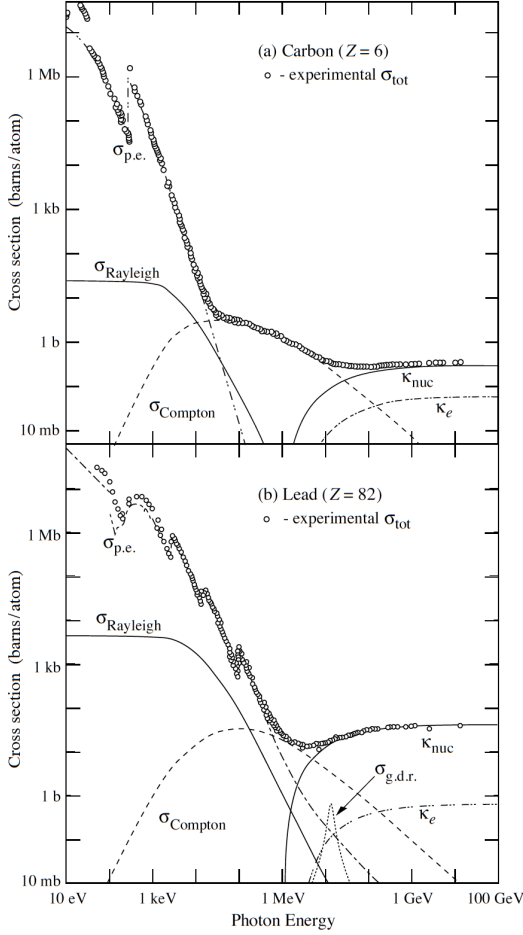


Figure 4.1: Gamma ray total cross sections as a function of energy in carbon and lead - Figure shows the contributions of different processes such as photoelectric effect $\sigma_{p.e.}$, Rayleigh scattering $\sigma_{Rayleigh}$, Compton scattering $\sigma_{Compton}$, pair production in nuclear or electron field κ_{nuc}/κ_e , photonuclear interactions $\sigma_{g.d.r}$ [117].

On the other side, the local and almost instantaneous energy deposition in the target can be very critical for the target lifetime. The heat load in the target is inhomogeneous due to the lateral development of the electromagnetic shower. This results in thermal gradients causing mechanical stresses (shock waves). If during the periodic heat load given by the pulsed irradiation these stresses exceed the elastic limit, target failure may occur. At present, there is no theoretical description to predict this phenomenon. The only available experimental data come from the experiments at SLAC [118]. The targets made of the different materials have been irradiated by the 20 - 33 GeV electron beams with several beam spot sizes at the target. Some targets have not survived to the irradiation. A threshold in the incident beam energy density per area for the cracked targets have been found to be $\sim 1.95 \times 10^{12}$ GeV/mm² [119]. After the SLC production target breakdown, a limit on the deposited energy per unit volume has been determined. The studies

undertaken at Los Alamos National Lab (LANL) [120], Stanford Linear Accelerator Center Laboratory (SLAC) and Lawrence Livermore National Laboratory (LLNL) [121] concerning the SLC tungsten positron target being in operation for ~ 1000 days showed that a Peak Energy Deposition Density (PEDD) in the SLC target of 35 J/g might not

be exceeded. This is now considered as a maximum tolerated value of the PEDD in Tungsten target for the positron source design.

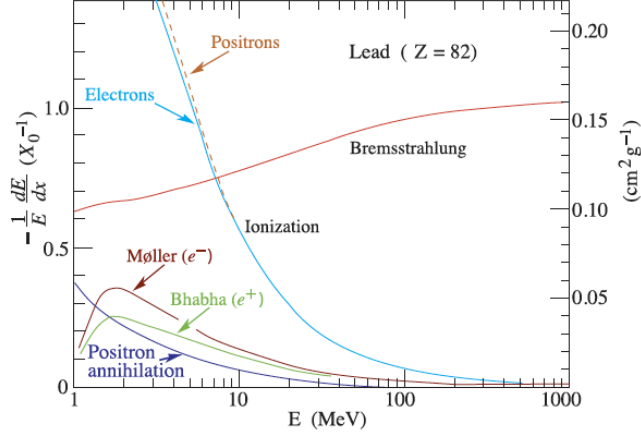


Figure 4.2: Fractional energy loss per radiation length in lead as a function of electron or positron energy - Figure shows the different contributions to the electron or positron energy loss [117].

4.2.2 Positron production simulations. The CLIC case.

To work on a practical example, the positron production and capture efficiency have been evaluated for the CLIC capture section. In this case, the simulation of the positron production is performed using a Geant4 code developed at LAL where the gamma rays-to-positrons polarization transfer and the subsequent depolarization in the target-converter are taken into account. A simplified scheme of positron production stage is shown in Fig. 4.3. The gamma ray distribution resulting from the 5 IP MIPL (see Section 3.3.3 Fig. 3.18b) is used to simulate the positrons. In order to calculate the optimum thickness of the target, the variation of the number of positrons emerging from the target with the target thickness has been investigated. A sample composed by ~ 165000 macro-particles has been used to perform the optimization studies. After the optimization studies regarding the positron yield (ratio of the number of positrons produced and the number of the incident gamma rays, N_{e^+}/N_{γ}^{dia}) and polarization (see Fig. 4.4), a 4 mm thick target made of Tungsten¹ has been used to simulate the production of the polarized positrons. This choice provides the maximum positron

¹In the real experiments the Tungsten-Rhenium ($W_{75}Re_{25}$) alloy targets are usually used.

4. POSITRON SOURCE PERFORMANCE

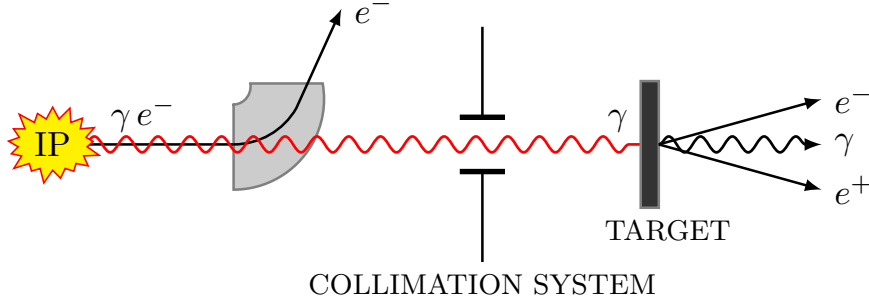


Figure 4.3: A fundamental scheme of the positron production - The gamma rays produced by Compton scattering are collimated and sent to the target. The electron beam is swept off before the target-converter to decrease the energy deposited inside the target causing various thermal effects.

yield (see Fig. 4.4a) while keeping the positron polarization at an acceptable level of 35 % (see Fig. 4.4b).

The energy deposited by the gamma ray generated shower in the target is shown on Fig. 4.5. For this, a mesh of $50 \times 50 \times 10$ has been created and the energy deposited is calculated within each target cell ($\Delta x = 0.5$ mm, $\Delta y = 0.5$ mm, $\Delta z = 0.4$ mm). In order to estimate the PEDD, the maximum energy deposited in the meshed volume has been found. It is about ~ 1.3 keV per initial electron what corresponds to the ~ 0.013 GeV/cm³/e⁻. In the case of the CLIC polarized positron source the PEDD should not be an issue for the target-converter design. The total energy deposited in the target is 0.89 MeV/e⁻.

The resulting positron energy spectrum is shown on Fig. 4.6a. Fig. 4.6b illustrates the energy dependence of the impinging gamma ray polarization together with that of the positrons produced.

The parameters and the results of the positron production simulation are listed in Table 4.1. The output of this simulation have been used as an input data for the Accelerating Capture Section (ACS) simulation. ACS consists of a matching device to capture the produced positrons and a pre-injector linac for primary longitudinal capture and acceleration. Afterwards, the positron beam is further accelerated and injected into a pre-DR.

4.2 Positron production

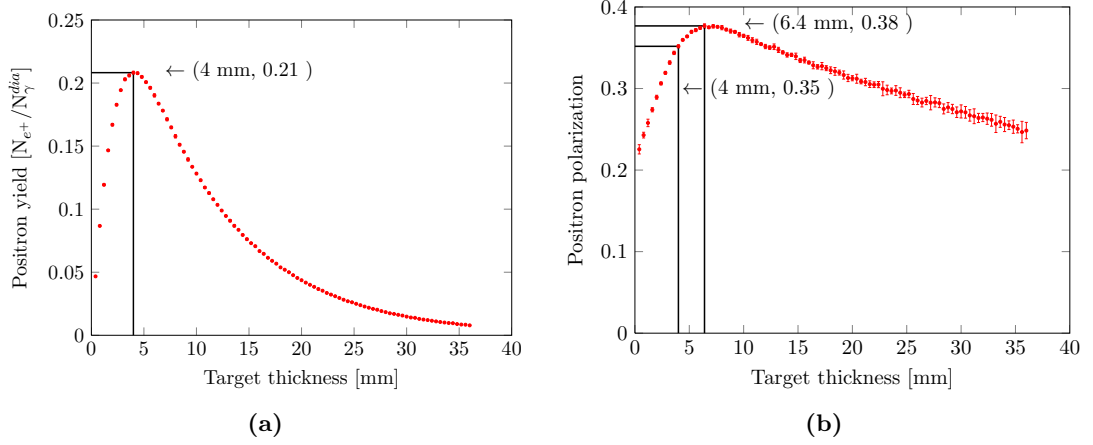


Figure 4.4: Optimization of the target-converter thickness - Fig. 4.4a shows a transition curve of the positrons generated during the electromagnetic shower development inside the Tungsten target. The shower is initiated by the gamma rays produced by Compton scattering. Fig. 4.4b shows the variation of the polarization with the target thickness. A 4 mm thick Tungsten target has been chosen.

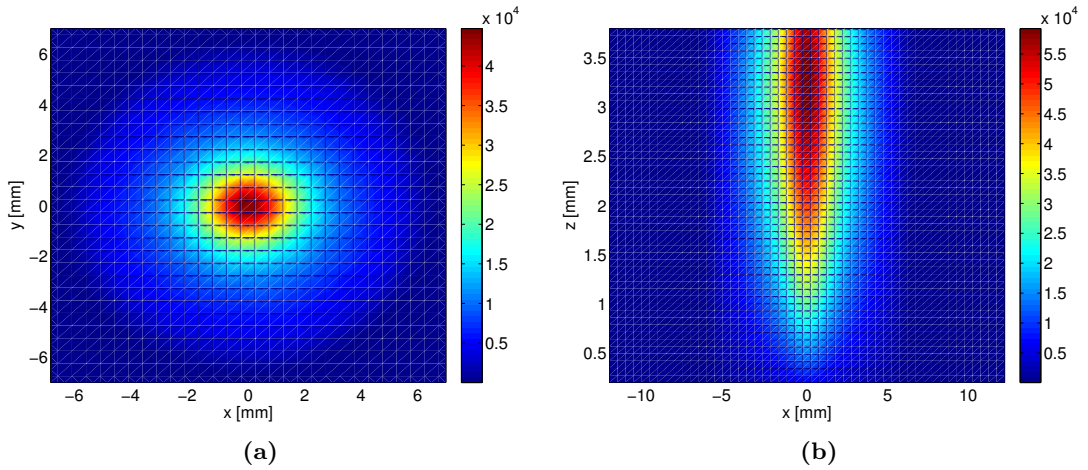


Figure 4.5: Energy deposition pattern in the target-converter - Fig. 4.5a shows the transverse x-y projection while Fig. 4.5b shows the x-z plane view. The gamma rays impinge along z- direction. As one can see, the energy deposition density is maximum at the exit of the target. The colorbar shows the total energy deposition in MeV.

4. POSITRON SOURCE PERFORMANCE

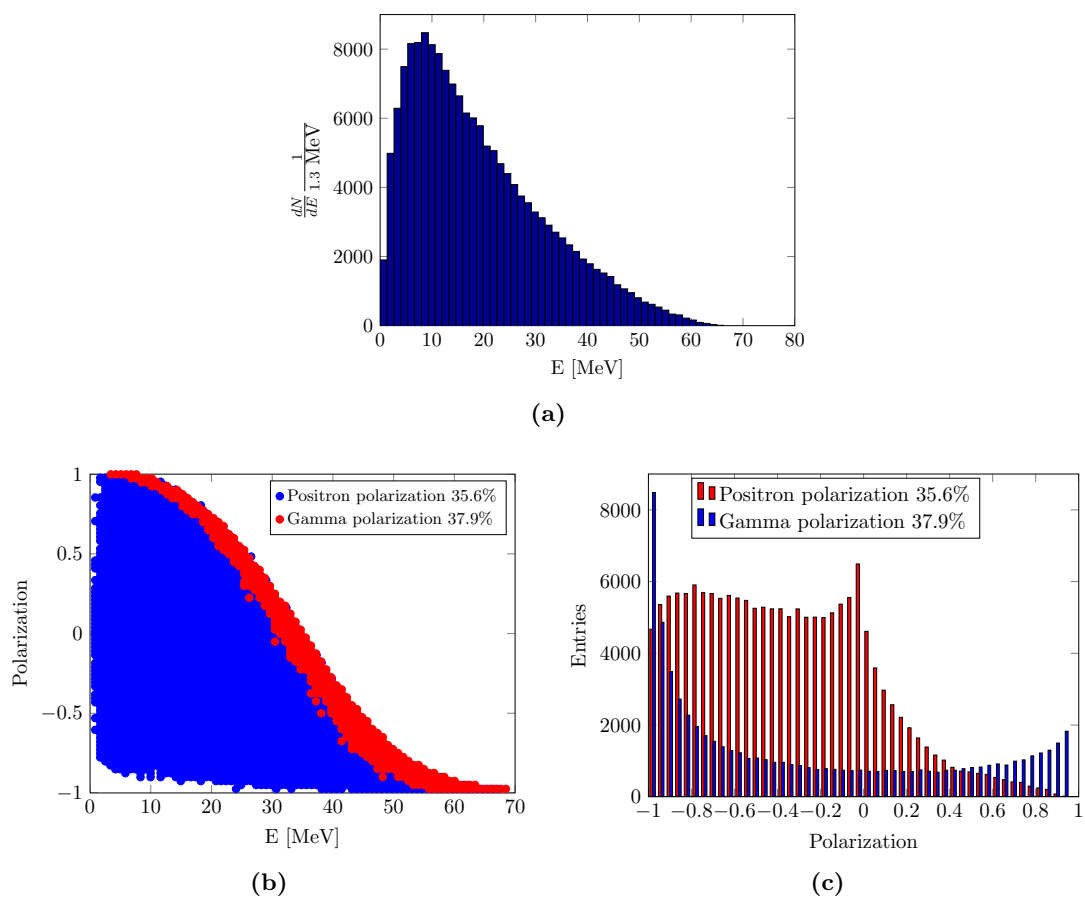


Figure 4.6: Distribution of the positrons produced - Fig. 4.6a shows the energy spectrum of the positrons at the exit of the target while Fig. 4.6b and Fig. 4.6c show the energy-polarization dependence and the polarization distribution of the gamma rays and positrons produced.

Description	Value
Gamma ray mean energy,	45.2 MeV
Target material	Tungsten
Tungsten radiation length, X_0	$8\text{g}/\text{cm}^2$ (0.35 cm)
Target shape	Rectangular Prism
Target thickness	4 mm
Target size	$2.5\text{ cm} \times 2.5\text{ cm}$
Gamma ray production efficiency (N_γ^{tot}/N_{e^-})	0.31
Positrons production yield (N_{e^+}/N_γ^{dia})	0.2
Compton source production efficiency (N_{e^+}/N_{e^-})	0.03
Mean positron energy at the production	18.9 MeV
Mean positron polarization at the production	35.6%
Total energy deposition in the target	$0.89\text{ MeV}/e^-$
PEDD in the target	$0.013\text{ GeV}/\text{cm}^3/e^-$

Table 4.1: The parameters and the results of the positron production simulation - The initial gamma rays have been produced by the Compton scattering of 1.17 eV laser photons by the 2 GeV electrons at the incident angle of 2 degrees. The 5 IP MIPL line has been employed. A sample composed by ~ 825000 macro-particles which introduces the statistical error less than 1% has been used.

4. POSITRON SOURCE PERFORMANCE

4.3 Capture system and primary acceleration

The ACS section design is based on an Adiabatic Matching Device (AMD) and 2 GHz pre-injector linac made of the 17 MV/m constant gradient Travelling Wave (TW) structures to accelerate the positrons up to the 200 MeV. A simplified scheme of the ACS is shown on Fig. 4.7. The simulation of the ACS is performed using a tracking code ASTRA [122].

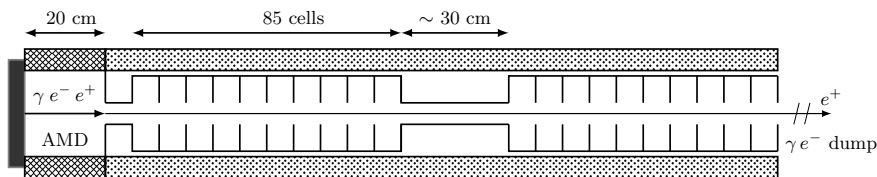


Figure 4.7: A fundamental scheme of the positron capture and primary acceleration - A capture section based on the AMD followed by a pre-injector linac is used to capture and accelerate the positron beam up to the ~ 200 MeV.

The AMD [123] is made of the tapered solenoid field and used to match the positron beam after the production (with large transverse divergence) to the acceptance of the pre-injector linac. The AMD is characterized by a strong peak field adiabatically decreasing to the nominal value of the solenoid field that surrounds the accelerating sections. The longitudinal field profile of the AMD can be observed on Fig. 4.8a. The main role of the AMD is to reduce the large angular divergence by increasing the beam radius. In this way the positron beam occupies all the geometrical acceptance of the accelerating structures. The transformation of the positron transverse phase space by the AMD is shown on Fig. 4.9. These systems have been successfully used at the SLAC [124] and the LAL in Orsay [125].

The AMD used in the simulation is 20 cm long with a longitudinal magnetic field starting at 6 T and adiabatically decreasing down to 0.5 T. The aperture radius of the AMD is 20 mm. It was shown in [127] that for a similar positron energy spectrum, a shorter AMD (20 cm compared to 50 cm) helps to gather more particles and minimize the bunch lengthening effect. Another capture system that can be used is a Quarter Wave Transformer (QWT) [123] where the magnetic field decreases rapidly without an adiabatic behaviour. The advantage of using the AMD rather than the QWT as a matching device, is that it allows to increasing the accepted positron yield by capturing

4.3 Capture system and primary acceleration

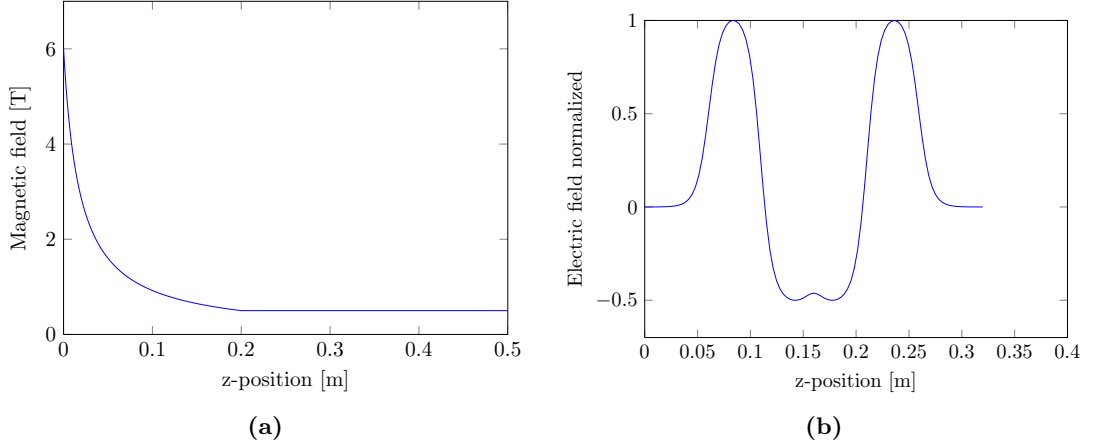


Figure 4.8: Magnetic and electric field profiles in the ACS - Fig. 4.8a shows a solenoid field of the AMD and pre-injector linac and Fig. 4.8b shows a longitudinal electric field of the TW 4-cell cavity together with drift fields. The latter was calculated with Superfish code [126] and used as input field for ASTRA.

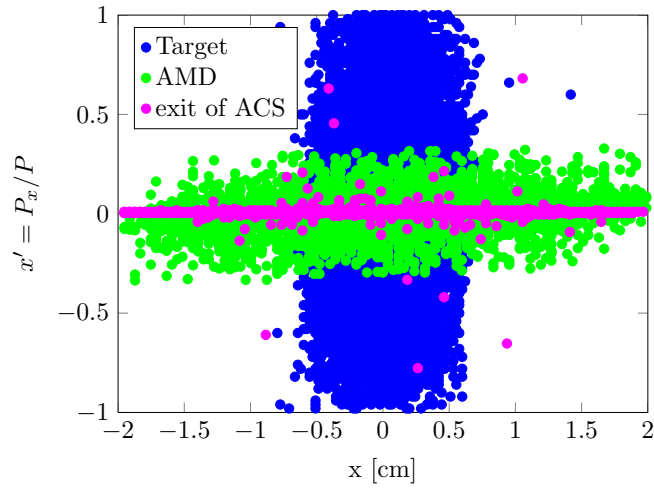


Figure 4.9: Positron beam emittance taken at the exit of the target, at the exit of the AMD and at the end of the accelerating capture section (ACS) - Figure shows the rotation of the positron transverse phase space transforming a small size high divergent positron beam to a beam having bigger size but lower transverse divergence. A reduced angular divergence is further compressed by adiabatic damping in the accelerating cavities of the pre-injector linac.

4. POSITRON SOURCE PERFORMANCE

the positrons within a wide energy band. Nevertheless, the drawback of the AMD is a lengthening of the bunch, which is afterwards responsible for the increase of the energy spread in the pre-injector linac. The parameters used for the simulations of the AMD are listed in Table 4.2.

At the end of the AMD six 2 GHz TW structures of the pre-injector linac are simulated. Each such RF structure is made of 84 cells and 2 couplers with the total length of 4.36 m. The iris radius of the RF cavities is 20 mm. A drift between the structures is set to one λ_{RF} that is about 15 cm.

To simulate one TW structure in ASTRA, a 3-cell cavity geometry is repeated 28 times with addition of the input /output coupler cell and the drift at each end of the structure¹. The longitudinal electric field of the basic structure to be repeated is shown on Fig. 4.8b. It includes the 3-cell cavity field together with couplers and drift fields.

The whole pre-injector linac is encapsulated inside a solenoid with the axial magnetic field equals to 0.5 T. It is employed to focus the positrons and to avoid the positron losses caused by the high divergence of the positron beam at the beginning of the ACS. The parameters used for the simulations of the ACS are summarized in Table 4.2.

The simulations show that the main positron losses are occurring after the AMD and the first TW structure. The main results obtained are presented in Table 4.3. To improve the positron source efficiency, a full optimization of the ACS has to be done. One of the proposed techniques implies the tuning of the RF phase of the first TW structure to decelerate the positrons in the first structure and further accelerate them in the following ones. Such technique [128] allows to capture more positrons and improve the positron bunch characteristics like the energy spread/bunch length what facilitates the stacking of the positrons bunches into the DR.

To define the Compton Positron Source (CPS) efficiency, an energy-longitudinal position window with (± 10 MeV, ± 10 mm) around the highest density of positrons is set at the end of the ACS. The longitudinal distributions of the positrons selected by this window is shown on Fig. 4.10. According to Table 4.3, the CPS efficiency normalized by the electron bunch charge and the energy of the laser pulse in the 5 IPs with

¹One TW structure is composed of the 85 cells surrounded by the drifts: $L_{TWS} = L_{DRIFT} + L_{IN} + 84 \times L_{CELL} + L_{OUT} + L_{DRIFT}$, where $L_{IN} = L_{OUT} = 0.5 \times L_{CELL}$, L_{CELL} is the length of one cavity cell being 0.0499 m, $L_{DRIFT} = 0.06$ m. In such a way, $L_{TWS} = 2L_{DRIFT} + 85 \times L_{CELL} = 4.36$ m.

4.3 Capture system and primary acceleration

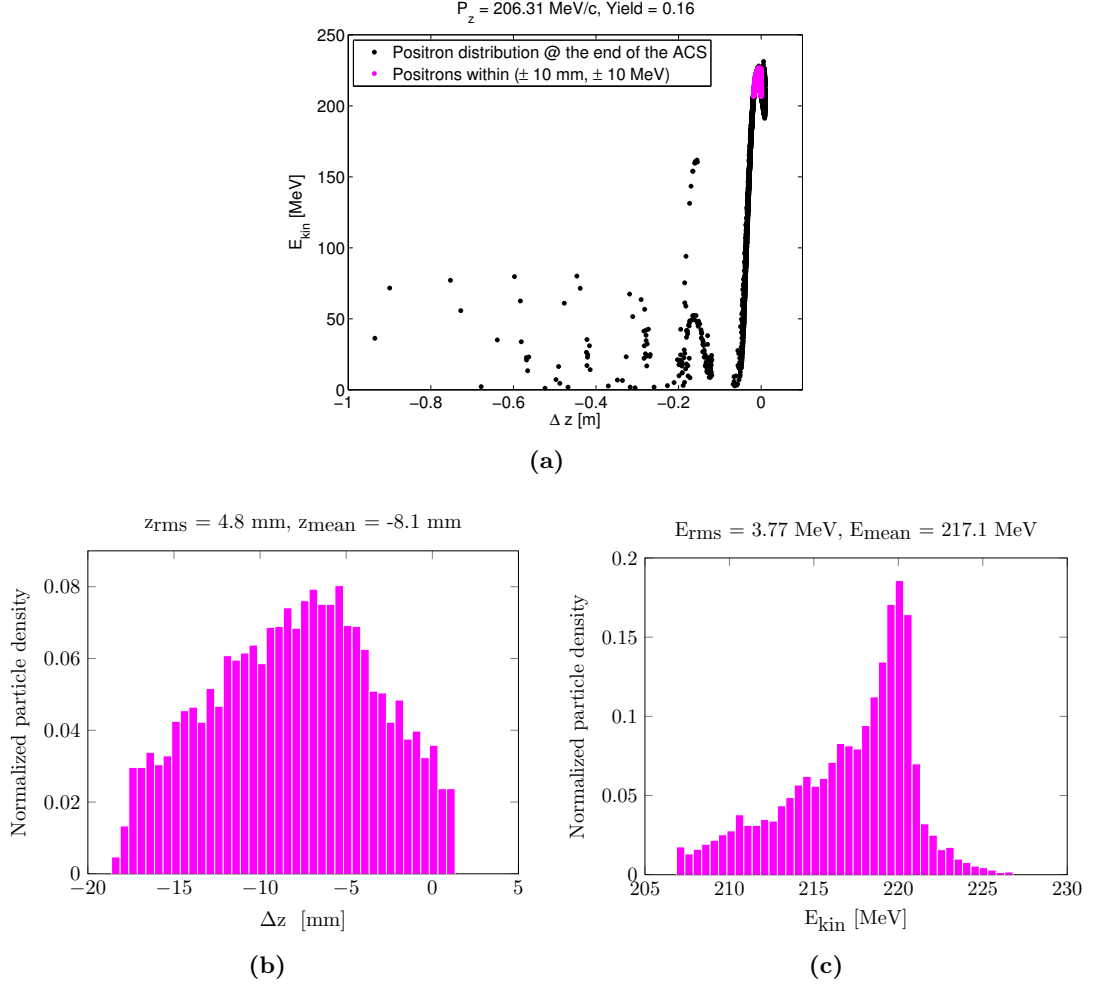


Figure 4.10: Longitudinal distributions of the positrons at the end of the pre-injector linac inside the (± 10 MeV, ± 10 mm) window - Fig. 4.10a shows the longitudinal distribution of the positrons at the exit of the ACS. The positrons which are within the specified window are tagged in magenta. Fig. 4.10b and Fig. 4.10c show their longitudinal and energy distributions respectively.

4. POSITRON SOURCE PERFORMANCE

Description	Value
Length of the ACS	~ 27 m
AMD initial field	6 T
Aperture radius	20 mm
ACS magnetic field	0.5 T
ACS type	TW
RF frequency	2.0 GHz
Iris radius	20 mm
Accelerating gradient	17 MV/m
Length of one TW structure	4.36 m
Number of cells in one TW structure	85
Phase advance per cell	$2 \pi/3$
Final energy	~ 200 MeV

Table 4.2: The parameters of the ACS used for the positron capture and primary acceleration simulation.

Description	Value
AMD capture efficiency ($N_{e^+}^{amd}/N_{e^+}^{targ}$)	0.43
Compton source accepted efficiency ($N_{e^+}^{amd}/N_{e^-}$)	0.014
ACS efficiency ($N_{e^+}^{\sim 200 MeV}/N_{e^+}^{targ}$)	0.24
Compton source efficiency ($N_{e^+}^{\sim 200 MeV}/N_{e^-}$)	0.0077
ACS efficiency ($N_{e^+}^{\pm 10 MeV \pm 10 mm}/N_{e^+}^{targ}$)	0.16
Compton source efficiency ($N_{e^+}^{\pm 10 MeV \pm 10 mm}/N_{e^-}$)	0.0051
Positron bunch length @ the ACS exit (σ_z)	~ 5 mm
Positron bunch energy spread @ the ACS exit ($\delta E/E$)	$\sim 2\%$

Table 4.3: Positron beam parameters at the exit of the AMD and the pre-injector linac - The initial gamma rays have been produced by the Compton scattering of 1.17 eV laser photons by the 2 GeV electrons at the incident angle of 2 degrees. The 5 IP MIPL line has been employed. A sample composed by ~ 166000 macro-particles which introduces the statistical error less than 1% has been used.

two crossed lasers scheme is estimated to be $1.71 \times 10^{-2}/(\text{nC} \cdot \text{J})$ or $5.32 \times 10^7 e^+ / (\text{nC} \cdot \text{J})$. A low positron charge produced per bunch can be compensated by multiple stacking in the same pre-DR RF bucket. In the case of the CLIC requirements, imposing $7.7 \times 10^9 e^+ / \text{bunch}$ at the entrance of the pre-DR [12], it is equivalent to ~ 140 injections/ $(\text{nC} \cdot \text{J})$.

4.3 Capture system and primary acceleration

For example, assuming a reasonable stacking efficiency of 10 injections per DR RF bucket, it is necessary to provide the electron bunches and laser pulses with $(nC \cdot J) \approx 14$ to the Compton IP which is not achieved with the current technologies. So, in this configuration a large number of stackings is needed.

The main results of the gamma ray and positron production, the positron capture and acceleration are summarized on Fig. 4.11.

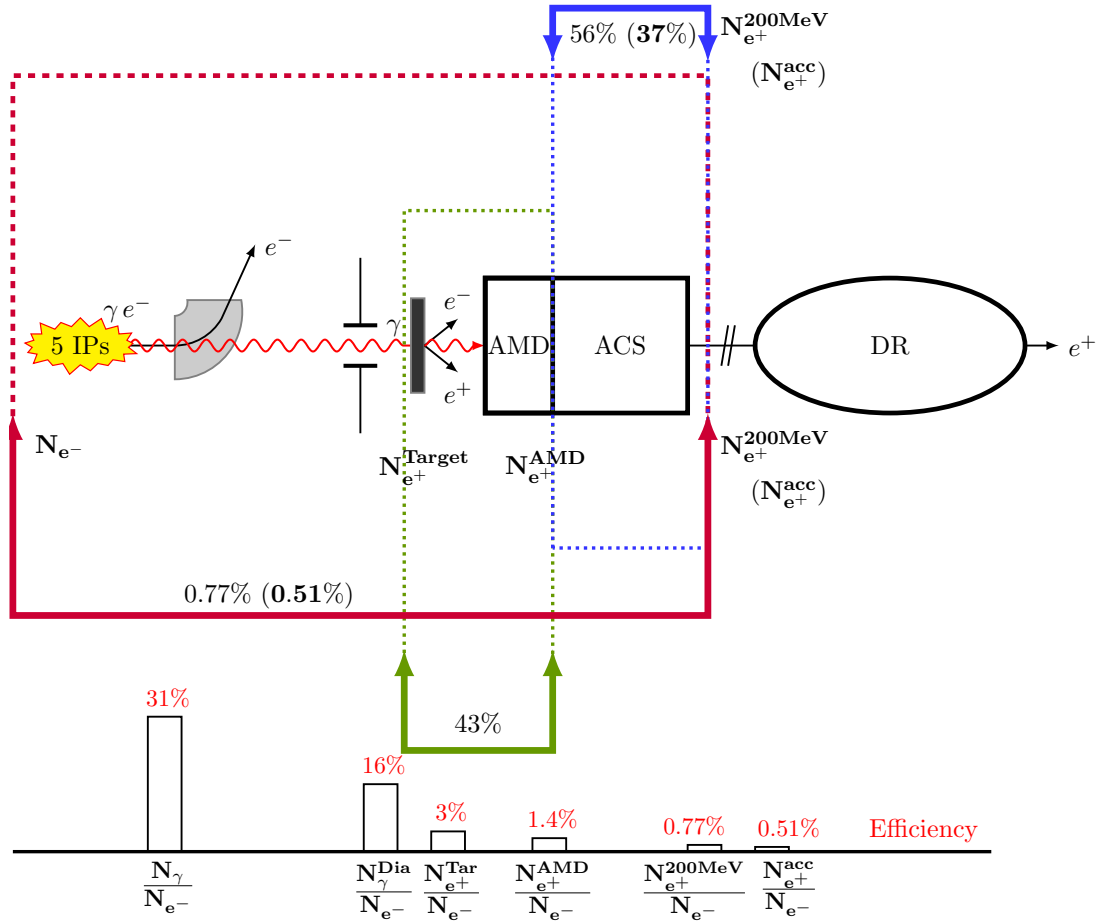


Figure 4.11: Layout of the Compton based polarized positron source - Figure shows the main elements and their efficiencies. A schematic diagram on the bottom illustrates the Compton source efficiency defined as the number of gamma rays/positrons taken at different stages divided by the number of electrons used.

4. POSITRON SOURCE PERFORMANCE

4.4 Impact of the results on the Compton based polarized positron source

The final design of the positron source for the future LC is under an evaluation stage. At present, the design for the baseline positron source of the ILC relies on the helical undulator to produce the high energy gamma rays which, then, are sent to the production target. The original layout of the positron source will allow to have a polarization of $\sim 30\%$ with the future upgrade up to $\sim 60\%$ [129]. However for the CLIC, the polarized positron source is not in the baseline configuration but an option for future upgrade [12]. The CLIC unpolarized positron source is a hybrid source which consists of a crystal target-radiator to generate the gamma ray beam and an amorphous target-converter where the positrons are produced in the gamma generated electromagnetic shower. In this framework, the Compton based polarized positron source is a good candidate at disposal to be an upgrade of the CLIC positron source and a polarized version of the ILC positron source¹. However, the number of positrons produced per bunch crossing is constrained due to the practical limitations of the laser pulse energy and the electron bunch charge. The parameters of the CLIC positron source as an example have been chosen to show the parametrization of the positron production. The simulations described above, in this case, show the production of $5.32 \times 10^7 e^+ / (\text{nC} \cdot \text{J})$ which is two (three) orders of magnitude smaller than the positron bunch charge required by the CLIC (ILC) design taking into account the present technology. Therefore, the accumulation of the produced positrons with the multiple stacking in the DR RF bucket should be performed until the requested positron bunch charge is reached [70, 130].

After the analysis of different systems, we can parametrize the requirements for the Compton based polarized positron source. For this, the final positron bunch population can be given by the following expression:

$$N_{e^+} = N_{e^-} \times \mathcal{E}_{\gamma/e^-} \times \mathcal{E}_{e^+/\gamma} \times \mathcal{E}_{e^+}^C \times \mathcal{E}_{e^+}^T \times N_s, \quad (4.1)$$

where N_{e^-} is the electron bunch population in the drive beam, $\mathcal{E}_{\gamma/e^-} = N_{\gamma}^{dia}/N_{e^-}$ is the efficiency of the polarized gamma ray production, $\mathcal{E}_{e^+/\gamma} = N_{e^+}/N_{\gamma}^{dia}$ is the polarized positron production efficiency, $\mathcal{E}_{e^+}^C = N_{e^+}^{pre-DR}/N_{e^+}^{targ}$ is the positron capture efficiency,

¹If the conventional or hybrid positron source will be chosen for the ILC injector baseline.

4.4 Impact of the results on the Compton based polarized positron source

$\mathcal{E}_{e^+}^T = N_{e^+}^{IP}/N_{e^+}^{pre-DR}$ is the positron transport efficiency and N_s is the number of stackings needed.

Let's assume an ERL based Compton source. According to the studies carried out, the following values can be assigned to each term of Eq. 4.1: the reasonable electron bunch charge of the ERL available at present is $N_{e^-}=3.13\times 10^9$; the simulation of the 5 IP MIPL with two crossed lasers configuration provides $\mathcal{E}_{\gamma/e^-} = 0.16$ together with the gamma ray polarization at the level of $\sim 38\%$; the simulations of the positron production show that $\mathcal{E}_{e^+/\gamma} = 0.2$ and the polarization of the positron produced is $\sim 36\%$; the simulations of the ACS give the positron capture efficiency at the entrance of the pre-damping ring $\mathcal{E}_{e^+}^C=0.16$; the positron transport efficiency has been assumed to be in the order of $\sim 50\%$ [12]; the number of injections in the same DR RF bucket N_s is considered as a free parameter depending on the injector design.

One can see that the N_{e^-} , \mathcal{E}_{γ/e^-} and N_s are the three parameters which primarily define the final positron bunch charge and depend on the ERL performance, laser power stored in the optical resonator and the possibility to increase the number of stackings. A graphical interpretation of the Eq. 4.1 and the impact of the electron bunch charge of the drive beam, gamma rays production efficiency (the laser pulse energy) and the number of stackings are shown on Fig. 4.12. Even at very high electron charge per bunch ~ 10 nC and high efficiency of the polarized gamma ray production ~ 0.8 (very high energy of the laser pulse) about 5 stackings are required. On the other hand, for a low laser pulse energy ($\mathcal{E}_{\gamma/e^-} \sim 0.1$) the number of stackings increases to 40.

Fig. 4.12 illustrates that approaching the target positron bunch charge goes along with extensive R&D and studies focusing on the three parameters: electron bunch charge, laser pulse energy and the number of stackings.

The “MightyLaser” experiment (see next Chapter), which confirms the gamma ray production given by the simulation and the experience of our Japanese colleagues [131] represents a promising continuation of the Compton based polarized positron source R&D. Moreover, the fast advance in the ERL and laser amplification technologies ensures possible improvements in the electron bunch charge and laser pulse energy in the nearest future, which can significantly relax the number of stackings required.

4. POSITRON SOURCE PERFORMANCE

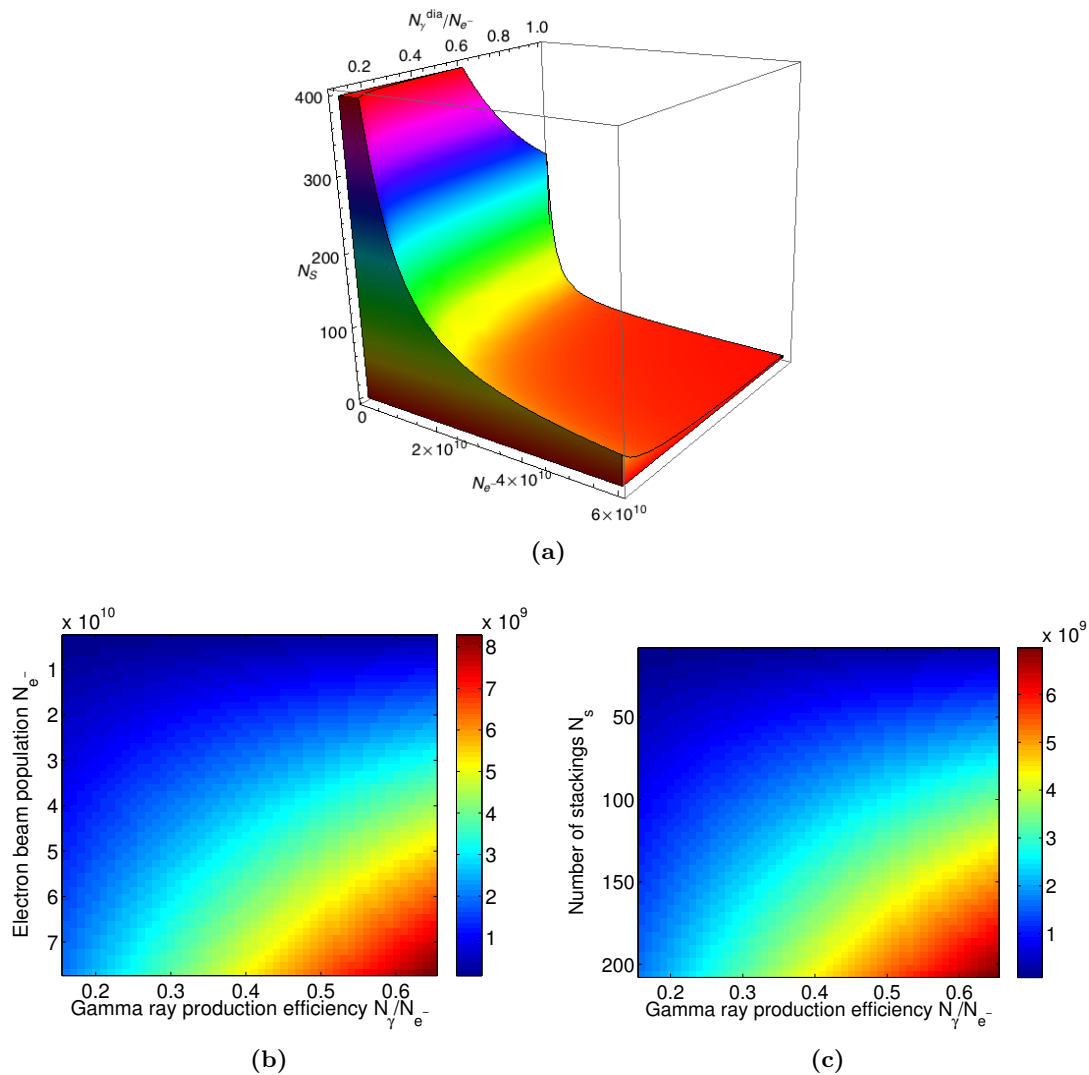


Figure 4.12: Efficiency of the Compton based polarized positron source - Fig. 4.12a shows the possible parameter space (N_{e^-} , \mathcal{E}_{γ/e^-} , N_s) ensuring the positron charge to be $\leq 4 \times 10^9$ positrons per bunch. Fig. 4.12b and Fig. 4.12c illustrate how the final positron bunch charge depends on the (N_{e^-} , \mathcal{E}_{γ/e^-}) and (N_s , \mathcal{E}_{γ/e^-}) parameter space respectively. The stacking efficiency of 10 injections per DR RF bucket has been assumed for Fig. 4.12b whereas for Fig. 4.12c the nominal electron bunch charge (0.5 nC) is used. The colorbar shows the positron bunch population.

5

Experiment: MightyLaser at KEK

5.1 Description of the experiment: a gamma ray factory

As discussed previously, the high energy physics as well as applied physics is strongly interested in intense fluxes of high energy X-rays and gamma rays. For some applications these gamma or alternatively X-rays can be generated by Compton scattering (see e.g. Section 2.6 or Chapter 3.2).

Development of various gamma ray/X-ray factories based on Compton scattering is ongoing around the world. As an example the High Intensity Gamma ray Source (HI γ S) in Duke University (USA) is in full operation and provides users with a gamma ray beam for scientific research [132, 133]. At this facility, the gamma ray beam is generated by colliding the electron beam with a Free Electron Laser (FEL) beam created by the same electron beam. The HI γ S is capable of producing gamma rays from 1 to 100 MeV with maximum gamma ray flux $10^{10}\gamma/s$ for ~ 10 MeV gamma rays.

However, a laser optical system can be used instead of a FEL facility to provide the low energy photon beam for the Compton collisions. In this case, to achieve a high flux of high energy photons despite the low cross section of Compton scattering, one requires a high average power laser system which can be based on a Fabry-Perot cavity together with a high current electron beam. In the context of polarized positron sources for future LC, a two-mirror Fabry-Perot cavity has already been successfully operated [134, 135] at the Accelerator Test Facility (ATF) [136] of the High Energy

5. EXPERIMENT: MIGHTYLASER AT KEK

Accelerator Research Organization (KEK) in Japan.

A solution to produce a high flux of circularly polarized gamma rays required for the polarized positron production is to use non-planar four mirror Fabry-Perot cavity (FPC) where laser pulses can be stacked to reach a high average power with small waist sizes at the interaction point (IP). This thesis was carried out in the framework of the project “MightyLaser”. For this project, a prototype of a non-planar high finesse four mirror Fabry-Perot cavity has been successfully built and installed at the KEK ATF, the final goal of “MightyLaser” is to test the production of the gamma rays. At the same time, this project will serve as a demonstrator for future technologies based on optical passive amplifiers such as Fabry-Perot cavities for low-energy electron machines (e.g. compact Compton X-ray sources like ThomX).

The optical system of the four mirror FPC has been commissioned during summer 2010 and electron-photon Compton collisions were observed on the first attempt in October 2010. In this Chapter the measurements of the gamma ray flux recorded during the first commissioning and its impact on the polarized positron source design are presented. The data analyzed here were taken before the tragic earthquake which struck Japan in March 2011. Further work will be done once the experimental setup will have been fully repaired.

5.2 Accelerator Test Facility at KEK

5.2.1 General overview of the ATF

A detailed description of the ATF at KEK can be found in [136, 137]. Originally, the ATF has been built to serve as a R&D facility to produce a small emittance electron beam in order to reach the nanometer sizes of the beams requested by the future LC. The ATF is comprised of a S-band linac, a Damping Ring (DR), and an extraction line. Fig. 5.1 shows a simplified layout of the ATF at KEK.

The DR has been designed to deliver this extremely low electron beam emittance as well as to test the advanced diagnostics tools and control systems to be used at the future LC. In such a way, in 2002 the ATF collaborators have reported the measured normalized electron beam emittance in horizontal and vertical plane to be respectively $\epsilon_x^n = 2.8 \times 10^{-6}$ m·rad and less than $\epsilon_y^n = 2.8 \times 10^{-8}$ m·rad at a beam energy of 1.3 GeV [138] which was the smallest normalized transverse emittance of the electron

5.2 Accelerator Test Facility at KEK

beam ever measured. Later, an extension called ATF2 has been constructed to test the focusing of the electron beam to nanometer beam size [139].

The working scheme of the ATF is the following: the electron beam accelerated up to the ~ 1.3 GeV by the linac is injected into the DR with a circumference of ~ 138 m. The 1.28 GeV DR has a revolution period of 462 ns corresponding to 2.16 MHz and operates at the radio frequency (RF) of 714 MHz. Electrons can be injected in 165 RF buckets spaced by 2.8 ns¹. Usually, the electron beam is injected into the DR with a repetition frequency of 1.56 Hz, stored approximately for a 480 ms (the beam is fully damped after approximately 200 ms) and then extracted in the ATF2. Although a total of up to 3 trains of 10 bunches separated by 5.6 ns can be injected in the ring (distance between the trains is 154 ns), most operations run with a single bunch per train or with a single train of up to 10 bunches [141]. The main parameters of the electron beam at the ATF DR are summarized in the Table 5.2.

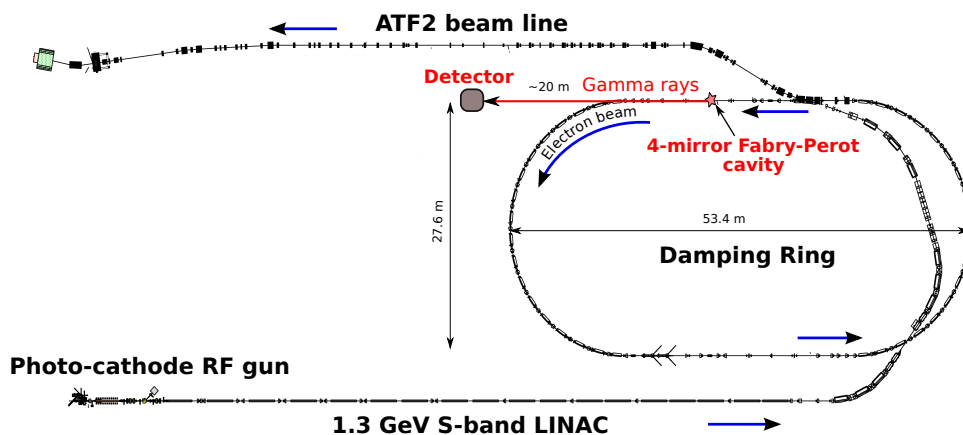


Figure 5.1: Layout of the Accelerator Test Facility at KEK - The red star indicates the approximate location of the four mirror Fabry-Perot cavity used for the measurements presented. The red arrow indicates the direction of propagation of the gamma rays produced. The grey box indicates the gamma ray detector.

The four mirror FPC is installed in one of the straight sections of the DR as shown on Fig. 5.1. So, in this straight section the electron beam collides with laser pulses

¹During the period of our experiment, the electron bunch repetition frequency was 178.5 MHz (5.6 ns bunch spacing). This allows studies concerning the extraction strip-line kicker for the ILC [140].

5. EXPERIMENT: MIGHTYLASER AT KEK

stored in the FPC. After the collisions the scattered gamma rays, propagating along the electron beam, are extracted through a window before passing through several collimators. They are measured by a gamma ray detector about 20 m downstream the IP.

5.2.2 Electron beam diagnostics in the ATF DR

The ATF status window as screen shots of the Wall Current Monitor (WCM) are recorded during “MightyLaser” operations to specify the ATF running conditions and the electron bunch charge (see e.g. Fig. 5.2). We also recorded the Beam Position Monitor (BPM) readings.

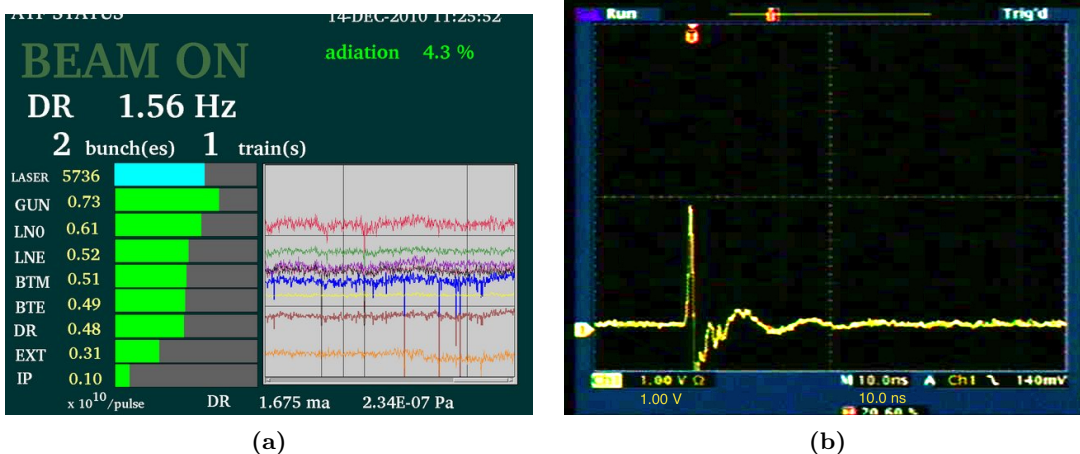


Figure 5.2: Illustration of the ATF running conditions - Fig. 5.2a shows the example of typical operation mode of the ATF. Fig. 5.2b shows a typical waveform of the WCM corresponding to the one bunch stored in the ATF DR.

The Beam Position Monitor (BPM) is one of the non-destructive beam diagnostics used for the different types of accelerators to measure the beam position in respect to the reference trajectory. The ATF DR is equipped with the 96 button BPMs [142].

Button type BPMs are made of four insulated electrodes (pickups) crosswise in the beam pipe [143]. The size of the button electrodes is 5–20 mm in diameter. The electric field of the charged particle beam induces the charge on the metal pickups placed at the beam pipe wall. According to Gauss law and Lorentz transformations, the charge (signal amplitude) induced in pickups by the charged particle bunch is proportional

to the bunch charge and inversely proportional to the distance to the beams barycenter. Therefore, by measuring the signal from the pickups, one can obtain the beam position (by making the difference in charge between the two opposite electrodes) and alternatively the charge (by making the sum of all the electrode charges) of the bunch.

The performance of the BPM is crucial to reach ultra-low vertical electron emittance. Therefore the BPMs of the ATF DR have recently been upgraded [144]. BPMs are also very important in the ATF2 to realize the fast feedback on bunch per bunch time scale and to achieve nanometer beam size.

During the data taking, the BPM readings have been used to monitor the position of the electron beam in the vicinity of the Compton IP as well as the electron bunch charge. The most relevant BPMs are those numbered 24 and 25 located upstream and downstream of the FPC. Fig. 5.3 shows typical distributions of the electron bunch charge and its horizontal and vertical positions recorded by the BPMs during the data taking.

5. EXPERIMENT: MIGHTYLASER AT KEK

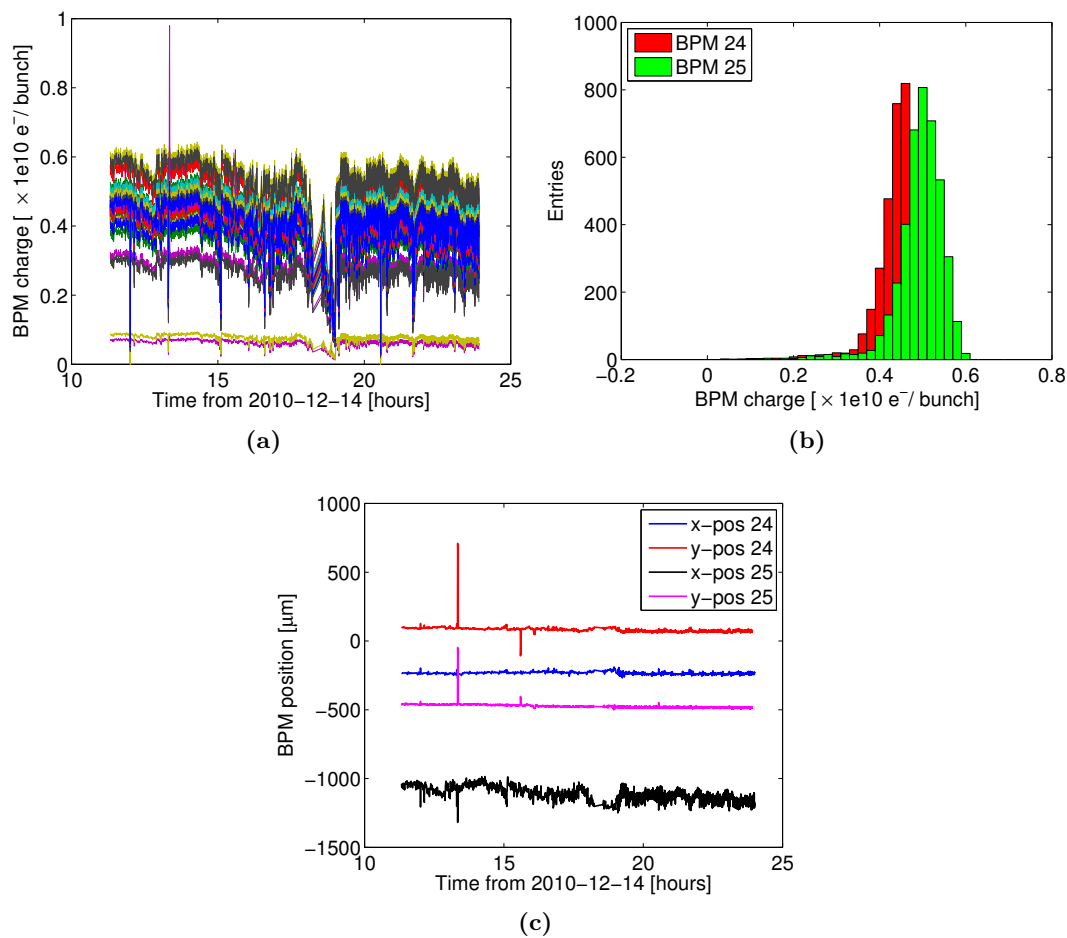


Figure 5.3: Beam Position Monitor readings during the data taking - Fig. 5.3a shows the charge measurements made by the different BPMs along the ATF DR. Different colors correspond to the readings of different BPMs. The histogram of the electron bunch charge measured by the BPM with the number 24 and 25 located on the different sides from the IP over 24 hours is shown on Fig. 5.3b. Fig. 5.3c shows the electron bunch position measurements done by the 24th and 25th BPM.

5.3 State-of-the-art of lasers and Fabry-Perot cavities

5.3.1 Laser for the Fabry-Perot cavity

As it was mentioned before, to provide an intense gamma/X- ray flux, a high average laser power is needed together with the ability for the laser system to work at high repetition frequency. At present, there is no direct amplification technology capable of reaching a sufficiently high average laser power and therefore passive optical resonators such as the FPC fed by the pulsed laser beam must be used. In this context, the laser should provide a stable, low phase noise pulse in order to be locked to a very high finesse¹ FPC. Such low noise performance can be achieved by commercially available laser oscillators [145]. However, due to the limited power they are capable of delivering (hundreds of mW), an additional laser amplification system has to be used before injection in the FPC.

In our case, this amplification system is based on the Chirped Pulse Amplification (CPA) technique. It implies that the laser pulses are stretched out temporally before the amplification and after this re-compressed to the length needed. This allows to decrease the possible non-linear effects during the pulse amplification. The whole optical system is shown on Fig. 5.4. Their main parts are the laser oscillator (Origami from OneFive GmbH) delivering 200 fs pulses of ~ 1030 nm wavelength at the repetition rate of 178.5 MHz, a stretcher unit, an Ytterbium (Yb) doped photonic crystal fiber as amplifier together with its pump source and a compressor unit. Using this setup, an average laser power of ~ 60 W has been achieved after the laser amplification stage. One of the reasons for choosing the fiber amplification is the fast progress of this technology. This can be observed on Fig. 5.5 where the main achievements in the CW fiber lasers are illustrated by plotting the power increase over the last years (see also [146]). In the pulsed regime, the authors of [147] reported the generation of 830 W average power from a CPA system working at 78 MHz repetition rate. However, the long term stability and reliability of such systems still requires extensive R&D [148].

¹Finesse F is one of quality characteristics of the FPC. It is defined as the ratio of the Free Spectral Range ($c/2L_{FPC}$) and the FWHM of a resonance. When the resonant conditions are fulfilled, the incident laser power is enhanced inside the cavity by a factor F/π , where $F = \pi\sqrt{R}/(1 - R)$ depends only on the reflectivity of the mirrors R .

5. EXPERIMENT: MIGHTYLASER AT KEK

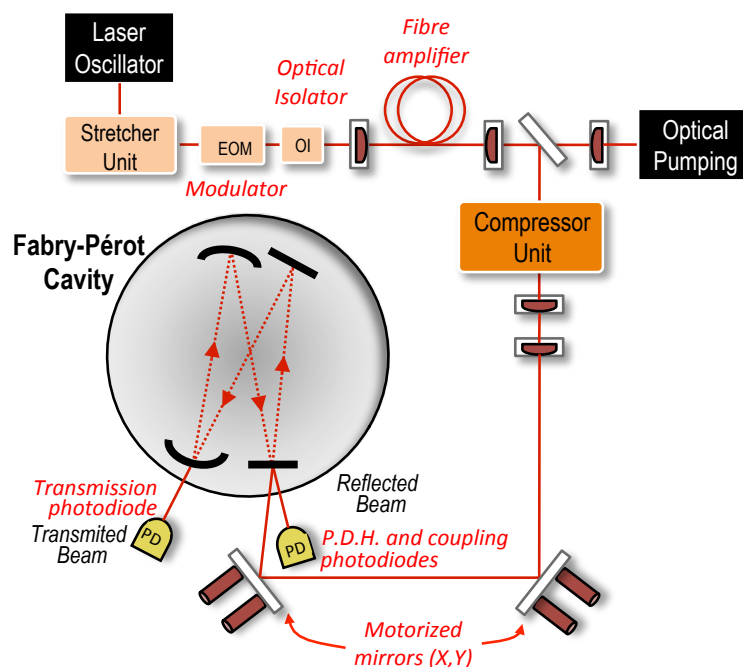


Figure 5.4: Optical system used for the laser power amplification and to inject the laser beam to the FPC - It includes a laser oscillator, a fiber amplifier and the FPC.

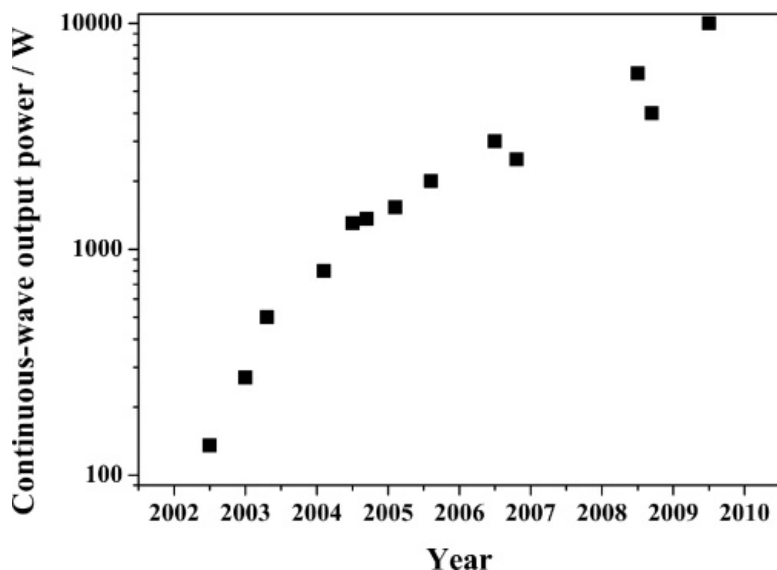


Figure 5.5: Illustration of the rapid advance in power of the fiber lasers - Power evolution of CW double-clad fiber lasers with diffraction-limited beam quality over the last decade. Figure is taken from [149].

5.3.2 Four mirror Fabry-Perot cavity

The design of a FPC for the accelerator facilities to deliver ~ 100 kW to 1 MW of average laser power is a big challenge. Recently, as part of the R&D program I. Pupeza et al. [150] reported that they achieved 72 kW of the laser power stored in a FPC working at 78 MHz repetition rate. At LAL, the possibility of stacking picosecond pulses inside the FPC with a finesse of 30000 at 76 MHz repetition rate has been demonstrated [151]. At accelerator facilities, in CW mode, a FPC with a finesse of 26000 and 30000 has been operated routinely at JLab [152] and HERA [153] respectively while in the pulsed regime a FPC finesse of 1000 [135] and 3000 [154] has been achieved. For the first time, the operation of a four mirror FPC with a finesse of 3000 at the accelerator facility has been demonstrated in the framework of “MightyLaser” project. More details on the experimental apparatus can be found in [79].

The four mirror configuration of the FPC has the advantage of being more stable than a two mirror configuration when providing a small waist of the cavity mode at the Compton IP [78, 155].

The FPC [79] is formed by two concave mirrors with a radius of curvature of 0.5 m and two flat mirrors. The mirrors have a very high reflectivity (1 - 1060 ppm for one of them and 1 - 330 ppm for the others) leading to a cavity finesse of the order of 3000 (that is a power enhancement of about 1000). In order to produce the polarized positrons later on, the FPC has a non-planar tetrahedron geometry which provides stable and circularly polarized fundamental eigenmodes [155]. The drawing of the four mirror FPC can be seen on Fig. 5.6. The FPC is mounted on a movable table which allows to scan vertically and horizontally the collision area in order to optimize the gamma ray production rate.

The duration of a round trip in the FPC is 5.6 ns (178.5 MHz) corresponding to the electron bunch spacing in the ATF DR. This allows to take advantage of the ATF DR multibunch operation mode. During one revolution made by the electrons in the DR (462 ns) the laser photons in the FPC perform 82.5 round trips. Therefore, the collisions on a given electron bunch occur only every other turn, at a frequency of 1.08 MHz. The main parameters are shown in Table 5.1.

According to Eq. 3.45, in order to increase the luminosity of the Compton collisions, the laser/electron beam crossing angle should be as small as possible (ideally “head-

5. EXPERIMENT: MIGHTYLASER AT KEK

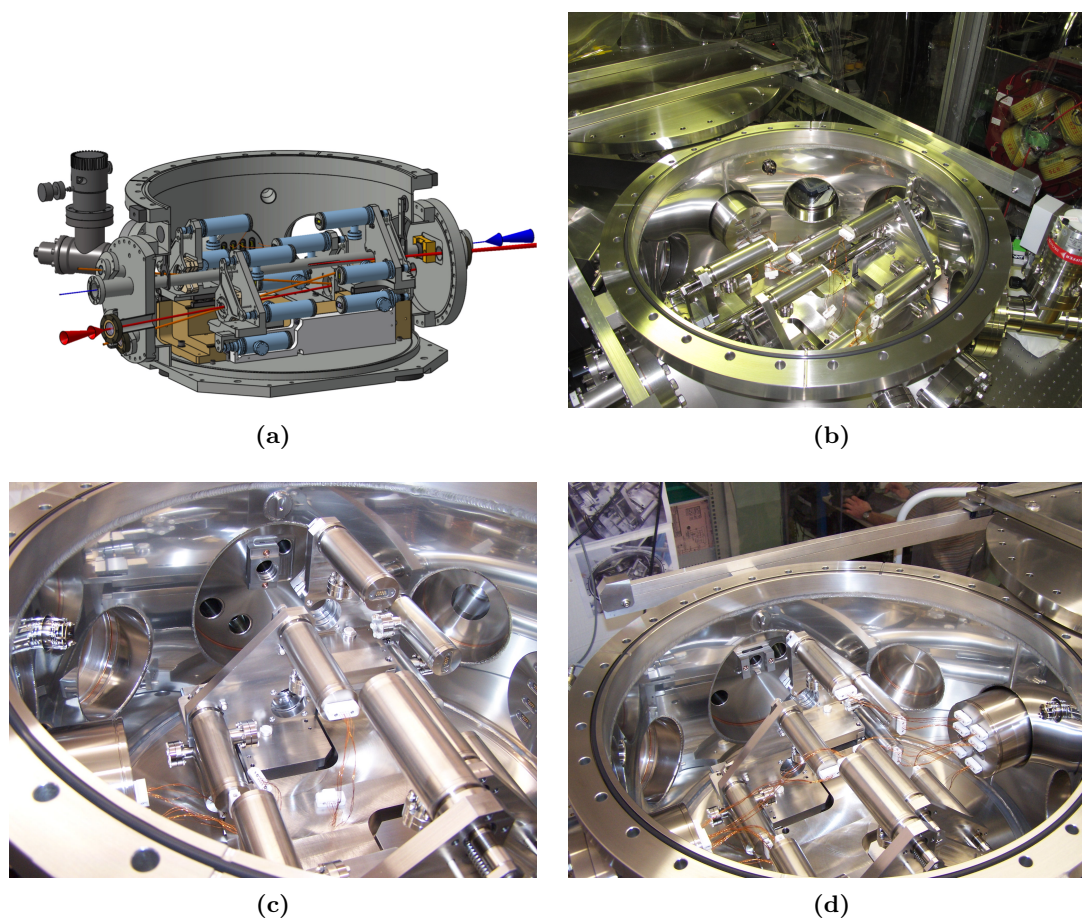


Figure 5.6: Vacuum vessel for the Fabry-Perot cavity installed at the ATF - Fig. 5.6a shows a drawing of the vacuum vessel together with the four mirror mounts and the beam pipe while Fig. 5.6b shows a real photograph of the FPC during the installation at the ATF DR. The blue arrow on Fig. 5.6a represents the direction of the electron beam whereas the laser beam direction is represented by the red arrow entering from the left side of the FPC. Fig. 5.6c and Fig. 5.6d show the photographs of different sides of the FPC: Fig. 5.6c points out the left side where the windows for laser beam injection, reflected and transmitted light and electron beam pipe are visible whereas Fig. 5.6d points out the opposite side of the FPC having two windows for transmitted light and one window for the electron beam pipe.

on” collisions). However, the FPC mechanical constraints set the crossing angle to be 8 degrees. Fig. 5.7 shows the dependence of gamma rays on the crossing angle. For our setup it results in the reduction of the gamma ray production rate by a factor of ~ 13 comparing to the “head-on” collisions.

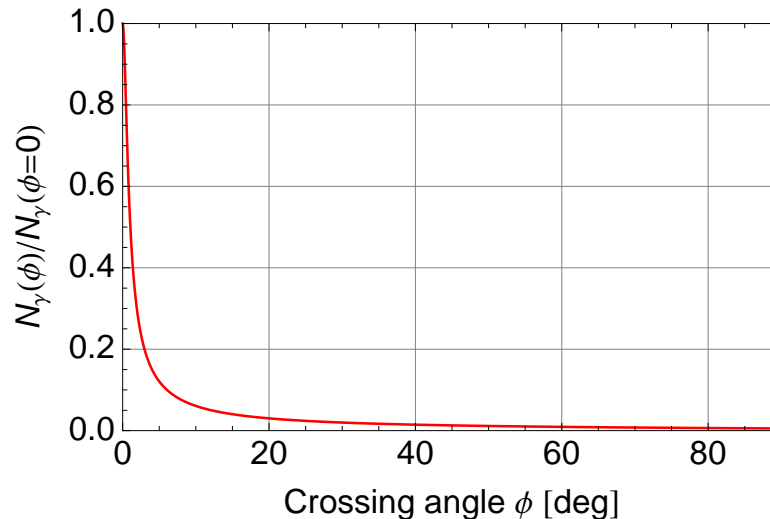


Figure 5.7: Dependence of the number of the gamma rays produced on the collision angle - the fast reduction of the gamma ray production rate is seen if an oblique collisions between the laser and the electron beam takes place. This reduction is also in strong correlation with the pulse lengths. For the parameters in Table 5.1 and 5.2 and at crossing angle of 8 degrees (0.139 rad), the gamma ray production rate is equal to 0.08 of that taken at zero crossing angle.

In our setup, there are two types of locking: locking of the laser beam to the FPC and the locking of the FPC to the ATF clock.

1. The width of the resonance peak is inversely proportional to the cavity finesse. In such a way the highest power enhancement factor of the FPC leads to the smallest width and thus to narrower resonances. This means that in order to maintain the cavity in resonance, one needs to match with high precision the FPC length and the laser beam repetition frequency. To ensure that the laser pulses are properly stacked in the cavity and to maintain the resonant conditions, a sophisticated feedback system is needed to lock the laser beam to the FPC. To accomplish this, the Pound-Drever-Hall (PDH) laser/cavity feedback method [156] has been implemented. For this, the initial laser beam is modulated and the effect of this

5. EXPERIMENT: MIGHTYLASER AT KEK

Description	Value
Laser oscillator power, P_{LO}	~ 200 mW
Laser photon energy, E_{ph}	1.2 eV ($\lambda_{ph} = 1032$ nm)
Laser spot size, σ_x/σ_y	26 / 38 μm
Laser frequency, f_L	178.5 MHz \pm 4 KHz
Finesse, F	~ 3000
Cavity enhancement factor, G	~ 1000
Laser pulse length, τ_L	68 ps (20 mm)
Average power stored in FPC, P_L	~ 160 W
Crossing angle, ϕ	8 deg.
Cavity length, L_{FPC}	1.7 m
Cavity mirror transmission@1035 nm, T	1060 ppm (1) /330 ppm (3)

Table 5.1: The main parameters of the laser system and the Fabry-Perot cavity installed at the ATF DR - laser beam parameters obtained during the experiment and which have been used for the various simulations.

modulations on the laser beam going out of the cavity is used. The best measured coupling between the laser beam and the FPC was measured to be about 60%.

2. It is also important to keep the correct phase between the ATF clock and FPC frequency to achieve stable Compton collisions. An all-digital ATF/FPC feedback system has been employed to lock the FPC on the ATF clock.

5.4 The IP physics

5.4.1 Expected gamma ray flux and energy spectrum

The simulation code CAIN has been used to simulate the Compton scattering process. This code simulates the interaction between one electron bunch and one laser pulse. Main parameters of the electron beam in the ATF DR are given in the table 5.2. Using these parameters and parameters listed in Table 5.1 the energy spectrum and the expected number of the scattered gamma rays per bunch crossing have been obtained (see Fig. 5.8). From this simulation we expect in average between 4 and 6 gamma rays per bunch crossing.

Description	Value
Electron energy, E_e	1.28 GeV
Electron bunch population, N_e	$\sim 0.5 \times 10^{10}$
Electron bunch length at injection, $\sigma_{z0}/c = \tau_{e0}$	~ 25 ps (7.5 mm)
Electron bunch length after damping, $\sigma_z/c = \tau_e$	~ 19 ps (5.7 mm)
Electron beam size, σ_x/σ_y	$\sim 110 / 10$ μm
Revolution period, T_0	462 ns
Emittance, $\gamma\epsilon_{x/y}$	$5 \times 10^{-6} / 3 \times 10^{-8}$ m·rad
Longitudinal damping time, t_{damp}	19.5 ms
Repetition frequency, f_{rep}	1.56 Hz (640 ms)
RF frequency of the DR, f_{RF}	714 MHz
Momentum compaction factor, α	0.002085
Harmonic number, h	330
Peak RF Voltage, V_0	250 kV
Energy spread at injection, ϵ_0	0.8 % FWHM
Energy loss per turn, $U_{synchRad}$	44 keV
Synchrotron frequency, Ω_s	10 kHz
RF bucket height, $(\frac{\Delta E}{E})_{max}$	0.012

Table 5.2: Parameters of the ATF DR - electron beam parameters obtained during the experiment and which have been used for the various simulations.

Due to the energy-angle correlation in Compton scattering, a single diaphragm acts as an energy filter. As it was mentioned before, the scattered gamma rays pass through several collimators before entering the detector. This provides a gamma energy spectrum selection owing to the energy-angle correlation in Compton scattering. Figure 5.8b shows the simulated energy spectrum of the gamma rays where the red color refers to the gamma rays transmitted by the collimators and blue color refers to the gamma rays filtered out due to their energy/angle.

The average energy of the gamma rays produced is ~ 15 MeV. However, due to the limited geometrical aperture (collimators), the gamma rays below 15 MeV do not reach the detector. Approximately, 43% of the initial gamma rays are accepted and the average energy of the gamma rays reaching the detector is therefore 24 MeV. Later, these results will be used for the Geant4 simulation and calibration of the calorimeter.

5. EXPERIMENT: MIGHTYLASER AT KEK

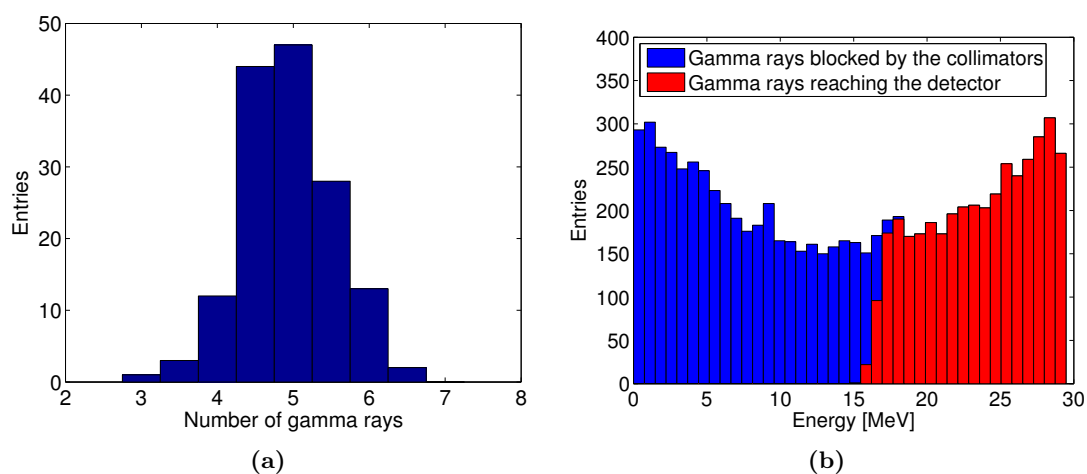


Figure 5.8: Expected energy spectrum and production rate of the gamma rays

- The number of gamma rays expected per one bunch crossing for the nominal parameters is shown on Fig. 5.8a. The energies of the gamma rays blocked by the collimators are shown on Fig. 5.8b as well as the energies of the gamma rays entering the detector. Only the gamma rays with energies above 15 MeV are accepted by the collimators.

5.4.2 Position sensitivity

It is important to investigate how the gamma ray production rate and therefore the intensity of the signal is affected by the position of the laser beam waist with respect to the electron beam position and time delay between the laser and electron beam. This is used to align properly the collision area and to maximize the yield of gamma rays. Fig. 5.9 shows the expected dependence of the number of gamma rays produced on the horizontal/vertical offset and delay between the electron and laser pulse in the case of 0 and 8 degrees collision angle.

As one can notice, the flux of gamma rays drops drastically with the increase of the horizontal and vertical offset for the “head-on” collisions. With the collision angle used by “MightyLaser”, for the nominal parameters, the most crucial parameter becomes the vertical misalignment (see Fig. 5.9b) since the horizontal one keeps the gamma ray flux constant along a large range (see Fig. 5.9a). We can see that with a vertical offset of $\sim 50 \mu\text{m}$ (~ 1.5 laser σ_y) the gamma ray flux drops by a factor 4 and it is almost zero for an offset of $100 \mu\text{m}$.

A non-zero time delay between the electron bunch and the laser pulse results in a rapid decrease of the gamma ray flux (see Fig. 5.9c). A delay of 100 ps (~ 25 degrees of ATF DR RF) leads to a drop of gamma ray flux by about 30%. This effect is strongly magnified in the case of 8 degrees collision angle (drop by about 60%).

In our setup we are able to adjust the horizontal and vertical position of the FPC in steps of $1 \mu\text{m}$ and the time delay by steps of less than 1 ps . The correspondent position and phase (timing) scans during the data taking will be discussed in Section 5.6.1.

5. EXPERIMENT: MIGHTYLASER AT KEK

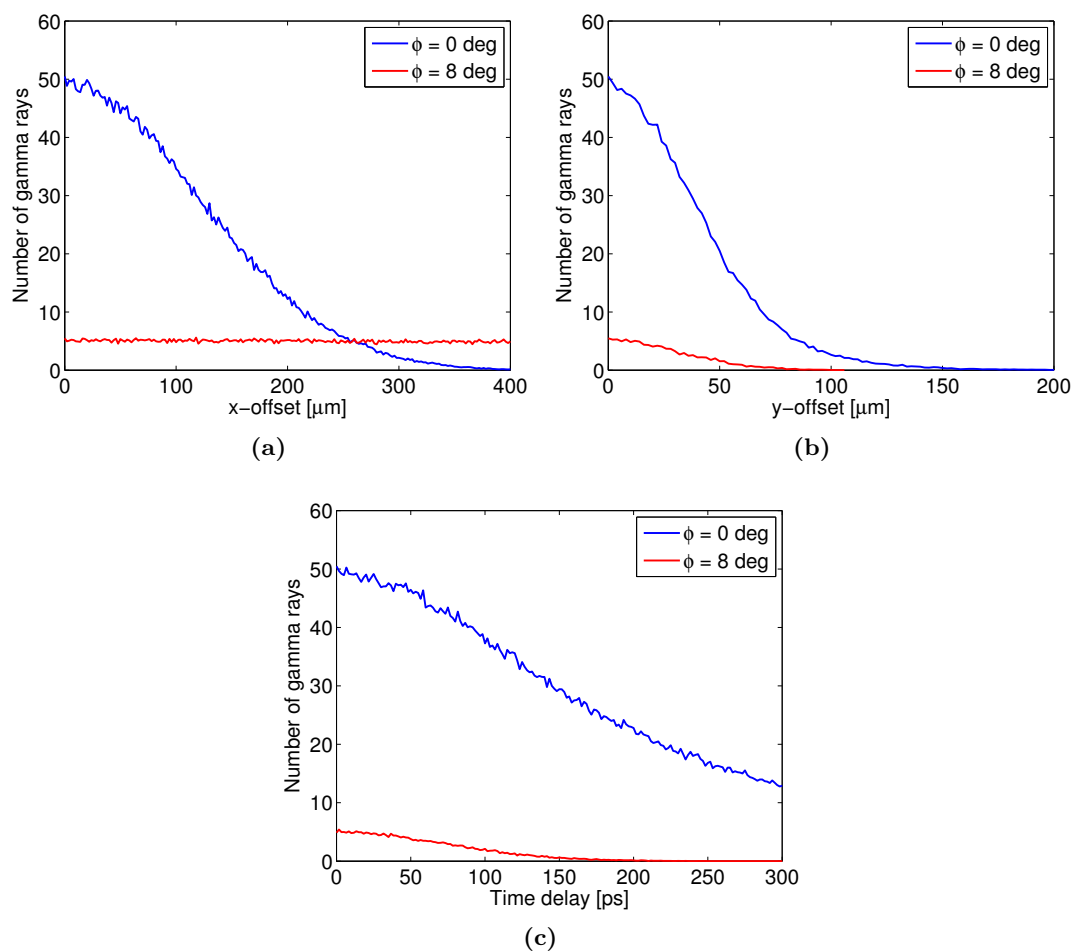


Figure 5.9: Dependence of the gamma ray production rate on the laser pulse offset and time delay with respect to the electron bunch for the nominal parameters. - Fig. 5.9a and Fig. 5.9b show the effect of a horizontal and vertical offset respectively whereas Fig. 5.9c illustrates the effect of the time delay. For our setup, the most important parameters therefore are the vertical offset and the time delay.

5.5 The gamma ray detector

To detect the gamma rays produced by the collisions between the laser photons and the electrons, we use a fast scintillation detector made of Barium fluoride (BaF_2) coupled with a Photomultiplier Tube (PMT). Two polished rectangular crystals of BaF_2 with dimensions $100 \text{ mm} \times 70 \text{ mm} \times 70 \text{ mm}$ each are glued to each other and wrapped into absorbing tape. The 200 mm depth of the BaF_2 calorimeter is nearly 10 radiation lengths, ensuring high detection efficiency.

Barium fluoride is commonly used since it has a fast response and two emission peaks at 220 nm and 310 nm with decay time constants of about respectively 0.8 ns and 630 ns (see Fig. 5.10a). To eliminate the scintillation from the slow component an optical filter has been installed in front of the PMT (see Fig. 5.10b). The decay time of the fast component of BaF_2 makes it possible to resolve two successive pulses of gamma rays generated from the electron bunches spaced by 5.6 ns. A fast PMT (Hamamatsu Photonics R3377) with a rise time of 0.7 ns is used. The main parameters of the detection system are listed in Table 5.3. The detector has been developed by Hiroshima university and more details can be found in [157].

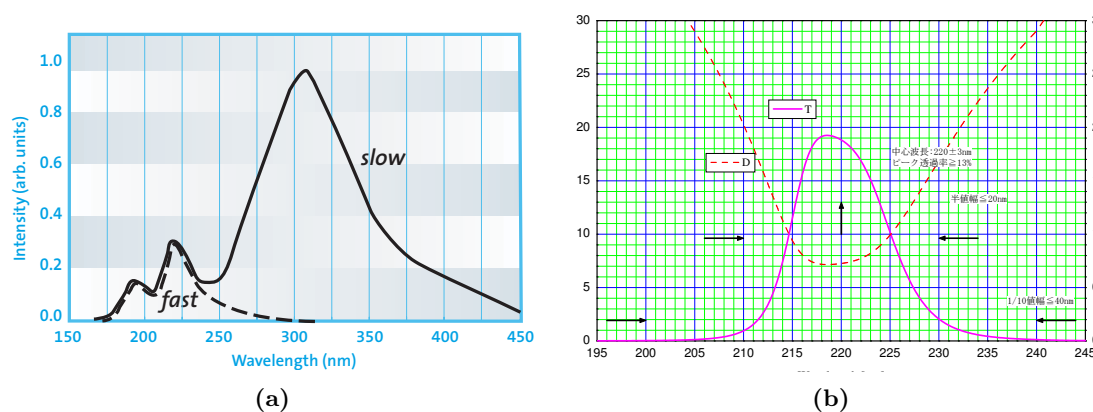


Figure 5.10: Emission spectrum of BaF_2 and transmittance of the UV-filter - Fig. 5.10a shows scintillation emission spectrum of BaF_2 [158] and Fig. 5.10b shows the transmittance of the optical filter to get rid of the slow component of scintillation. A pink solid line stands for the transmittance curve. On this plot, the abscissa is the wavelength in [nm] and the ordinate is the transmittance value in per cent [%].

5. EXPERIMENT: MIGHTYLASER AT KEK

Description	Value
Material of the scintillator	BaF ₂
Density of BaF ₂ , g cm ⁻³	4.89
Peak emission, nm	195 (f), 220 (f), 310 (s)
Decay time, ns	0.8 (f), 630 (s)
Detector size, mm	200 × 70 × 70
Light yield, ph/MeV	1800 (f) 10000 (s)
Radiation length, cm	2.06
Molière radius, cm	3.39
dE/dx for MIP, MeV cm ⁻¹	6.4
Refractive index	1.56 @ 200 nm
Optical filter pass band, nm	220 ± 10
Photodetector	PMT R3377
Rise time, ns	0.7

Table 5.3: Main parameters of the gamma ray detector - most of the parameters are taken from [158] [159] [160] [161]. The values marked by (f) are for the fast component and those marked by (s) are for the slow component.

5.5.1 Geant4 simulations

Using Geant4 [162], the development of electromagnetic showers inside the BaF_2 calorimeter (see figure 5.11) was simulated. This allows performing realistic estimations of the high energy gamma rays passing through the calorimeter. The initial distribution of gamma rays is obtained by using the code CAIN. The effect of the collimators to obtain a distribution of the gamma rays at the entrance of the calorimeter has been simulated as well. This distribution is used as an input for Geant4.

Once a gamma ray hits the calorimeter it generates an electromagnetic shower and scintillation light is uniformly emitted along the path of these charged particles. The number of optical photons is proportional to the energy loss of the impinging gamma rays. The scintillation light then is propagated and finally arrives at the PMT located at the end of the scintillator forming an electronic pulse. For the rough simulation of the PMT, it was assumed being composed of a quartz window and a photocathode. At the photocathode, the optical photon detection efficiency [163] is applied to estimate the PMT signal. Output for each Geant4 event is written to a ROOT [164] file for further analysis.

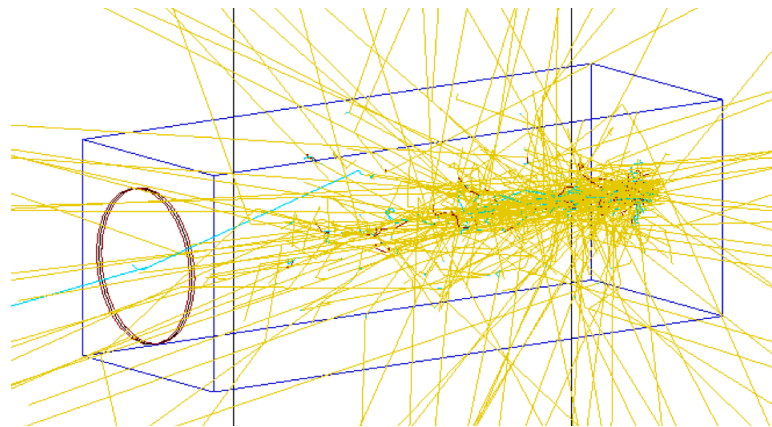


Figure 5.11: Development of an electromagnetic shower in the BaF_2 calorimeter - Shower created by 50 impinging gamma rays produced by Compton scattering. Gamma rays enter the detector from the right side. The tracks of the high energy gamma rays are depicted in yellow, tracks of the electrons in cyan and the tracks of the positrons in red. The photocathode to detect optical photons is modeled by a metal slab on the opposite side of the calorimeter. Impinging gamma rays and optical photons are not drawn.

According to the simulations, a large fraction of gamma rays interact along the

5. EXPERIMENT: MIGHTYLASER AT KEK

BaF₂ crystal while some of them pass through the calorimeter without interacting (see Fig. 5.12a). As illustrated on Fig. 5.12b, 98% of impinging gamma rays interact inside

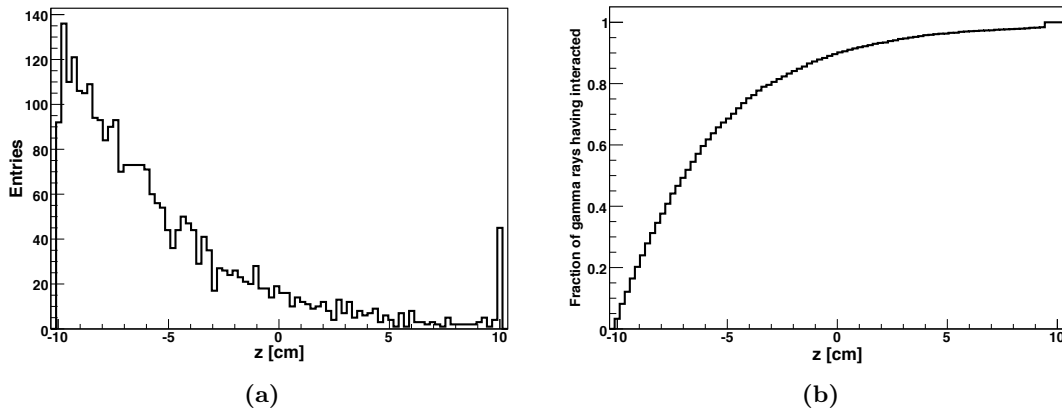


Figure 5.12: Interaction of the gamma rays inside the BaF₂ calorimeter - Fig. 5.12a shows the location of the first interaction vertex of initial gamma rays while the fraction of gamma rays having interacted in the calorimeter of different length is presented on Fig. 5.12b. The last bin on histogram 5.12a gives the number of gamma rays traversing the detector without having interacted.

the 20 cm long scintillator while for shorter crystal length like 10 or 5 cm, this number drops to 87% and 64% respectively. Thus, a shorter crystal reduces the efficiency and the nominal BaF₂ crystal length ensures high detection efficiency as was indicated before.

Fig. 5.13 shows the distributions of the optical photons produced in the BaF₂ calorimeter. Most of the optical photons are produced at the beginning of the scintillator (see Fig. 5.13a). These optical photons have smaller probability to reach the PMT due to absorption on the sides of the calorimeter. In such a way, the optical photons which hit the PMT are produced inside the scintillator almost uniformly (see Fig 5.13b). In the transverse plane (see Fig. 5.14b), one can see that the optical photon flux is more intense close to the axis.

The BaF₂ crystal is wrapped in absorbing tape on all sides except the optical exit where it is polished and coupled to the PMT. The effect of the absorbing tape is that the photons reaching the photocathode have in most cases not undergone any reflection and their arrival time is well defined. Fig. 5.13b shows that about only 11% of the photons reaching the PMT have undergone at least one reflection in the crystal before reaching

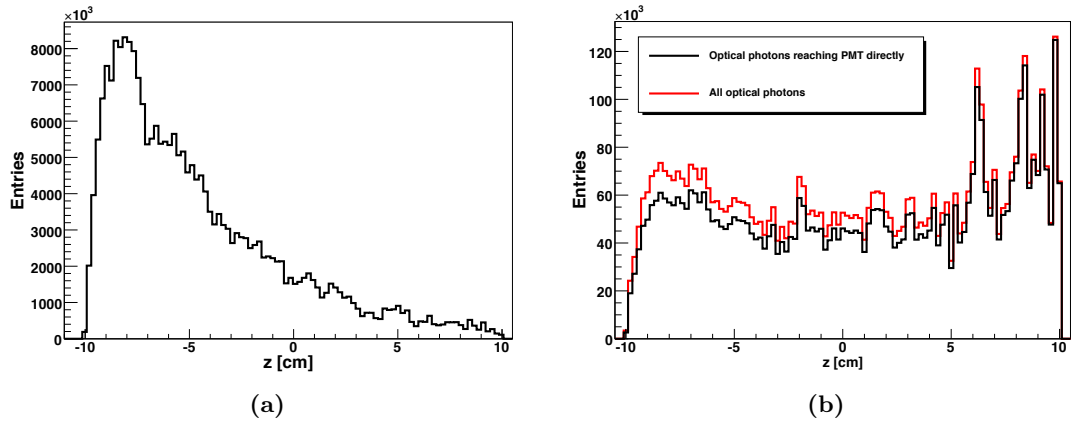


Figure 5.13: The distribution of the optical photons produced in the BaF₂ calorimeter - Fig. 5.13a shows the position inside the scintillator where the optical photons have been produced. Fig. 5.13b shows the optical photons which are within the PMT acceptance and reach the PMT directly (black curve) or all the optical photons arriving at the PMT (red curve). The difference between the two is the number of optical photons which underwent at least one reflection.

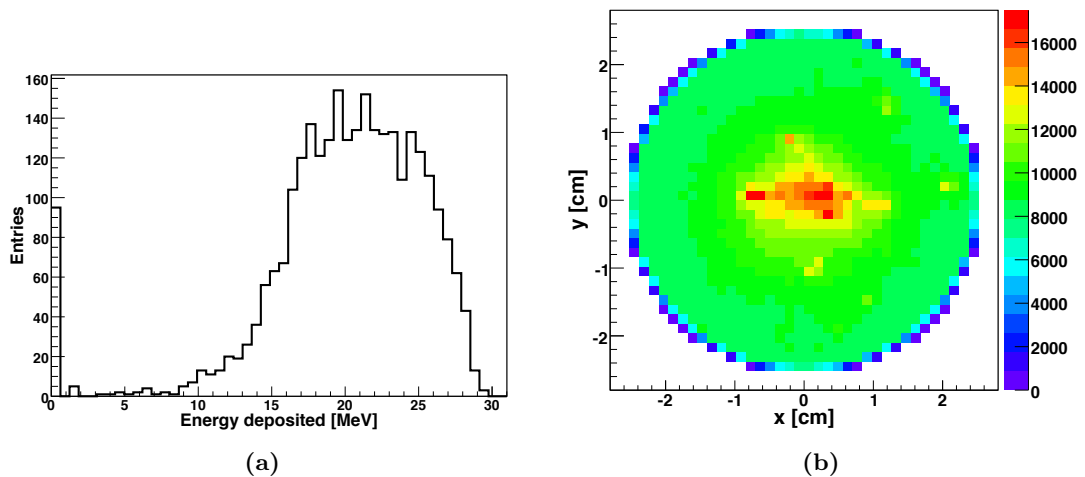


Figure 5.14: Energy deposited in the scintillator and the optical photon distribution at the PMT - Fig. 5.14a shows the energy deposited by the gamma rays in the BaF₂ calorimeter with a mean value of 20 MeV. Fig. 5.14b shows the transverse distribution of the optical photons at the PMT location.

5. EXPERIMENT: MIGHTYLASER AT KEK

the PMT. The simulations show that the average energy deposited equals 20 MeV as illustrated on Fig. 5.14a.

5.5.2 Data acquisition system

The data acquisition relies on several oscilloscopes. Two oscilloscopes (Tektronix) are used to monitor the status of the FPC (RF clock, RF phase, laser coupling with the FPC, lock status, power stored in the FPC, etc.) and a third oscilloscope, with an on-board computer, is used to record the signal coming from the calorimeter as well as reference signals (ATF clock, injection trigger and FPC stored power). The detection setup is based on the last one, a LeCroy WS454 oscilloscope (1GS/s, 500 MHz bandwidth). The three oscilloscopes are located inside the ATF tunnel and are not directly accessible during the accelerator operations. They are connected to the outside world via an ethernet network.

A server located outside the ATF tunnel is used to collect information during data taking. Two independent scripts running on this server are used to send over http the commands to download the data displayed on these scopes. Once these data are received they are timestamped and stored in a MySQL database. For the third scope the data acquisition goes in the other direction: when a waveform is recorded it is saved locally and a MySQL request is sent to store the timestamped filename in the database. The file is then moved to a disk shared by the server. Another script running independently on the server connects at regular intervals to the ATF Server using EPICS [165] to download the current accelerator status parameters (e.g. BPM readout, FPC movers positions).

FPC operators can access all the informations collected by the server by accessing a web page on the local network. This webpage is dynamically updated using the information in the MySQL database. A schematic drawing of the acquisition system is shown in Fig. 5.15.

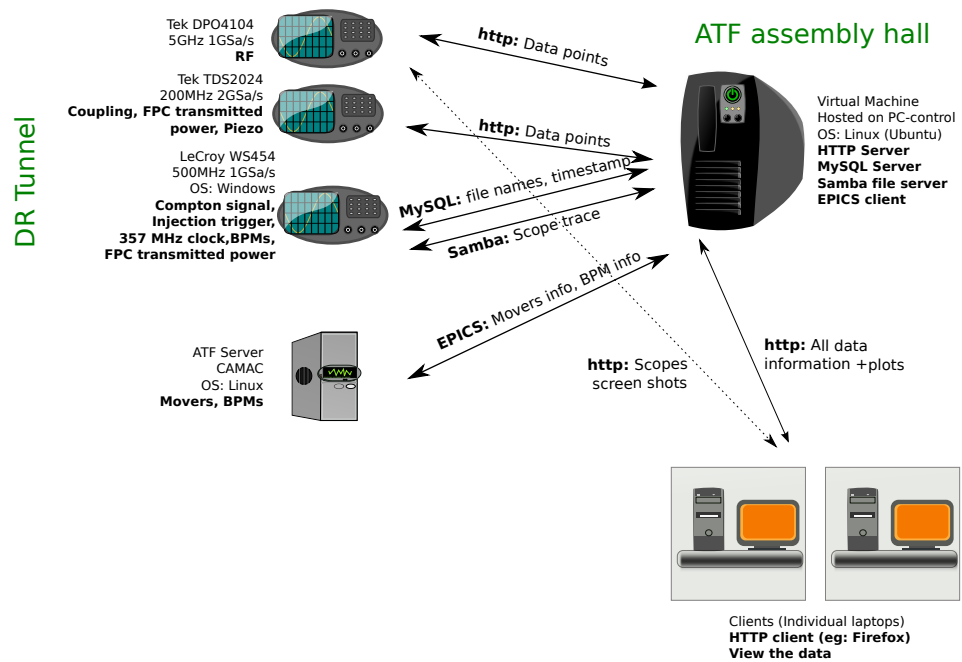


Figure 5.15: Layout of the data acquisition system - a central computer uses network connections to connect to oscilloscopes located in the ATF tunnel and to collect informations about the accelerator status. The same computer can also deliver these informations to operators connected over the network from the control room.

5. EXPERIMENT: MIGHTYLASER AT KEK

5.5.3 Calibration

In the energy range of interest (tens of MeV), the calorimeter can be calibrated using cosmic rays muons. This is possible because the cosmic rays muons have a mean energy loss rate close to the minimum and can be considered as minimum ionizing particles [117]. Therefore the energy loss of the muons in BaF₂ is well known. The calibration gives us a relation between the oscilloscope measurements (voltage and signal shape) and the energy deposited in the calorimeter. The height and integral of the signal have been used as a measure of energy lost by the gamma rays.

In calibration mode the coincidences between two plastic scintillators, one placed at the top and the other at the bottom of the calorimeter, are used to trigger the data acquisition (see Fig. 5.16) [157]. The signal from the PMT is then digitized by the oscilloscope used to acquire the Compton data. Calibration measurements were performed before each data taking run.



Figure 5.16: Schematic layout of the calibration setup - The two plastic scintillators read out by PMT 1 and PMT 2 are used to trigger the data acquisition of PMT 3 reading the BaF₂ crystal.

A typical measured distribution of pulse heights and pulse integrals is shown on figure 5.17.

For detectors of moderate thickness such as the one we are using, the energy loss probability distribution is described by the Landau distribution [166] and the most

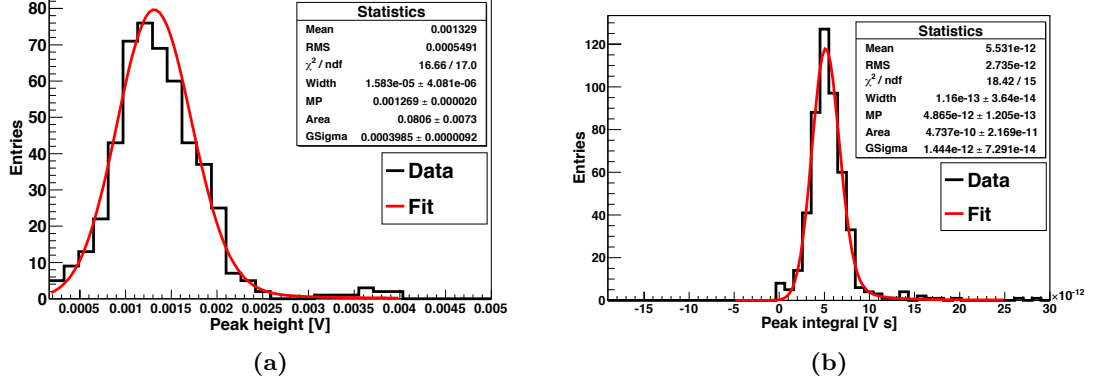


Figure 5.17: Calibration of the gamma ray detector - Energy loss distribution of the cosmic muons in the calorimeter. Fig. 5.17a shows the histogram of the peak heights and figure 5.17b shows the histogram of the peak integrals. A Landau distribution fit with parameters is shown in both cases.

probable energy loss of cosmic muons is given by the most probable value (MPV) of a Landau distribution.

According to our calibration, the MPV for the integrated signal is (4.87 ± 0.12) mV·ns and the MPV for the peak height distribution is (1.27 ± 0.02) mV. Assuming minimum ionization, the energy deposition in the calorimeter is 6.374 MeV/cm [167]. This value corresponds to approximately 45 MeV of energy deposited by a muon passing through the calorimeter. However, this value should be corrected to account for the geometry and the acceptance of the detection system.

To do so, the measure should be scaled by the ratio between the total number of optical photons produced in the BaF₂ crystal and those optical photons which are within the PMT acceptance. Another correction factor appears due to the fact that the two surrounding plastic scintillators are not fully covering the surface of the BaF₂ crystal. Therefore, the previous factor has to be corrected to take into account this difference in overlapping surfaces.

To address these two issues we used a Geant4 simulation of the detector. The ratio of the optical photons produced in the calorimeter and those which are within the PMT acceptance has been calculated (F_1). Then, this ratio has been estimated only for those optical photons which are within the acceptance of two plastic scintillators used for the

5. EXPERIMENT: MIGHTYLASER AT KEK

calibration (F_2) (see Fig. 5.18). This can be summarized by the following expression:

$$E_\gamma[\text{MeV}] = \frac{V_\gamma[\text{mV}]E_\mu[\text{MeV}]}{V_\mu[\text{mV}]}F, \quad F = \frac{F_1}{F_2}, \quad (5.1)$$

where

$$F_1 = \frac{N_{ph}^{All}}{N_{ph}^{PMT}}, \quad F_2 = \frac{N_{ph}^{All,calib}}{N_{ph}^{PMT,calib}}$$

and V_γ is the voltage read from the oscilloscope corresponding to the energy deposited by the gamma rays E_γ whereas V_μ and E_μ are those values for the cosmic ray muons. The simulations provide a correction factor F which is equal to $0.745 \pm 0.001(\text{stat}) \pm 0.04(\text{syst})$. Statistical error is estimated based on the statistics of the simulation and systematic one is based on the uncertainty on the measurement of the calibration volume.

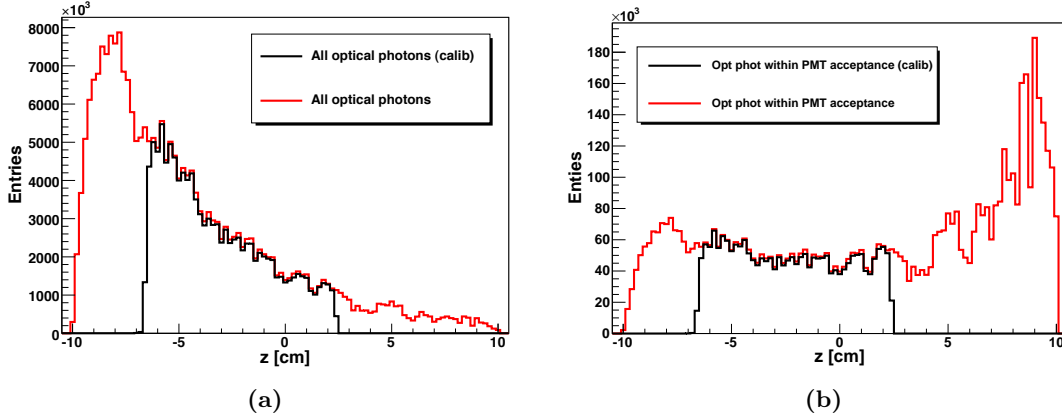


Figure 5.18: Illustration of the correction factors used for the calibration - Fig. 5.18a shows the distribution of all the optical photons produced in the calorimeter and those optical photons produced within the acceptance of the calibration setup. Fig. 5.18b shows the optical photons which are within the PMT acceptance together with those photons which are in calibration acceptance.

Once, all corrections have been applied, a peak height of 1 mV and peak integral of 1 mV·ns is equivalent in average to (26.6 ± 1.9) MeV and (6.9 ± 0.5) MeV of energy deposited in the calorimeter respectively.

5.6 Data analysis and results

5.6.1 Scanning procedure and the first data

The FPC was operated in October 2010 and Compton collisions were recorded on the first attempt (October, 26). Before data taking we investigated how the intensity of the signal is affected by the position of the laser beam waist with respect to the electron beam position and synchronization between the laser and electron beam by performing position and phase scans.

The search for the collisions area between the electrons and the laser photons has several degrees of freedom and is not straightforward. The two most sensitive degrees of freedom are the vertical position of the FPC (dimension orthogonal to the plane of the beams) and the relative phase between the laser and the electrons (time dimension). When the FPC frequency is locked on the frequency of the ATF clock, the relative phase between the electrons and the laser is constant and it needs to be changed manually. While searching for the collision point we offset the FPC frequency by at least 100 Hz with respect to the ATF frequency. By doing this the relative phase between the electrons and the laser is automatically scanned at a rate of at least 100 Hz.

A slow sweep of the vertical position of the laser then allows to quickly scan most of the parameters space. While performing this scan we look on the data acquisition oscilloscope for the apparition of short bursts in the output of the PMT (see Fig. 5.19). The length and the frequency of these bursts are related to the difference between the frequency of the cavity and the frequency of the ATF clock.

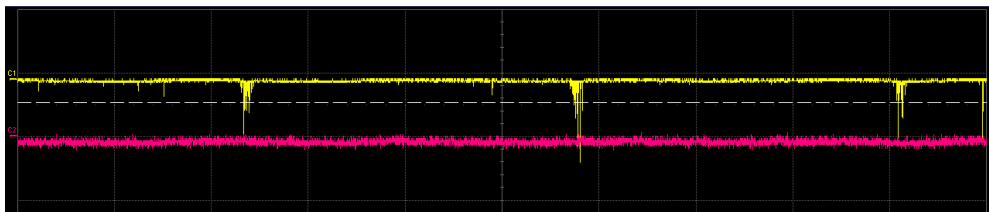


Figure 5.19: Example of signal observed on the oscilloscope while scanning the parameters space to find the collision area - The yellow line is the signal from the PMT. The duration of the waveform is 10 ms and the vertical scale is 200 mV (on this day the signal was amplified). The red line records the injection trigger (the trigger itself is off the screen).

On Fig 5.19 the bursts correspond to the time at which the phase of the laser

5. EXPERIMENT: MIGHTYLASER AT KEK

matches that of the electrons. The distances between the bursts correspond to the difference between the ATF frequency and the laser frequency. Each burst contains several peaks spaced by the duration of two DR revolution. It was checked that the bursts on the yellow lines disappear when the cavity is moved vertically by a distance greater than the beam size.

Once these bursts have been detected the vertical position of the laser is adjusted to maximize their intensity providing the vertical position scan (see Fig. 5.20). Fig. 5.20a shows that the gamma ray flux reaches its maximum at the relative position of the mover $\sim 120 \mu\text{m}$. By doing a Gauss fit, the mean value of $-124 \mu\text{m}$ with a standard deviation of $70 \mu\text{m}$ have been retrieved (see Fig. 5.20a). The experimental result can be compared to the simulation showing in Fig. 5.20b. This allows finding the offset made by the mover system with respect to a zero vertical offset. In the case of the simulation, the Gauss fit gives a zero mean with the standard deviation of $45 \mu\text{m}$. The agreement between the experiment and simulation is reasonable. The small difference in width may be explained by not being exactly on the beam waists when this scan was performed.

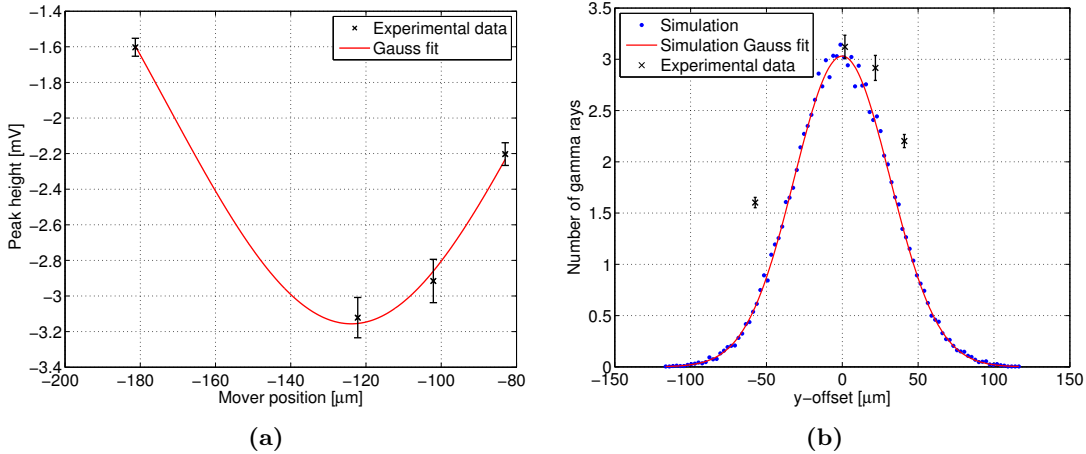


Figure 5.20: Vertical position scan - Fig. 5.20a shows the vertical position scan done during the one of our data takings. Peak height is a measure of energy deposited in the calorimeter and stands for the intensity of the Compton signal measured by the oscilloscope. Fig. 5.20b shows the simulation of the vertical offset fitted by a Gauss distribution together with the experimental data points. In this case the cosmic ray calibration has been used to find the number of gamma rays produced by the experiment.

At this stage the laser frequency can be locked on the ATF frequency. As the relative phase between these two frequencies is unknown¹ it must be swept to optimize the intensity of the signal observed on the PMT output.

5.6.2 Data taking and an example of the data

During data taking we record the signal from the PMT as well as the 357 MHz ATF clock and the laser power transmitted by the FPC and measured by a photodiode. To avoid the misleading noise from the injection or extraction kickers a typical data acquisition starts at least 200 ms after the injection trigger is received. At this time we expect the beam to be almost fully damped. A typical signal waveform from the calorimeter can be observed in Fig 5.21. A full waveform contains approximately 200 000 samples spaced by 1 ns.

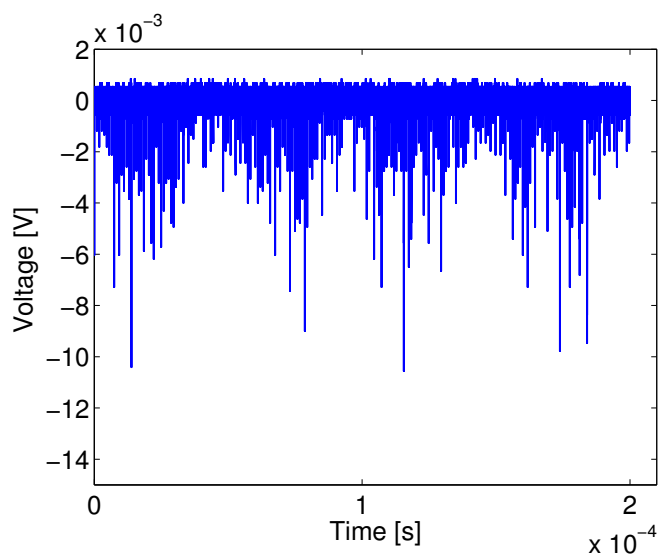


Figure 5.21: The typical signal shape for the high energy gamma rays produced by Compton scattering observed at the anode output of the PMT - Each spike on the picture corresponds to the gamma production after successive bunch crossings over 0.2 ms. Data shown correspond to a single bunch stored in the ATF DR.

¹Our experience shows that the variation of this phase from day to day is small. However, we do observe small drifts, which require a new phase scan on each run.

5. EXPERIMENT: MIGHTYLASER AT KEK

5.6.3 Data analysis technique

The raw data recorded contain the signal read from the PMT output as a function of time (see Fig. 5.21). Data analysis was carried out to extract the intensity of the Compton signal and remove unwanted backgrounds. Matlab [168]/Octave [169] framework have been used to perform data analysis. After experimental data processing, the results are saved in the MySQL database for further analysis.

As the data were acquired during different ATF runs with different filling modes of the DR (1 train, 2 trains, 3 trains stored in the ATF DR) the correct number of Compton peaks and their timing must be found. The 357 MHz ATF clock is used to define the beginning of a 924 ns periods corresponding to the occurrence of the Compton signal (two ATF DR revolutions). All 924 ns periods belonging to one data file (usually 0.2 ms long) are superimposed on top of each other to find the number of the peaks per revolution and their time of arrival with respect to the beginning of the period. Such technique is used to enhance statistically the signal over the background reducing at the same time the electronic noise. This results in a more precise way for the estimation of the number of the peaks and their timing. An example of such period stacking can be seen on Fig. 5.22a.

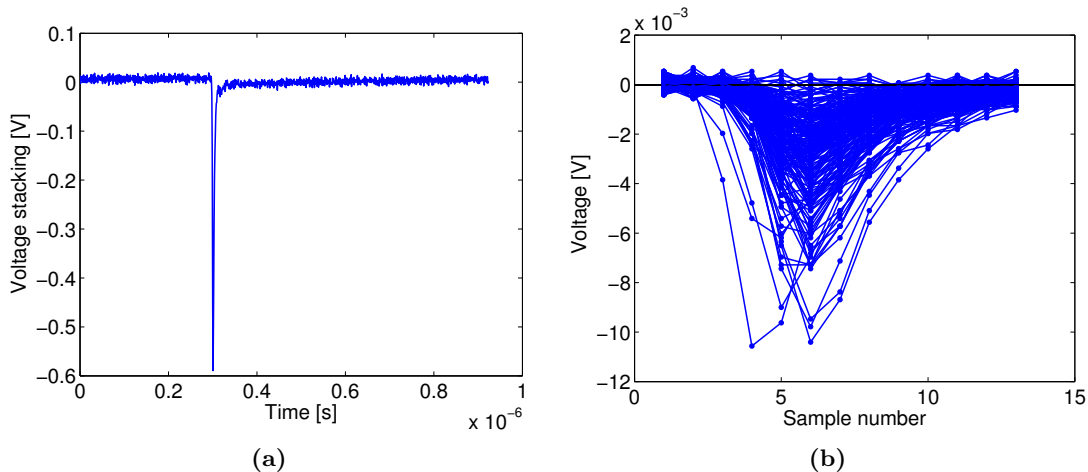


Figure 5.22: Example of the stacking of the 924 ns periods - Fig. 5.22a shows stacking of all the 924 ns periods from the data file presented on Fig. 5.21. This stacking is used to find the number of the peaks and their timing. Time profile of the signals for all the periods from the same file is shown on Fig. 5.22b.

Once the number of peaks and their positions within the period is found we define a gate around the position where the Compton signal is expected. We use this gate to calculate the height and integral of the peak. The Compton peak height and its integral are our measure of the energy deposited by the gamma rays in the calorimeter. The length of the gate is set to 12 ns in order to entirely contain the signal thus ensuring a correct evaluation of the energy deposited. The signal distribution in such gates around the peak is presented on Fig. 5.22b.

The background level and its RMS are calculated within each period and are subtracted from the corresponding peak height and peak integral. The background level is defined as the mean over the timebase corresponding to a given period excluding the gate containing the signal. The average background level and its RMS for our data sample is estimated to be around $7 \mu\text{V}$ and 0.2 mV respectively. Finally, the peak height and peak integral are calculated for every peak within the period (see Fig. 5.23a).

The shape of the detector's response creates a linear relation between the total charge and the maximum charge measured. This can be seen as a correlation between the calculated peak height and peak integral as shown on Fig. 5.23b

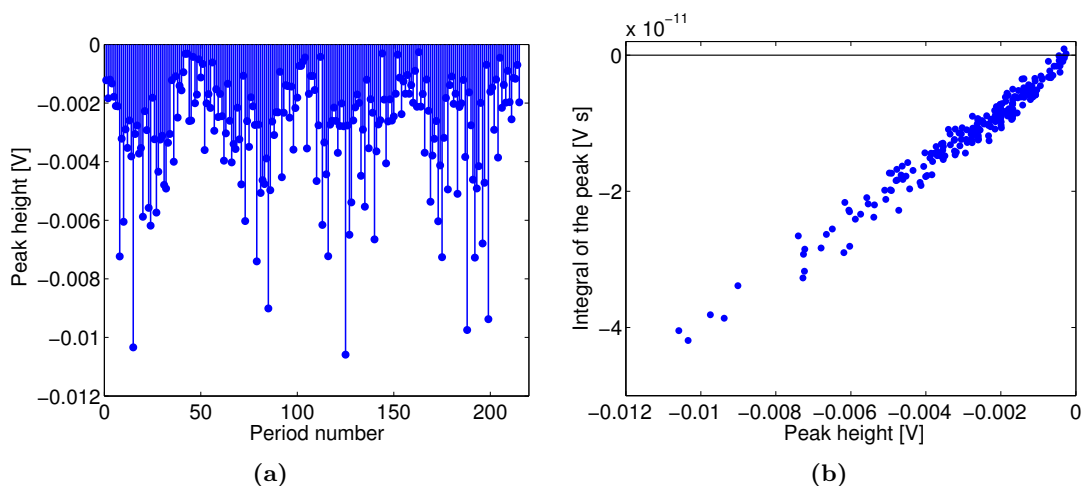


Figure 5.23: Illustration of the peak height distribution - Fig. 5.23a gives an example of the peak height distribution from the data file presented on Fig 5.21. Peak height vs. peak integral for the same data file is shown on Fig. 5.23b.

5. EXPERIMENT: MIGHTYLASER AT KEK

Quality of the data. Different quality cuts are applied to restrict the analysis to a high purity sample. By putting limitations we can reject noise and obtain a set of good quality data (see Fig. 5.24).

1. We require for all the Compton peaks within one file to have the same phase with respect to the ATF clock. This fixes the synchronization between the Compton signal and the beginning of the gate implying Compton signal to arrive 6 ns after the beginning of the gate (see Fig. 5.24a). For the future, it will be possible to profit from a new feature of the upgraded DAQ system, to start the acquisition on an ATF turn by turn trigger after the ATF injection trigger. By doing this, the distance between the beginning of the period and the Compton peak will be fixed. This will enhance the background rejection and make the data analysis much easier.
2. Sometimes, the noise can dominate the signal (see Fig 5.24b). Quite often, these signals can even lead to an integral value with the wrong sign. This is illustrated on Fig. 5.24c by the dots with positive values of the integral of the peak. Such events have to be considered as picked up noise and must be rejected. For this, we introduce a “contrast” variable:

$$V = \frac{2I_{max}(t_0)}{I(t_0 - 1) + I(t_0 + 1)}, \quad (5.2)$$

where $I_{max}(t_0)$ is the intensity of the signal taken at the time when it reaches maximum, $I(t_0 - 1)$ and $I(t_0 + 1)$ are the intensities of the signal in the two nearest data points. By imposing $1 \leq V \leq 10$ the noise is filtered out as V reaches either negative or very high positive values for noise signal. In Fig 5.24b the magenta line corresponds to the real Compton signal for which our estimator variable V is about 1 while the red and blue lines are for the noise events and in this case V equals to -2 and 17 respectively.

The effect of the cuts mentioned above is shown in Fig. 5.24c. The cut on the signal arrival time preserves a good linear relation between the peak height and peak integral apart from a few high intensity data points for which our data acquisition system saturated. The cut on the shape of the pulse helps to remove the noise. However, some low intensity events still remain, which correspond to low energy depositing by the gamma rays in the calorimeter.

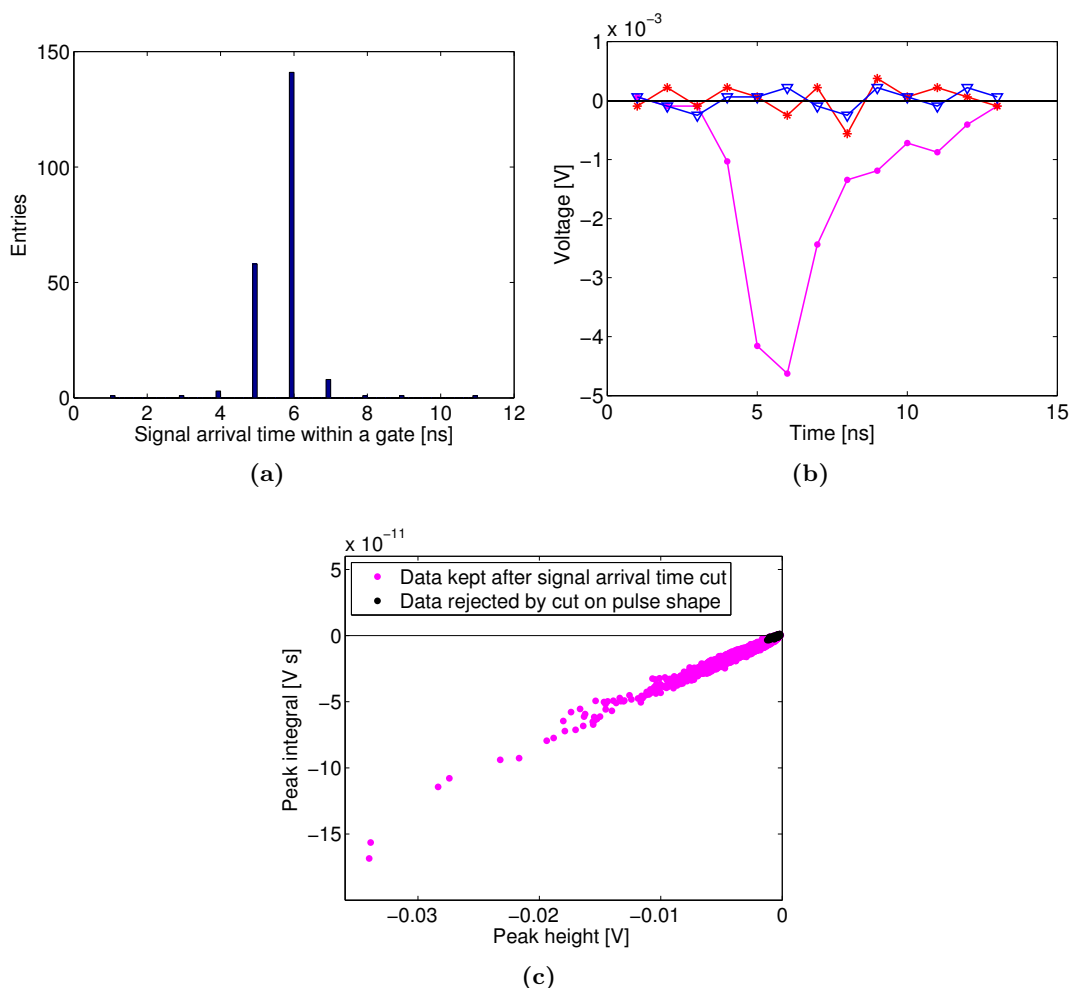


Figure 5.24: Illustration of the quality cuts together with their effect on the data sample - Quality cut illustration (Fig 5.24a and 5.24b) shown together with their effect on all the data sample (Fig. 5.24c). Fig. 5.24a: the distribution of the signal arrival time within the gate for all the signals found in the data file presented on Fig. 5.21. Fig. 5.24b gives an example of a correct signal (magenta line, $V = 1$) as opposed to the noise signal (blue, $V = 17$ and red, $V = -2$ line). Fig. 5.24c shows the data sample remaining after the cut on the signal arrival time applied (magenta points) together with the events which are rejected due to the cut on the shape of the pulse (data points tagged in black).

5. EXPERIMENT: MIGHTYLASER AT KEK

Background While analysing the data we noticed that some data files contain peaks spaced by about 462 ns corresponding to one ATF DR revolution period. Figure 5.25 shows an example of such files where the stacking of all the periods for one file is given. One can clearly see that in addition to the Compton peak a small signal satellite spaced by 462 ns is present. With the “MightyLaser” experimental setup this is not possible because the electron bunch can not interact with laser pulses on two consecutive turns. Such turn-by-turn background should be investigated in the future. To enforce high purity data, the files with such background are rejected.

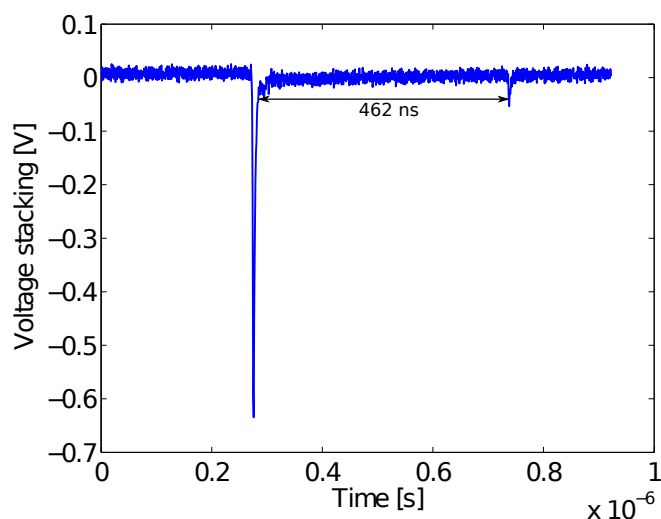


Figure 5.25: Example of the data file having the turn by turn background - Stacking of all the periods belonging to a data file rejected because of turn-by-turn background. Two signal peaks spaced by 462 ns are visible below the noise level.

Approximately half of the data taken and presented in this study have been rejected after the different quality cuts have been applied. All the results commented below are based on high quality data sample.

5.6.4 Laser power stored in the FPC

During the data taking, the average power stored in the FPC was approximately 160 W in average. It was measured by a photodiode placed behind one of the mirrors of the FPC and calibrated with a power-meter. A typical waveform taken by the photodiode is illustrated on Fig. 5.26. Due to the limited dynamic range, the photo-

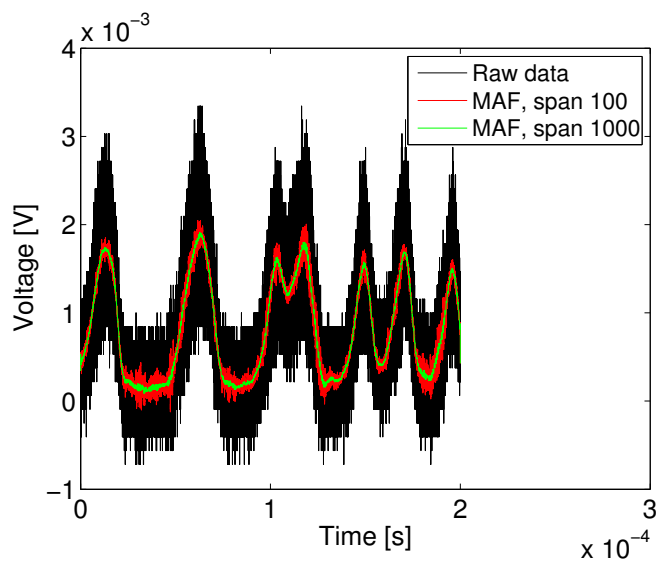


Figure 5.26: Signal waveform of the laser power stored in the FPC - The laser power stored in the FPC is measured by a photodiode placed behind one of the FPC mirrors. The red and green curves correspond to the signal after smoothing with a span of 100 ns and 1000 ns, respectively, has been applied.

diode signal is noisy. These data can be cleaned by applying a smoothing procedure (moving-average filter) with a span value comparable to the FPC time constant (few μs). As one can also see, the FPC laser power experiences oscillations which can be explained by several resonances in the FPC feedback system. For this data taking, the feedback loop used to stabilize the laser power stored in the FPC had not yet been optimized. This optimization has since been done (see Fig. 5.27).

Fig. 5.28a shows the distribution of stored FPC laser power measured by the photodiode during the data taking. The FPC laser power experienced significant fluctuations due to the resonances in the FPC feedback system mentioned above. In Fig. 5.28b a strong correlation between the laser power and the peak height distribution is clearly observed.

5. EXPERIMENT: MIGHTYLASER AT KEK

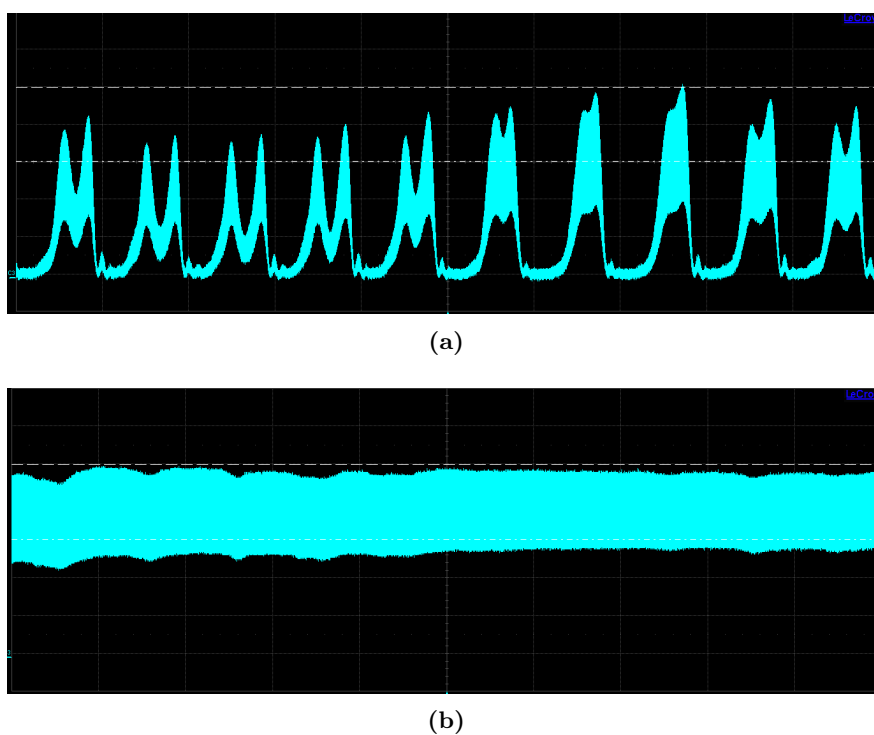


Figure 5.27: Illustration of the laser power stored in the FPC - The duration of the waveforms is 0.5 ms ($50\mu\text{m}$ per division) and the vertical scale is 100 mV per division. Fig. 5.27a shows a typical distribution of laser power during our data takings. The resonances at 20 kHz and 40 kHz are visible. Fig. 5.27b shows the distribution of the laser power after additional filters in the FPC feedback system have been applied (resonances vanish completely).

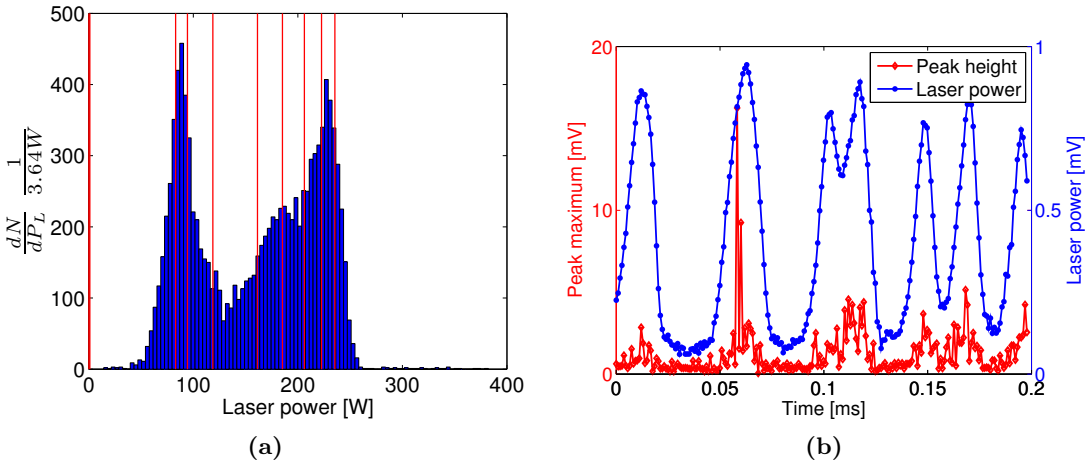


Figure 5.28: Distribution of the laser power stored in the FPC - Fig. 5.28a shows the histogram of the laser power stored in the FPC. Red vertical lines divide the distribution into nine laser power bins of approximately the same population each (see section 5.6.5). Fig. 5.28b gives an example of the correlation between the transmitted FPC laser power and the gamma ray production intensity for a typical data file. This correlation can be seen by the correspondence between the peak height distribution (red line) and the laser power measured by the photodiode at the same time (blue line).

5. EXPERIMENT: MIGHTYLASER AT KEK

5.6.5 Results and discussion

A data analysis was performed to evaluate the number of gamma rays produced during the collisions between the electrons and laser photons.

A spectrum of the gamma rays is shown in Fig. 5.29. It represents the distribution of the energy deposited in the calorimeter expressed by the peak integrals¹.

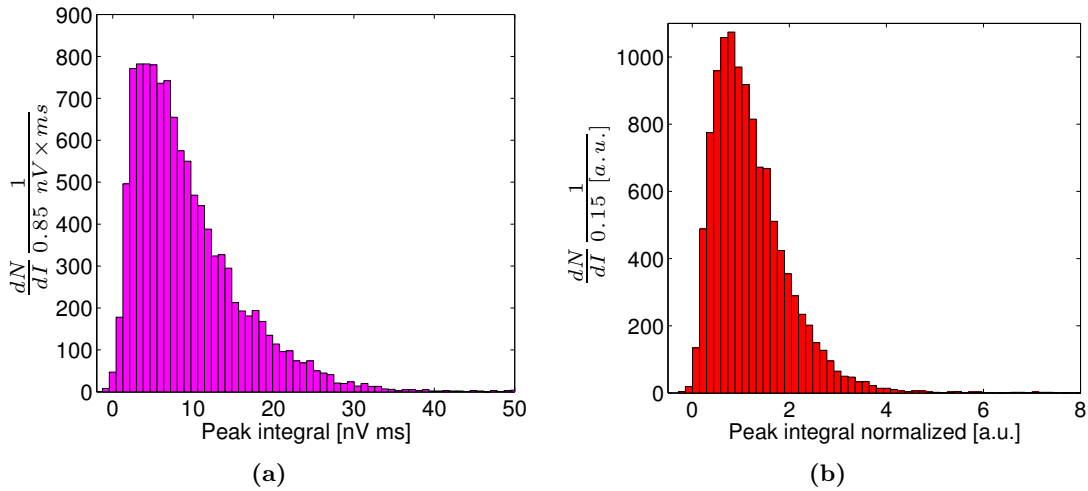


Figure 5.29: Spectrum of the gamma rays produced for all laser powers - Fig. 5.29a shows the distribution of the integrals of the Compton peaks for the high quality data sample whereas the Fig. 5.29b shows the same spectrum normalized by the laser power.

Using our calibration, we can estimate the average number of scattered gammas per bunch crossing. As it was shown in Section 5.4, the mean energy of scattered gamma rays we simulate is 24 MeV. The average energy deposited per bunch crossing (see Eq. 5.1) is 65.1 ± 4.9 MeV and 63.8 ± 4.6 MeV when the Compton peak integral and Compton peak height variables are used respectively. Therefore, we deduce that approximately 2.7 ± 0.2 gamma rays are produced in average per bunch crossing in both cases (for an average laser power stored in the FPC of about 160 W). This rate of about 2.7 gamma rays per bunch crossing was successfully sustained over 6 hours until the end of our run. For the given collision repetition frequency in the ATF DR

¹Similar spectra could be obtained by using the Compton peak height as a measure of energy deposited in the calorimeter.

of about 1 MHz, the flux of gamma rays achieved is about 3×10^6 gammas per second (this does not take into account the 0.75 duty cycle of the ATF).

To verify the linearity of the gamma ray flux as a function of the laser power stored in the FPC, we took data over a wide range of laser power (see Section 5.6.4). The laser power distribution has been split into nine bins of approximately 1300 events each as it is shown on figure 5.28a. Then, the gamma production has been studied within each laser power bin. Spectra of scattered gamma rays which correspond to the different values of laser power stored in the FPC are presented in Fig. 5.30a. As expected, the average of the peak integral distribution (energy deposited in the calorimeter by the gamma rays) scales linearly with the laser power stored in the FPC (see figure 5.30b).

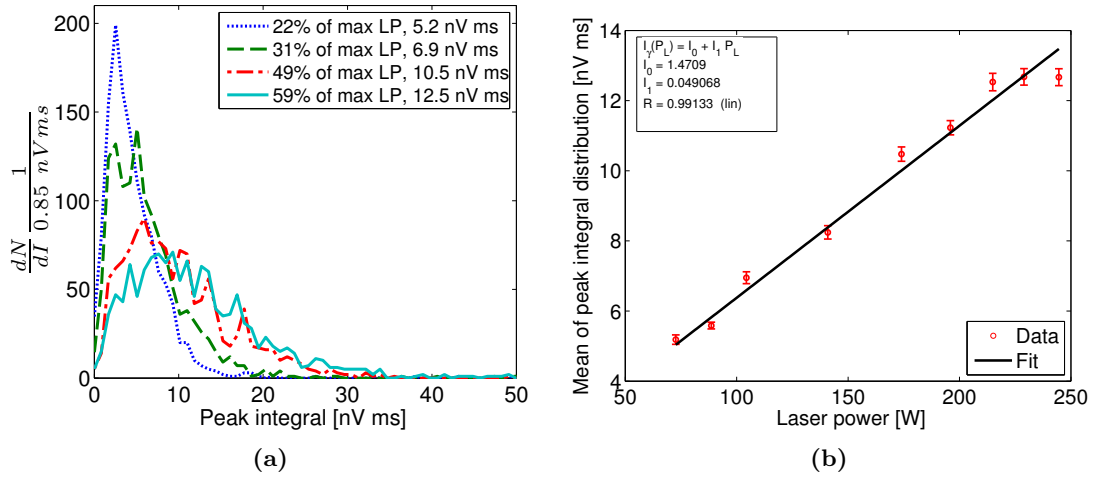


Figure 5.30: Gamma ray spectrum for different FPC stored laser power - Fig. 5.30a presents gamma ray spectrum for different FPC stored laser power. Different colors correspond to the spectra taken at different FPC powers. In the legend, the fraction of the maximum FPC stored power and the mean of each of these spectra are shown. Fig. 5.30b shows the linear relation between the mean of gamma spectra for each laser power bin and the correspondent laser power which is defined as a mean of the laser power bins shown on Fig. 5.28a. The errors bars indicate the statistical errors.

Multibunch data. On one shift, the possibility to record the data during the multi-bunch ATF operation (one train of six bunches Fig. 5.31a) was given. Only a few waveforms were acquired. An example of such data can be seen in Fig. 5.31b, where it is possible to appreciate the presence of pile-up between the bunches in the train as

5. EXPERIMENT: MIGHTYLASER AT KEK

well as a strong contribution from the electronics response. The difference between the

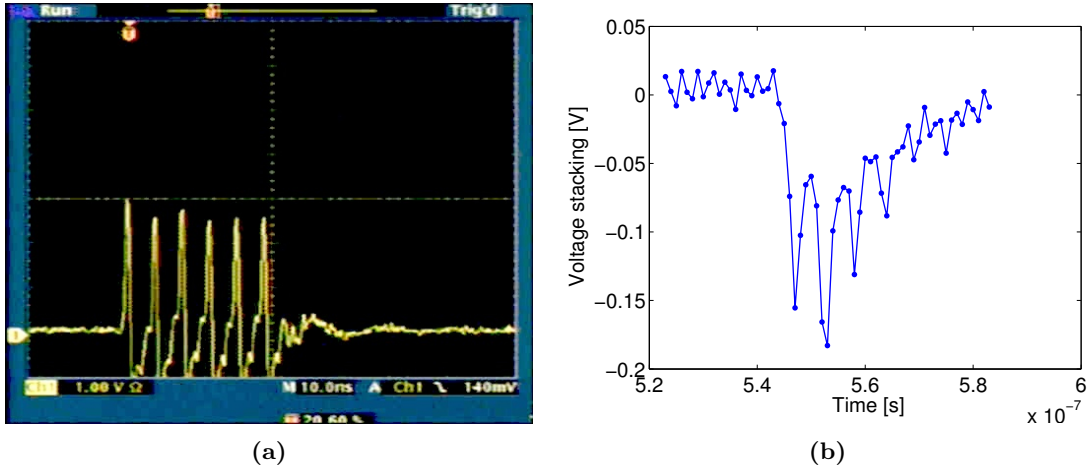


Figure 5.31: Illustration of the data taken during the multibunch ATF run - Fig. 5.31a shows a waveform of the WCM corresponding to the six bunches stored in the ATF DR. Fig. 5.31b shows the stacking for all the periods in the data file acquired during such operation.

intensity of the first and the second peak can be explained by the residual scintillation in the crystal coming from the slow component. The decrease in the intensity after the second peak may be explained by saturation of the PMT leading to a reduced gain.

Unfortunately, we did not have enough data to investigate these issues and to perform a full comprehensive analysis. However, the factors which can contribute to the shape of the signal detected are the following:

- Intrinsic resolution of the crystal (scintillation emission time);
- Transfer resolution (light propagation time in scintillator);
- PMT contribution (transit time of the photoelectrons, anode output circuit);
- DAQ system (bandwidth and sampling rate).

Since the emission time of BaF₂ crystal and the light propagation time in the crystal should not be an issue, possible PMT saturation due to the high amount of light produced can happen. Then, the PMT electronics is perhaps not optimized to capture the signal at high rate. Therefore, for the next data takings one needs to introduce

an optical attenuator installation and optimize the PMT voltage divider circuit for the intense light pulses and the high count rates.

Highest integrated/instantaneous flux. We scanned our data for the best integrated and instantaneous gamma flux which was produced. The best instantaneous flux we measured (the highest energy deposition) was 34 mV which according to the calibration corresponds to 904 ± 65 MeV deposited in the calorimeter. Assuming 24 MeV per gamma ray, this gives about 38 ± 3 gammas produced per bunch crossing. The corresponding Compton peak can be seen on figure 5.32. For the applications of ac-

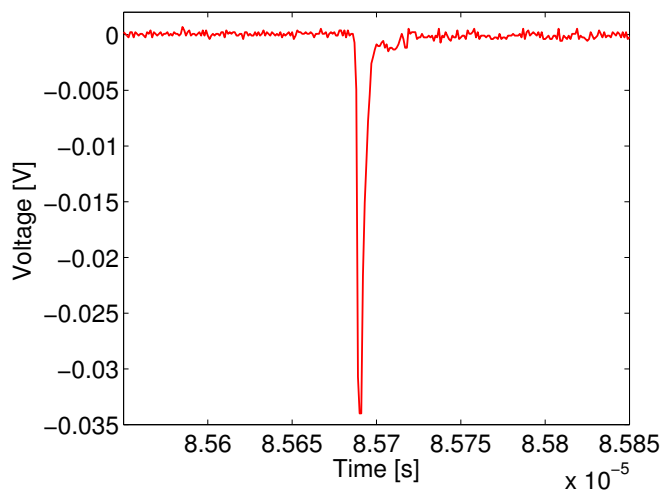


Figure 5.32: Part of the data file containing the highest energy deposited in the calorimeter per one shot which is about 904 MeV - Waveform shows this event which stands for the highest instantaneous gamma flux we measured. It is equivalent to 38 gammas produced in one bunch crossing.

celerator driven Compton sources an important characteristic is the total gamma flux. Table 5.4 summarizes the results concerning the highest gamma ray flux integrated over 0.2 ms (duration of one data file) for different ATF DR filling modes.

As one can see, the total flux does not scale linearly with the number of electron bunches stored in the DR contrary to what was expected. Additional studies should be conducted to investigate this issue. Among the possible reasons can be that there is a small phase shift between the different train at injections and this results in a decrease of the luminosity of the Compton collisions.

Figure 5.33 shows the three data files having the best integrated gamma ray flux.

5. EXPERIMENT: MIGHTYLASER AT KEK

Table 5.4: Highest integrated gamma ray flux achieved.

Electron pulse structure	Total intensity over 0.2 ms	Energy deposited over 0.2 ms	Integrated flux over 0.2 ms	Integrated flux over 1 s	Systematic error
1 train	893 mV	23750 MeV	990 γ	$\sim 4.9 \times 10^6 \gamma$	7%
2 trains	910 mV	24210 MeV	1010 γ	$\sim 5.0 \times 10^6 \gamma$	7%
3 trains	1010 mV	26800 MeV	1120 γ	$\sim 5.6 \times 10^6 \gamma$	7%

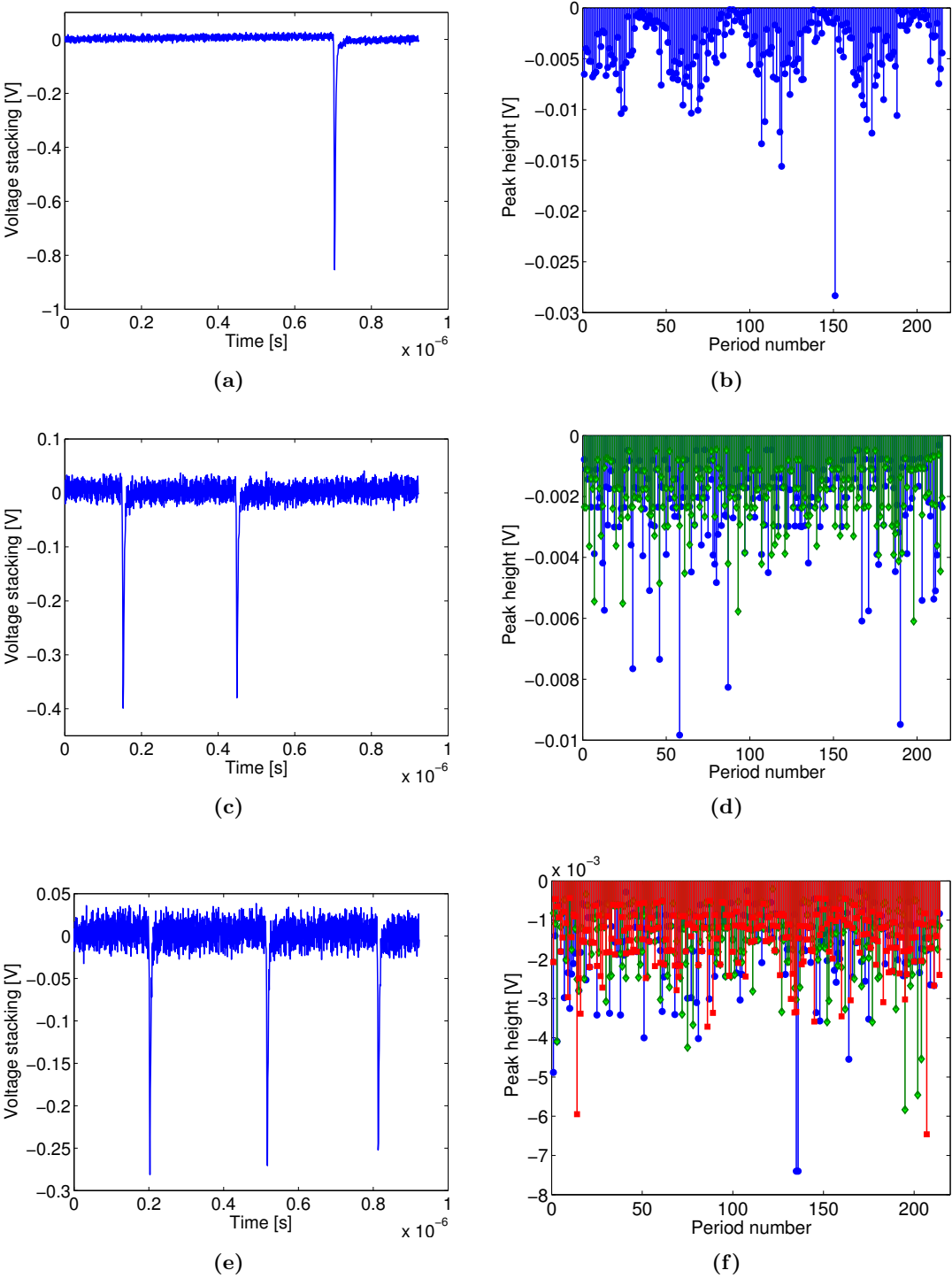


Figure 5.33: Illustration of three data files containing the highest integrated flux over 0.2 ms for different ATF DR filling modes: one bunch stored in the DR (a, b), two trains of one bunch each stored in the DR (c, d) and three trains of one bunch each stored in the DR (e, f). The stacking of all the periods for a given file are shown to the left (a, c, e) while the corresponding peak height distributions are shown to the right (b, d, f). Different colors on figures (d, f) label the gamma ray production from the different trains stored in the ATF DR.

5. EXPERIMENT: MIGHTYLASER AT KEK

5.6.6 Data - simulations comparison

Simulations were carried out to have a comparison with the gamma ray spectrum obtained experimentally. For this, the output of Geant4 simulations (set of the events) is saved into a ROOT file. After that, different events corresponding to one gamma ray each were combined using Poisson statistics to reproduce the multiplicity of the Compton collisions we expected during the experiment (see Fig. 5.34a). Noise measured in the experiment was introduced in the simulations and an optical photon spectrum was obtained. In order to compare this spectrum with those obtained experimentally, the number of optical photons must be converted to the PMT output voltage. For this, Eq. 5.3 can be used to calculate the total charge at the PMT anode Q_{anode} .

$$Q_{anode} = Y_{fast} \times T_{filter} \times QE \times CE \times G \times C_e \quad (5.3)$$

In Eq. 5.3, Y_{fast} is the fraction of the fast component in the total light yield of BaF₂, T_{filter} is the transmittance of the optical filter at the emission maximum, QE and CE are the quantum and charge collection efficiencies of the photocathode respectively, G is the PMT gain and C_e is the electron charge. The quantum and charge collection efficiencies of the photocathode together with the PMT gain have been taken from a data-sheet of the PMT Hamamatsu R3377. From the anode charge the voltage expected during the experiment can be obtained. The corresponding spectrum can be seen in Fig. 5.34b. The quality cuts employed during the data analysis were applied in the same manner for both data and simulations.

At this stage, the simulations can be compared to the measurements. The spectrum of gamma rays measured is shown in Fig. 5.35 together with the spectrum simulated for a mean value of 2.7 gamma rays. The spectrum measured corresponds to the distribution of the energy deposited in the calorimeter expressed by the Compton peak heights.

Figure 5.35 shows a very good agreement between the experimental data and simulations and confirms the production of 2.7 gamma rays per bunch crossing. This good agreement validates the cosmic ray calibration.

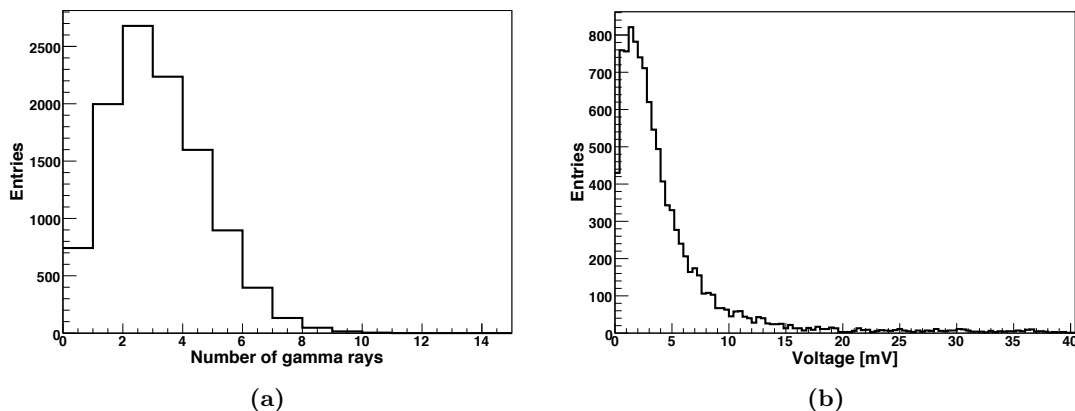


Figure 5.34: Distribution of the number of the optical photons expected in the experiment - Fig. 5.34a shows the simulated distribution of the number of gamma rays produced per bunch crossing owing the Poisson statistics with a mean value of 2.7. Fig. 5.34b shows the distribution of the number of optical photons produced expressed as an anode voltage. Both figures are for 10000 collisions.

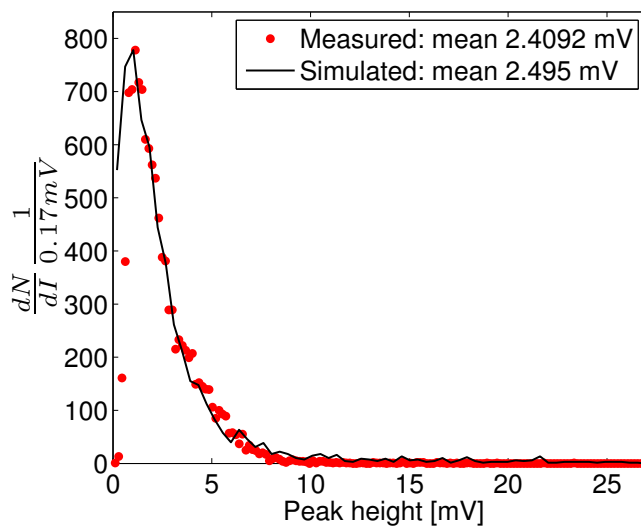


Figure 5.35: Comparison between the measured and simulated energy spectra of the gamma rays resulting from the Compton scattering - The black solid line represents the simulated spectrum and the dots represent the measured gamma ray energy distribution expressed in peak heights. For the simulations the events occur according to a Poisson process with a rate of 2.7 gamma rays per bunch crossing.

5.7 Effect of the Compton scattering on the electron beam dynamics at the ATF DR

During Compton scattering, the electrons transfer part of their kinetic energy to the laser photons, so that both the longitudinal and transverse electron phase space are disturbed. Compton scattering affects parameters like beam lifetime, emittance, energy spread and bunch size. Using Matlab, an investigation of the first order impact of Compton scattering on the ATF beam and of which effects can be easily observed, especially for a high laser power was performed.

5.7.1 Simulation procedure

In the longitudinal phase space (E, τ) , electrons oscillate in longitudinal position and in energy with respect to the synchronous particle (see Section 3.3.1). To find the oscillation amplitudes, a numerical solution of the equations of motion was used in which the energy change δE and time displacement $\delta \tau$ per revolution are given by Eq. 3.48. In the simulation, all the main processes defining the longitudinal beam dynamics have been introduced, that is:

- Synchrotron radiation;
- Energy loss compensation by RF cavities;
- Damping of the oscillation amplitudes;
- Quantum excitation of energy loss;
- Compton scattering.

The program outputs dynamics of the longitudinal phase space by simulating turn by turn electron motion in the $(\delta E, \delta \tau)$ space. It is very difficult to follow the evolution of all the particles in the bunch, therefore a macro-particle approach is used. A number of macro-particles has to be chosen in order to describe properly the dynamics of the electron bunch and to minimize the statistical errors. After different tests to optimize between simulation time and accuracy, the electron bunch has been divided into 10^5 macro-particles.

5.7 Effect of the Compton scattering on the electron beam dynamics at the ATF DR

The Compton scattering effect is simulated using Eq. 3.45 and Eq. 3.46 to retrieve the probability for a given electron to be scattered by a laser photon. The energy loss due to Compton scattering is calculated then for each macro-particle on a turn by turn basis using a Monte-Carlo technique to decide if a given macro-particle has interacted and how much energy was lost due to Compton scattering. The energy spectrum of scattered gamma rays to be used in the program is obtained by using the simulation code CAIN (see e.g. Fig. 5.8b). A simulation using macro-particles cannot predict the real number of scattered gamma rays but it provides the properties we are interested in (electron bunch length, energy spread, etc.) with quite good precision.

Tables 5.1 and 5.2 summarise the parameters used for the simulations. All the initial distribution were considered to be Gaussian.

5.7.2 Results and discussion

Using this simulation code, the motion of the electrons after injection in the DR was studied. On Fig. 5.36 the turn by turn evolution of the electron bunch injected into the DR bucket is shown as well as the boundary of the bucket (separatrix) [107]. When the energy kick for an electron δE brings it beyond the separatrix, the electron is ejected from the bunch and eventually lost. The maximum electron energy offset in ATF DR to stay inside a separatrix (or ATF bucket height) has been calculated to be $(\delta E/E_e)_{max} = 0.012$.

One can see on Fig. 5.36a and also in Fig. 5.37b and Fig. 5.37c the effect of bunch mismatching inside the bucket. The injected bunch is shorter than the RF bucket but has a large energy spread, therefore, under the influence of the RF field it rotates in the longitudinal phase space (see Fig. 5.36a, 5.36b, 5.36c, 5.36d). As the electron bunch is mismatched, it filamentates (see Fig. 5.36e): the electrons spread out in the phase space and evolve into a spiral bounded by the separatrix. After $\sim 10^3$ turns the bunch fills the RF bucket and the damping process dominates. After $\sim 2 \times 10^5$ turns (~ 90 ms) the equilibrium between quantum excitation and damping is reached. However, this equilibrium is modified by Compton scattering (see Fig. 5.36f, 5.36g, 5.36h and Fig. 5.37, the scattered electrons are tagged in black).

In the absence of Compton scattering, at equilibrium all electrons remain within the separatrix. The bucket height is ~ 15 MeV, so Compton scattering with low energy transfer will displace the electrons within the separatrix (see Fig. 5.36f). Whereas larger

5. EXPERIMENT: MIGHTYLASER AT KEK

perturbations such as Compton Scattering with high energy transfer ($\Delta E > 15$ MeV) will kick some electrons out of the bucket resulting in their loss (see Fig. 5.36g).

The evolution of the number of macro-particles, the energy spread and the bunch length are presented on Fig. 5.37a, Fig. 5.37b and Fig. 5.37c respectively. If the laser power is below 100 kW, the effect of Compton scattering is quite small over $\sim 2 \times 10^6$ turns (1 s). For more than 100 kW laser power the equilibrium longitudinal emittance is modified.

For a laser power of 100 kW and 1MW the equilibrium bunch length and the energy spread are respectively $\tau_e = 21$ ps, $\epsilon = 0.06$ % and $\tau_e = 34$ ps, $\epsilon = 0.1$ %. Fig. 5.37a shows that for 1 MW of laser power, the electron loss rate is significantly increased. Table 5.5 summarizes the results obtained and compares them to the available data from the ATF DR. As one can see the ATF data are reproduced well by the simulations of the longitudinal beam dynamics without Compton scattering. This can be considered as a validation of the simulation code.

Table 5.5: Results of the longitudinal beam dynamics simulation of the ATF DR.

Property	Initial	Equilibr w/o Compton	ATF data	Equilibr w Compton (100 kW/1 MW)
Energy spread	0.34 %	0.055 %	0.056 %	0.060 % / 0.092%
Bunch length	25 ps	18.4 ps	18.7 ps	20.6 ps / 33.8 ps

The main effect of Compton Scattering on the ATF beam is a reduction of its lifetime. This could be observed in our setup by monitoring the evolution of the current in the DR over several seconds. For a laser power below 100 kW, the Compton effect on the electron beam dynamics at the ATF DR are rather small which makes them difficult to observe. For high enough laser power bunch lengthening could be observed using a streak camera. As for the energy spread measurements, these would be difficult to perform since it can be measured on a screen at a dispersive region in the ATF2 extraction line only with a poor resolution.

5.7 Effect of the Compton scattering on the electron beam dynamics at the ATF DR

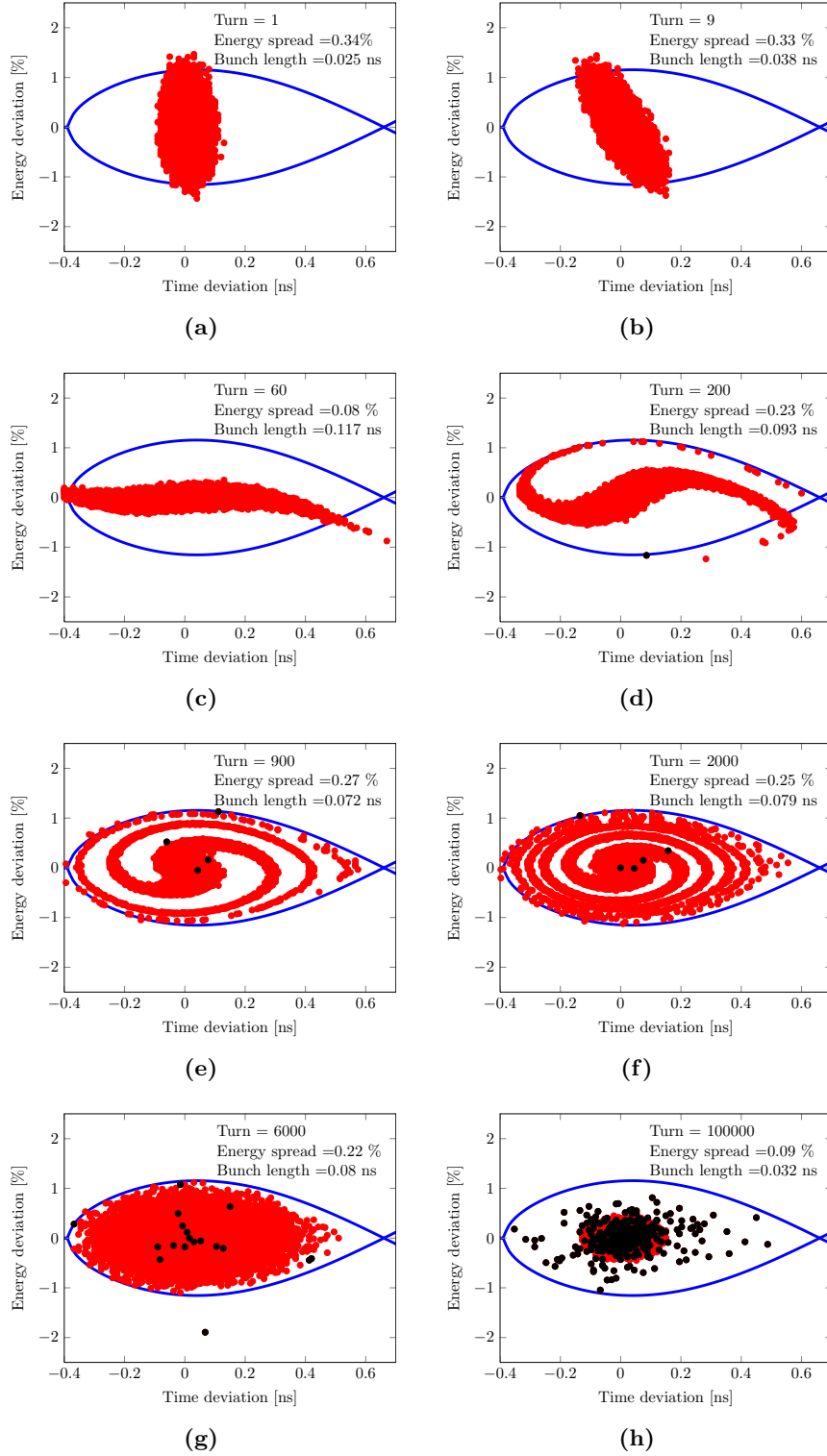


Figure 5.36: Evolution of the longitudinal phase space of one electron bunch at the ATF DR with Compton scattering - The bunch is modeled by 10^5 macro-particles and the laser power is 100 kW. The blue curve defines the separatrix. Macro-particles denoted in black underwent Compton scattering at least once.

5. EXPERIMENT: MIGHTYLASER AT KEK

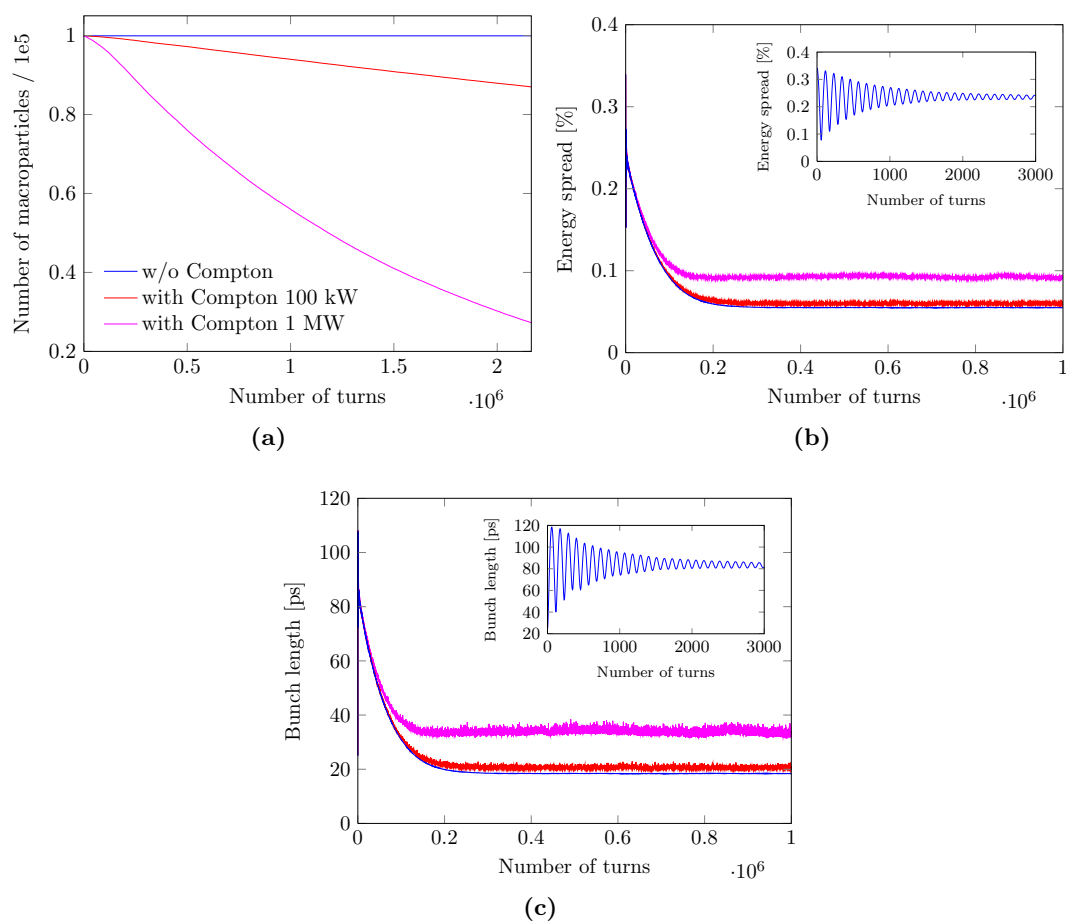


Figure 5.37: Results of the longitudinal beam dynamics simulations of the ATF DR - Fig. 5.37a shows the evolution of the number of macro-particles for different laser power over 1 second. Fig. 5.37b shows the evolution of the energy spread for different laser powers, while Fig. 5.37c shows the evolution of the bunch length for different laser powers, both over approximately 0.5 second. The damping period corresponds to $\sim 2 \times 10^5$ turns (90 ms) after which the equilibrium is reached.

5.8 Perspectives

The experimental results discussed in this Chapter have been obtained during the first “MightyLaser” experimental campaign in 2010. During that time we were learning and gaining experience in FPC operation, understanding the detection, DAQ systems and diagnostics available at the ATF. Therefore these data are statistically limited.

The result obtained shows the production of 2.7 gamma rays per bunch crossing ($\sim 5.6 \times 10^6$ gamma rays per second). However, it is limited by the FPC laser power obtained so far. Work to improve the laser stability and increase the FPC finesse has been interrupted by the earthquake which hit Japan in March 2011. At present, the laser power fluctuation problem seems to be solved, a more powerful laser amplifier has been built and mirrors with higher finesses have been produced. The objective of the next campaign is to increase the rate of production of high energy gamma rays by several orders of magnitude. The increase of the laser power will lead to the production of a large number of high energy gamma rays and we will need to have a PMT capable of sustaining such high current. Therefore work to upgrade the PMT needs to be done. According to our experience, the acquisition of data in multibunch regime will require studies on the optical attenuator and the PMT voltage divider circuit.

Since our last data taking run, a lot of improvements have been done to optimize the data taking process. In this context, the vertical and horizontal position scans have been automatized and for the next data taking it will be more performant and will take much less time. Up to now all the analysis discussed here have been done offline whereas for the next data taking runs, the routine is already optimized to perform online data processing. This is also very important for the position scan since it will allow finding the collision area very quickly.

The DAQ system has been upgraded. A model of the signal measured after the PMT has been developed. This is used to study the effect of limited bandwidth, sampling rate and ADC resolution to specify a faster and more accurate DAQ system. A new oscilloscope LeCroy WaveRunner 610Zi (10 GS/s, 1 GHz bandwidth) has been bought. It has also the advantage of working in segmented acquisition mode allowing us to acquire data every few DR turns over the full duration of an ATF DR storage, significantly increasing the statistics of the data.

5. EXPERIMENT: MIGHTYLASER AT KEK

The longitudinal beam dynamics studies performed show that interesting effects caused by Compton scattering could be observed. During the next runs, we could observe the effect of Compton scattering by monitoring the beam losses (beam lifetime) using the DC Current Transformer (DCCT) and WCM while operating the DR in a storage mode. For higher laser power stored in the FPC, the electron bunch length and size could be monitored by the streak camera and the X-ray synchrotron radiation monitor.

6

Conclusion

The High Energy Physics community is, at present, extremely excited for the probable Higgs boson discovery. After this a new phase of the LHC operation will look for New Physics exploring the energy frontier. At the same time there is a large consensus indicating the future lepton linear collider as the next international facility for the fundamental high energy physics. This is based on a strong physics case concerning a Higgs factory scenario and different channels to search for New Physics. In this framework the interest in colliding both polarised electron and positrons beams has been proven.

To fulfill this requirement, a long period of design studies and R&D have been worked out in many large research laboratories. All these activities have produced two different proposals for a future linear collider: the ILC and the CLIC. The former is based on a high energy cold linac made of the L-band superconductive cavities at 1.3 GHz. The second one is envisaging an innovative scheme of two beams acceleration. A high current linac is playing a role of a “relativistic klystron”, feeding the X-band accelerating structures at 12 GHz. Both projects share a general design scheme based on a sequence of the systems given by the sources, the first accelerating linac injecting the beams in a Damping Ring (DR), a long accelerating linac to bring the beam to the nominal collision energy and a final focus line providing nanometric size beams in the Interaction Point (IP).

In this thesis we identified the positrons source as one of the key elements of the linear collider systems. Due to the large 6D production emittance and to the important thermal and thermo-mechanical stresses in the production target, the positron source

6. CONCLUSION

characteristics fix many of the collider parameters such as the repetition frequency, the bunch and the train current and so the final luminosity.

The basic aspects of the polarised positron source have been illustrated. First of all a full review of the polarization definitions and theory has been provided. The different proposed schemes for the polarised positron sources of the future linear collider projects have been analysed taking into account the ILC and CLIC baseline and the alternative solutions. A particular attention has been given to the solution where the gamma ray flux, to produce the positrons, is provided by colliding an intense electron beam with high power laser pulses. In this case, Compton scattering boosts the energy of the laser photons giving the gamma ray the required energy. The weak point of this scheme is the low Compton scattering cross section to produce the gamma rays. Therefore, a study to explore the possibility of using a multiple collision point line integrated in the ERL has been carried out. The results reveal that increasing the number of IPs, an important loss of the efficiency is obtained, especially, when a tight angular selection is required to provide the acceptable degree of polarisation. For the configuration proposed, employing the 5 IP line with two crossing lasers per IP, a gain factor of ~ 4 has been observed. The results obtained can be easily extended for the other schemes based on a Compton Ring or on a Compton Linac.

The Compton source in the Ring configuration has been studied by evaluating the equilibrium energy spread given by both the synchrotron damping and the Compton quantum excitations. An original contribution was to evaluate the Compton regime dynamics by applying the Campbell theorem. This method allows easily to be extended to the polarised beams by only introducing the Compton scattering cross section. The results obtained are in good agreement with the ones given by the other methods.

To highlight the importance of the Compton facilities, not only in the framework of the polarised positron sources, a short overview on the different applications fields have been provided. Depending on the energy of the electron beam it is possible to envisage a large domain of applications such as the crystallography, the medicine, the cultural heritage preservation, the material science, the Nuclear Physics and the nuclear waste treatment.

The system of production and capture of the positrons has been studied and characterised in the CLIC case. In this context, the limits of the adiabatic matching device have been pointed out. The global longitudinal and transverse acceptances have

been estimated by simulating the positron production and by tracking the positrons in the accelerating capture system. After this, a final estimation of the impact on the global linear collider polarised positron source efficiency have been provided. This parametrization allowed to individuate the technologies to be improved in the future to demonstrate the feasibility of such a source for the future linear collider.

The last Chapter was dedicated to the experimental activity carried out in the framework of the “MightyLaser” experiment at the ATF KEK. A high gain passive optical resonator has been coupled with a high power laser and installed in a line of the ATF ring. The resonator is a non-planar four mirror Fabry-Perot cavity which allows a minimum waist of the cavity mode at the Compton IP and provides the circularly polarized fundamental eigenmodes. This allowed to have the first test of a high gain resonator in an accelerator environment testing the vacuum integration and the synchronization systems.

Taking into account the nominal parameters of the Fabry-Perot cavity and the electron ring, it was possible to evaluate the expected gamma ray flux and the spectrum to be measured. A detailed analysis of the possible errors given by the geometrical-temporal misalignments of the electron beam and the laser pulses in the IP was carried out. The experimental set-up was fully characterised by both Monte-Carlo simulations and the cosmic ray calibration. At the end, the data analysis demonstrates that it was possible to synchronize two beams and to produce the gamma rays by Compton collisions.

The method and the experimental cuts applied in the analysis were motivated. An average of 2.7 ± 0.2 with a peak of 38 ± 3 gamma rays per crossing and the highest integrated flux of 1120 ± 80 gamma rays over 0.2 ms ($\sim 5.6 \times 10^6$ gamma rays per second) was measured. The variation of the detected flux was justified by the laser power fluctuations given by the unstable coupling between the laser and the optical resonator. This problem has been solved meanwhile but at present it was not possible to have another experimental campaign mainly due to the earthquake that struck Japan.

In addition, the effects of the Compton collisions on the longitudinal beam dynamics in the ATF ring have been evaluated. We conclude that a higher laser power is needed to produce the measurable effects on the equilibrium longitudinal emittance to be detected by measuring the electron bunch length. During the next experimental runs, we should

6. CONCLUSION

observe the effect of Compton scattering by monitoring the beam losses while operating the ATF DR in a storage mode.

The future developments and the R&D directions, in our opinion, should be concentrated on mainly three topics:

- It will be important to pursue the technological R&D on high power laser systems and the optical cavities or the optical recirculators. This must target a regime where the circulating laser pulse has a very important energy in the order of 1 J. In this framework, it is very interesting to follow the research conducted in the context of the ELI-NP facility (constructed in Romania) in which a new technology of the laser recirculation are studied.
- At the same time it is important to pursue the studies on the electron beam stability in the Compton rings and the technological R&D to design an extremely challenging ERL accelerators with a current in the Amperes domain. This has to be explored by taking into account the configuration with a low repetition frequency (few tens of MHz) and high charge per bunch. ERL is at present a developing field due also to their application as the light sources. Unfortunately, at the moment, there is no an experimental programme envisaging measuring the beam dynamics under a strong Compton regime in the storage ring.
- The last topic concerns a possibility of producing and shaping the positron bunch to allow a continuous injection stacking in order to increase the charge per bunch in the DR. Fast multibunch injection is a very challenging experiment which interest, in the context of the future linear collider positron sources, is certain independently from the polarisation.

Exploring all these topics is not only a very important step in the framework of the future linear collider, but it represents also an amazing challenge in many aspects of the accelerator physics that can lead to very important applications in many applied physics fields.

References

- [1] R. AβMANN, M. LAMONT, AND S. MYERS. **A brief history of the LEP collider.** *Nuclear Physics B-Proceedings Supplements*, **109**(2):17–31, 2002. 2
- [2] A.P. BLONDEL, F. ZIMMERMANN, M. KORATZINOS, AND M ZANETTI. **LEP3: A High Luminosity e+ e- Collider in the LHC Tunnel to Study the Higgs Boson.** In *Proc. International Particle Accelerator Conference, New Orleans, Louisiana, USA*, page TUPPR078. IEEE, 2012. 2
- [3] R W AβMANN, J BADIER, A BLONDEL, M BGE, M CROZON, BERND DEHNING, H GROTE, JEAN-PIERRE KOUTCHOUK, MASSIMO PLACIDI, R SCHMIDT, F SONNEMANN, F A TECKER, AND J WENNINGER. **Spin dynamics in LEP with 40-100 GeV beams.** *AIP Conf. Proc.*, **570**:169–178, 2000. 2
- [4] L. LINSSEN, A. MIYAMOTO, M. STANITZKI, AND H. WEERTS. **Physics and Detectors at CLIC: CLIC Conceptual Design Report.** *arXiv preprint arXiv:1202.5940*, 2012. 2
- [5] A. DJOUADI, J. LYKKEN, K. MÖNIG, Y. OKADA, M. OREGLIA, AND S. YAMASHITA. **International linear collider reference design report volume 2: physics at the ILC.** *arXiv preprint arXiv:0709.1893*, 2007. 2, 70
- [6] G. MOORTGAT-PICK, T. ABE, G. ALEXANDER, B. ANANTHANARAYAN, A.A. BABICH, V. BHARADWAJ, D. BARBER, A. BARTL, A. BRACHMANN, S. CHEN, ET AL. **Polarized positrons and electrons at the linear collider.** *Physics Reports*, **460**(4):131–243, 2008. 2, 3, 4, 5, 18
- [7] G. AAD, T. ABAJYAN, B. ABBOTT, J. ABDALLAH, S. ABDEL KHALEK, AA ABDELALIM, O. ABDINOV, R. ABEN, B. ABI, M. ABOLINS, ET AL. **Ob-**

REFERENCES

- ervation of a new particle in the search for the Standard Model Higgs boson with the ATLAS detector at the LHC. *Physics Letters B*, 2012. 2
- [8] S. CHATRCHYAN, V. KHACHATRYAN, AM SIRUNYAN, A. TUMASYAN, W. ADAM, E. AGUILO, T. BERGAUER, M. DRAGICEVIC, J. ERÖ, C. FABJAN, ET AL. **Observation of a new boson at a mass of 125 GeV with the CMS experiment at the LHC.** *Physics Letters B*, 2012. 2
- [9] J.E. BRAUA, R.M. GODBOLEB, F.R. LE DIBERDERC, MA THOMSOND, H. WEERTSE, G. WEIGLEINF, J.D. WELLSG, AND H. YAMAMOTOH. **The Physics Case for an e+e- Linear Collider.** *arXiv preprint arXiv:1210.0202*, 2012. 2, 3, 6
- [10] N. PHINNEY. **ILC reference design report: Accelerator executive summary.** *ICFA Beam Dyn. Newslett. 42: 7-29, 2007*, **42**(SLAC-PUB-13044), 2007. 2, 9, 25
- [11] **International Linear Collider Submission to European Strategy Discussion. Summary of the Technical Design Report for the ILC.** Technical report, ILC ESD-2012/2, 2012. 2, 9
- [12] CLIC COLLABORATION. **A multi-TeV linear collider based on CLIC technology. CLIC Conceptual Design Report.** 2012. 2, 7, 8, 21, 70, 82, 84, 85
- [13] P LEBRUN ET AL. **The CLIC Programme: Towards a Staged e^+e^- Linear Collider Exploring the Terascale: CLIC Conceptual Design Report.** Technical Report arXiv:1209.2543. CERN-2012-005. ANL-HEP-TR-12-51. KEK-Report-2012-2., Geneva, Sep 2012. 3
- [14] P.C. ROWSON, DONG SU, AND STEPHANE WILLOCQ. **Highlights of the SLD physics program at the SLAC linear collider.** *Ann.Rev.Nucl.Part.Sci.*, **51**:345–412, 2001. 4
- [15] J.L. ABELLEIRA FERNANDEZ ET AL. **A Large Hadron Electron Collider at CERN: Report on the Physics and Design Concepts for Machine and Detector.** *J.Phys.*, **G39**:075001, 2012. 8

-
- [16] P.A.M. DIRAC. **The quantum theory of the electron.** *Proceedings of the Royal Society of London. Series A, Containing Papers of a Mathematical and Physical Character*, **117**(778):610–624, 1928. 11
- [17] P.A.M. DIRAC. **A theory of electrons and protons.** *Proceedings of the Royal Society of London. Series A, Containing Papers of a Mathematical and Physical Character*, **126**(801):360–365, 1930. 11
- [18] F.E. CLOSE. *Antimatter.* Oxford University Press, USA, 2009. 11
- [19] C.D. ANDERSON AND S.H. NEDDERMEYER. *The production and properties of positrons.* PA Norstedt & söner, 1937. 11, 12
- [20] C.D. ANDERSON. **The positive electron.** *Physical Review*, **43**(6):491, 1933. 11
- [21] I. JOLIOT-CURIE. **Nobel Lecture: Artificial Production of Radioactive Elements**, 1935. 12
- [22] P.J. GILMER. **Irène Joliot-Curie, a Nobel laureate in artificial radioactivity.** *Celebrating the 100th anniversary of Madame Marie Sklodowska Curies Nobel Prize in Chemistry*, pages 41–57, 2011. 12
- [23] J.D. JACKSON. *Classical electrodynamics.* New York: John Wiley & Sons, Inc., third edition, 1999. 13, 31
- [24] G. STOKES. **Trans. Cambridge Phil. Soc.** *vol*, **9**:309, 1852. 13
- [25] G. STOKES ET AL. *Mathematical and physical papers.* 1901. 13
- [26] H. A. TOLHOEK. **Electron polarization, theory and experiment.** *Reviews of modern physics*, **28**(3):277–298, 1956. 15
- [27] M.E. ROSE. *Relativistic electron theory.* New York: John Wiley & Sons, Inc., 1961. 15
- [28] U. FANO. **Description of states in quantum mechanics by density matrix and operator techniques.** *Reviews of Modern Physics*, **29**(1):74–93, 1957. 15

REFERENCES

- [29] R.W. SCHMIEDER. **Stokes-algebra formalism.** *JOSA*, **59**(3):297–302, 1969. 15
- [30] W.H. MCMASTER. **Matrix representation of polarization.** *Reviews of Modern Physics*, **33**(1):8–27, 1961. 15
- [31] EUGENE P. WIGNER. **Relativistic Invariance and Quantum Phenomena.** *Rev. Mod. Phys.*, **29**:255–268, Jul 1957. 17
- [32] J.M. JAUCH AND F. ROHRLICH. *The theory of photons and electrons.* 1959. 17
- [33] E.L. GARWIN, D.T. PIERCE, AND H.C. SIEGMANN. **Swiss Physical Society Meeting, April 26, 1974.** *Helv. Phys. Acta*, **47**:393, 1974. 18
- [34] G. LAMPEL AND C. WEISBUCH. **Proposal for an efficient source of polarized photoelectrons from semiconductors.** *Solid State Communications*, **16**(7):877 – 880, 1975. 18
- [35] E.L. GARWIN, D.T. PIERCE, AND H.C. SIEGMANN. **Polarized photoelectrons from optically magnetized semiconductors.** Technical report, Stanford Research Inst., Menlo Park, CA (USA); Eidgenoessische Technische Hochschule, Zurich (Switzerland). Lab. fuer Festkoerperphysik, 1975. 18
- [36] C.K. SINCLAIR. **High Intensity Polarized Electron Sources.** In *High-energy physics with polarized beams and polarized targets: proceedings of the 1980 international symposium, Lausanne, September 25-October 1, 1980*, **38**, page 27. Birkhauser, 1981. 18
- [37] T. MARUYAMA, E. L. GARWIN, R. PREPOST, G. H. ZAPALAC, J. S. SMITH, AND J. D. WALKER. **Observation of strain-enhanced electron-spin polarization in photoemission from InGaAs.** *Phys. Rev. Lett.*, **66**:2376–2379, May 1991. 18
- [38] T. OMORI, Y. KURIHARA, T. NAKANISHI, H. AOYAGI, T. BABA, T. FURUYA, K. ITOGA, M. MIZUTA, S. NAKAMURA, Y. TAKEUCHI, M. TSUBATA, AND M. YOSHIOKA. **Large enhancement of polarization observed by extracted electrons from the AlGaAs-GaAs superlattice.** *Phys. Rev. Lett.*, **67**:3294–3297, Dec 1991. 18

-
- [39] R. ALLEY ET AL. **The Stanford linear accelerator polarized electron source.** *Nuclear Instruments and Methods in Physics Research Section A: Accelerators, Spectrometers, Detectors and Associated Equipment*, **365**(1):1 – 27, 1995. 19
- [40] T. MARUYAMA, D.A. LUH, A. BRACHMANN, JE CLENDENIN, E.L. GARWIN, S. HARVEY, J. JIANG, RE KIRBY, CY PRESCOTT, R. PREPOST, ET AL. **Systematic study of polarized electron emission from strained GaAs/GaAsP superlattice photocathodes.** *Applied physics letters*, **85**(13):2640–2642, 2004. 19
- [41] F. ZHOU, A. BRACHMANN, T. MARUYAMA, AND J. C. SHEPPARD. **Polarized Photocathode R&D for Future Linear Colliders.** In *AIP Conference Proceedings*, **1149**, 2009. 19
- [42] M. KUWAHARA, T. MORINO, T. NAKANISHI, S. OKUMI, M. YAMAMOTO, M. MIYAMOTO, N. YAMAMOTO, R. SAKAI, K. TAMAGAKI, A. MANO, ET AL. **Spin-Polarized Electrons Extracted from GaAs Tips using Field Emission.** In *AIP Conference Proceedings*, **915**, pages 1055–1060, 2007. 19
- [43] J.E. CLENDENIN. **High-yield positron systems for linear colliders.** In *Particle Accelerator Conference, 1989. Accelerator Science and Technology., Proceedings of the 1989 IEEE*, pages 1107–1111. IEEE, 1989. 19
- [44] J. DUMAS. *Feasibility studies of a polarized positron source based on the bremsstrahlung of polarized electrons.* PhD thesis, Laboratoire de Physique Subatomique et de Cosmologie, Joseph Fourier University, 2011. 20
- [45] V.E. BALAKIN AND A.A. MIKHAILICHENKO. **Conversion System for Obtaining Highly Polarized Positrons and Electrons at High Energy.** Technical report, Budker INP preprint 79-85, Novosibirsk, 1979. 20, 23
- [46] R. CHEHAB, F. COUCHOT, AR NYAIESH, F. RICHARD, AND X. ARTRU. **Study of a positron source generated by photons from ultrarelativistic channeled particles.** In *Particle Accelerator Conference, 1989. Accelerator Science and Technology., Proceedings of the 1989 IEEE*, pages 283–285. IEEE, 1989. 20

REFERENCES

- [47] P. RULLHUSEN, X. ARTRU, AND P. DHEZ. *Novel radiation sources using relativistic electrons: from infrared to x-rays*, **4**. World Scientific Pub Co Inc, 1998. 21, 41
- [48] X. ARTRU, R. CHEHAB, M. CHEVALLIER, T. KAMITANI, T. OMORI, L. RINOLFI, V.M. STRAKHOVENKO, T. SUWADA, A. VARIOLA, AND A. VIVOLI. **A Positron Source Using Channeling in Crystals for Linear Colliders**. In *Charged and Neutral Particles Channeling Phenomena: Channeling 2008: Proceedings of the 51st Workshop of the INFN ELOISATRON Project*, **30**, page 210. World Scientific Publishing Company, 2010. 21
- [49] E.G. BESSONOV AND A.A. MIKHAILICHENKO. **A Method of Polarized Positron Beam Production**. In *Proceedings of the 5th European Particle Accelerator Conference*, page 1516, 1996. 21
- [50] T. OKUGI, Y. KURIHARA, M. CHIBA, A. ENDO, R. HAMATSU, T. HIROSE, T. KUMITA, T. OMORI, Y. TAKEUCHI, AND M. YOSHIOKA. **Proposed Method to Produce a Highly Polarized e+ Beam for Future Linear Colliders**. *Japanese journal of applied physics*, **35**(part 1):3677–3680, 1996. 21
- [51] T. OMORI. **Polarized positron source for linear colliders**. Presented at the workshop on new kinds of positron sources for Linear Colliders, SLAC, Stanford, California, March, 4-7 Nov 1997. 21, 27
- [52] TSUNEHIKO OMORI, TOHRU TAKAHASHI, SABINE RIEMANN, ET AL. **A conventional positron source for international linear collider**. *Nuclear Instruments and Methods in Physics Research Section A*, **672**(0):52 – 56, 2012. 21
- [53] A.A. SOKOLOV AND I.M. TERNOV. In *Doklady Akad. Nauk SSSR*, **153**, page 1052, 1963. 22
- [54] J. D. JACKSON. **On understanding spin-flip synchrotron radiation and the transverse polarization of electrons in storage rings**. *Rev. Mod. Phys.*, **48**:417–433, Jul 1976. 22

-
- [55] D.P. BARBER. **Theory and Observation of Electron Polarization in High Energy Storage Rings.** In *Proc. of 10th International Symposium on High Energy Spin Physics, Nagoya, Japan*, **10**, 1992. 22
- [56] D. P. BARBER, H.D. BREMER, M. BÖGE, R. BRINKMANN, W. BRÜCKNER, C. BÜSCHER, M. CHAPMAN, K. COULTER, PPJ DELHEIJ, M. DÜREN, ET AL. **The HERA polarimeter and the first observation of electron spin polarization at HERA.** *Nucl. Instrum. Meth*, **A329**(1-2):79–111, 1993. 22, 60
- [57] V. E. BALAKIN AND A. A. MIKHAILICHENKO. **VLEPP: The conversion System for Obtaining Highly Polarized Electrons and Positrons.** . Prepared for 12th International Conference on High-Energy Accelerators, Batavia, Illinois, 11-16 Aug 1983. 23
- [58] A.A. MIKHAILICHENKO. *Conversion System for Obtaining Polarized Electrons and Positrons at High Energy Translation.* PhD thesis, Academy of science USSR, Budker Institute of Nuclear Physics, Novosibirsk, 1986 (translated 2002). 23
- [59] D. F. ALFEROV, YU. A. BASHMAKOV, K. A. BELOVINTSEV, E. G. BESSONOV, AND P. A. CHERENKOV. **Istochniki ondulyatornogo izlucheniya (teoriya, eksperiment, primeneniya).** *Uspekhi Fizicheskikh Nauk*, **128**(5):177–180, 1979. 24
- [60] A.A. MIKHAILICHENKO. **Pulsed Helical Undulator for Test at SLAC Polarized Positron Production Scheme.** 2002. 24
- [61] B.M. KINCAID. **A short-period helical wiggler as an improved source of synchrotron radiation.** *Journal of Applied Physics*, **48**(7):2684–2691, 1977. 24
- [62] K. FLÖTTMANN. *Investigations toward the development of polarized and unpolarized high intensity positron sources for linear colliders.* PhD thesis, Dt. Elektronen-Synchrotron, 1993. 24
- [63] J. C. SHEPPARD. **Helical undulator radiation.** *SLAC LCC-0095, July*, 2002. 24
- [64] G. ALEXANDER ET AL. **Observation of Polarized Positrons from an Undulator-Based Source.** *Physical review letters*, **100**(21):210801, 2008. 25

REFERENCES

- [65] G. ALEXANDER ET AL. **Undulator-Based Production of Polarized Positrons.** *Nucl. Instrum. Meth.*, **A610**:451–487, 2009. 25
- [66] D. J. SCOTT ET AL. **Demonstration of a High-Field Short-Period Superconducting Helical Undulator Suitable for Future TeV-Scale Linear Collider Positron Sources.** *Phys. Rev. Lett.*, **107**:174803, Oct 2011. 26
- [67] J. GRONBERG, C. BROOKSBY, T. PIGGOTT, R. ABBOTT, J. JAVEDANI, AND E. COOK. **Prototyping of the ILC Baseline Positron Target.** *Arxiv preprint arXiv:1203.0070*, 2012. 26
- [68] S. ARAKI, Y. HIGASHI, Y. HONDA, Y. KURIHARA, M. KURIKI, T. OKUGI, T. OMORI, T. TANIGUCHI, N. TERUNUMA, J. URAKAWA, ET AL. **Design of a polarised positron source based on laser compton scattering.** *Arxiv preprint physics/0509016*, 2005. 27
- [69] A. VARIOLA, C. BRUNI, I. CHAIKOVSKA, O. DADOUN, T. OMORI, J. URAKAWA, L. RINOLFI, A. VIVOLI, AND F. ZIMMERMANN. **ERL parameters for Compton polarized positron source.** In *Proceedings of the 23rd Particle Accelerator Conference, Vancouver, Canada*, page MO6RFP068. IEEE, 2009. 28, 30, 53, 54
- [70] F. ZIMMERMANN, Y. PAPAPHILIPPOU, L. RINOLFI, F. ANTONIOU, R. CHEHAB, M. KURIKI, T. OMORI, J. URAKAWA, A. VARIOLA, A. VIVOLI, ET AL. **Stacking Simulations for Compton Positron Sources of Future Linear Colliders.** In *Proceedings of the 23rd Particle Accelerator Conference, Vancouver, Canada*, page MO6RFP068. IEEE, 2009. 28, 84
- [71] V. YAKIMENKO AND I. V. POGORELSKY. **Polarized γ source based on Compton backscattering in a laser cavity.** *Phys. Rev. ST Accel. Beams*, **9**:091001, Sep 2006. 28, 53
- [72] I.V. POGORELSKY AND V.E. YAKIMENKO. **Experimental demonstration of feasibility of a polarized gamma-source for ILC based on compton backscattering inside a CO₂ laser cavity.** In *Particle Accelerator Conference, 2007. PAC. IEEE*, pages 3208–3210. IEEE, 2007. 28

-
- [73] EUGENE BULYAK, PETER GLADKIKH, VLADISLAV SKOMOROKHOV, TSUNEHICO OMORI, JUNJI URAKAWA, KLAUS MOENIG, AND FRANK ZIMMERMANN. **Beam dynamics in Compton ring gamma sources.** *Phys. Rev. ST Accel. Beams*, **9**:094001, Sep 2006. 29, 53, 54
- [74] L. RINOLFI, H.H. BRAUN, Y. PAPAPHILIPPOU, D. SCHULTE, A. VIVOLI, F. ZIMMERMANN, F. ANTONIOU, I.R. BAILEY, L. ZANG, E.V. BULYAK, ET AL. **The CLIC positron sources based on Compton schemes.** In *Proceedings of the 23rd Particle Accelerator Conference, Vancouver, Canada*. IEEE, 2009. 29
- [75] T. HIROSE, K. DOBASHI, Y. KURIHARA, T. MUTO, T. OMORI, T. OKUGI, I. SAKAI, J. URAKAWA, AND M. WASHIO. **Polarized positron source for the linear collider, JLC.** *Nuclear Instruments and Methods in Physics Research Section A: Accelerators, Spectrometers, Detectors and Associated Equipment*, **455**(1):15–24, 2000. 29
- [76] T. OMORI, M. FUKUDA, T. HIROSE, Y. KURIHARA, R. KURODA, M. NOMURA, A. OHASHI, T. OKUGI, K. SAKAUE, T. SAITO, ET AL. **Efficient propagation of polarization from laser photons to positrons through compton scattering and electron-positron pair creation.** *Physical review letters*, **96**(11):114801, 2006. 29
- [77] W. BARLETTA, R. KLANNER, G. KNOLL, AND F. SAULI. **Energy Recovering Linacs 2005, Proceedings of the Beam Dynamics Workshop on Energy Recovering Linacs.** *Nuclear Instruments and Methods in Physics Research Section A: Accelerators, Spectrometers, Detectors and Associated Equipment*, **557**(1), 2006. 30
- [78] H. KOGELNICK AND T. LI. **Laser beams and resonators.** *Appl. Opt.*, **5**:1550–1567, 1966. 30, 95
- [79] J. BONIS ET AL. **Non-planar four-mirror optical cavity for high intensity gamma ray flux production by pulsed laser beam Compton scattering off GeV-electrons.** *Journal of Instrumentation*, **7**:P01017, 2012. 30, 95
- [80] A. H. COMPTON. **A quantum theory of the scattering of X-rays by light elements.** *Physical Review*, **21**(5):483, 1923. 32

REFERENCES

- [81] O. KLEIN AND T. NISHINA. **Über die Streuung von Strahlung durch freie Elektronen nach der neuen relativistischen Quantendynamik von Dirac.** *Zeitschrift für Physik A Hadrons and Nuclei*, **52**(11):853–868, 1929. 32
- [82] M.E. PESKIN AND D.V. SCHROEDER. *An introduction to quantum field theory*, **94**. Westview press, 1995. 34, 35
- [83] V. B. BERESTETSKII, L. D. LANDAU, E. M. LIFSHITZ, L. P. PITAEVSKII, J. B. SYKES, AND J. S. BELL. *Quantum electrodynamics*, **4**. Butterworth-Heinemann, 1982. 35, 39, 43
- [84] V. TELNOV. **Principles of photon colliders.** *Nuclear Instruments and Methods in Physics Research Section A*, **355**(1):3–18, 1995. 43, 44
- [85] C. SUN AND Y.K. WU. **Theoretical and simulation studies of characteristics of a Compton light source.** *Physical Review Special Topics-Accelerators and Beams*, **14**(4):044701, 2011. 47, 62
- [86] I. F. GINZBURG, G. L. KOTKIN, S. L. PANFIL, V. G. SERBO, AND V. I. TELNOV. **Colliding [gamma] e and [gamma][gamma] beams based on single-pass e+ e-accelerators II. Polarization effects, monochromatization improvement.** *Nuclear Instruments and Methods in Physics Research*, **219**(1):5–24, 1984. 47
- [87] E.G. BESSONOV, R.M. FESHCHENKO, M.V. GORBUNOV, A.V. VINOGRADOV, AND V.I. SHVEDUNOV. **Energy losses and efficiency of laser-electron X-ray generator for medical applications.** *Arxiv preprint physics/0405003*, 2004. 49
- [88] A.A. YEE, A. SAVCHENKO, A. IGNACHENKO, J. LUKIN, X. XU, T. SKARINA, E. EVDOKIMOVA, C.S. LIU, A. SEMESI, V. GUIDO, ET AL. **NMR and X-ray crystallography, complementary tools in structural proteomics of small proteins.** *Journal of the American Chemical Society*, **127**(47):16512–16517, 2005. 49
- [89] C. BRUNI, R. CHICHE, R. CIZERON, Y. FEDALA, J. HAISSINSKI, M. JACQUET, D. JEHANNO, M. LACROIX, L. MEIGNIEN, B. MERCIER, ET AL. **ThomX-Conceptual Design Report.** 2009. 49

-
- [90] R. HAJIMA, T. HAYAKAWA, N. KIKUZAWA, AND E. MINEHARA. **Proposal of nondestructive radionuclide assay using a high-flux gamma-ray source and nuclear resonance fluorescence.** *Journal of Nuclear Science and Technology*, **45**(5):441–451, 2008. 50
- [91] C.P.J. BARTY AND F.V. HARTEMANN. **Lawrence Livermore Laboratory Report.** Technical report, UCRL-TR-206825, 2004. 50
- [92] ELI-NUCLEAR PHYSICS WORKING GROUPS. **The White Book of ELI Nuclear Physics.** Reference available at <http://www.eli-np.ro/documents/ELI-NP-WhiteBook.pdf>. 50
- [93] M. COTTE, E. WELCOMME, VA SOLÉ, M. SALOMÉ, M. MENU, P. WALTER, AND J. SUSINI. **Synchrotron-based x-ray spectromicroscopy used for the study of an atypical micrometric pigment in 16th century paintings.** *Analytical chemistry*, **79**(18):6988–6994, 2007. 50
- [94] J. DIK, K. JANSSENS, G. VAN DER SNICKT, L. VAN DER LOEFF, K. RICKERS, AND M. COTTE. **Visualization of a lost painting by Vincent van Gogh using synchrotron radiation based x-ray fluorescence elemental mapping.** *Analytical chemistry*, **80**(16):6436–6442, 2008. 50
- [95] T. TAKEDA, Y. ITAI, K. HYODO, M. ANDO, T. AKATSUKA, AND C. UYAMA. **Medical applications with synchrotron radiation in Japan.** *Journal of synchrotron radiation*, **5**(3):326–332, 1998. 51
- [96] P. SUORTTI AND W. THOMLINSON. **Medical applications of synchrotron radiation.** *Physics in medicine and biology*, **48**:R1, 2003. 51
- [97] G. MARGARITONDO. *Elements of synchrotron light: for biology, chemistry, and medical research.* Oxford University Press, USA, 2002. 51
- [98] F. CARROLL. **Tunable, monochromatic X-rays: An enabling technology for molecular/cellular imaging and therapy.** *Journal of cellular biochemistry*, **90**(3):502–508, 2003. 51

REFERENCES

- [99] M.C. BISTON, A. JOUBERT, J.F. ADAM, H. ELLEAUME, S. BOHIC, A.M. CHARVET, F. ESTÈVE, N. FORAY, AND J. BALOSSO. **Cure of Fisher rats bearing radioresistant F98 glioma treated with cis-platinum and irradiated with monochromatic synchrotron X-rays.** *Cancer research*, **64**(7):2317, 2004. 52
- [100] J. ROUSSEAU, C. BOUDOU, R.F. BARTH, J. BALOSSO, F. ESTÈVE, AND H. ELLEAUME. **Enhanced Survival and Cure of F98 Glioma-Bearing Rats following Intracerebral Delivery of Carboplatin in Combination with Photon Irradiation.** *Clinical Cancer Research*, **13**(17):5195–5201, 2007. 52
- [101] D. LI, K. IMASAKI, K. HORIKAWA, S. MIYAMOTO, S. AMANO, AND T. MOCHIZUKI. **Iodine transmutation through laser Compton scattering gamma rays.** *Journal of Nuclear Science and Technology*, **46**(8):831–835, 2009. 52
- [102] C. JIN-GEN, X. WANG, ET AL. **Transmutation of nuclear wastes using photonuclear reactions triggered by Compton backscattering photons at the Shanghai laser electron gamma source.** *Chinese Physics C*, **32**:677, 2008. 52
- [103] T. SUZUKI. **General formulae of luminosity for various types of colliding beam machines.** *KEK note*, pages 76–3. 53
- [104] ALESSANDRO VARIOLA, FABIAN ZOMER, EUGENE BULYAK, PETER GLADKIKH, VLADISLAV SKOMOROKHOV, TSUNEHIKO OMORI, AND JUNJI URAKAWA. **Luminosity optimization schemes in Compton experiments based on Fabry-Perot optical resonators.** *Phys. Rev. ST Accel. Beams*, **14**:031001, Mar 2011. 54
- [105] EUGENE BULYAK AND VLADISLAV SKOMOROKHOV. **Parameters of Compton x-ray beams: Total yield and pulse duration.** *Phys. Rev. ST Accel. Beams*, **8**:030703, Mar 2005. 54
- [106] I. CHAIKOVSKA, C. BRUNI, ET AL. **Effect of Compton Scattering on the Electron Beam Dynamics at the ATF Damping Ring.** In *Proc.*

-
- 2nd International Particle Accelerator Conference, San Sebastián, Spain*, number WEPC051, 2011. 54
- [107] J. LE DUFF. **Dynamics and acceleration in linear structures**. In *Proceedings of the CAS, CERN 94-01*, page 253, 1994. 55, 133
- [108] H. WIEDEMANN. *Particle accelerator physics*, **1**. Springer Verlag, 2003. 55
- [109] M. SANDS. **Physics of electron storage rings: an introduction**. Technical Report SLAC-R-121, Stanford Linear Accelerator Center, Calif., 1970. 56, 58
- [110] ZHIRONG HUANG AND RONALD D. RUTH. **Laser-Electron Storage Ring**. *Phys. Rev. Lett.*, **80**:976–979, Feb 1998. 57
- [111] A. PAPOULIS. *Probability, random variables, and stochastic processes*. McGraw-Hill, New York, third edition, 1991. 58
- [112] N. WAX. *Selected papers on noise and stochastic processes*. Dover Pubns, 2003. 58
- [113] PBO LAB[®]. **Version 3.0.2.0**. PBO Lab[®] is available from AccelSoft Inc., <http://www.ghga.com/accelsoft>. 61
- [114] K. YOKOYA. **User Manual of CAIN, version 2.40**, 2009. 62
- [115] T. AKAGI ET AL. **Production of gamma rays by pulsed laser beam Compton scattering off GeV-electrons using a non-planar four-mirror optical cavity**. *Journal of Instrumentation*, **7**:P01021, 2012. 62
- [116] M.S. DUBROVIN, R. CHEHAB, A. JEJCIC, AND J. SILVA. **Positron sources using channeling: a comparison with conventional targets**. *Particle Accelerators*, **59**:19–41, 1998. 71
- [117] J. BERINGER AND OTHERS (PARTICLE DATA GROUP). **Review of Particle Physics**. *Phys.Rev.*, **D86**:010001, 2012. 72, 73, 110
- [118] S. ECKLUND. **Positron target material tests**. *SLACCN-128*, 1981. 72
- [119] T. KAMITANI AND L. RINOLFI. **Positron production at CLIC** . Technical report, CLIC Note 465, March, 2001. 72

REFERENCES

- [120] S. MALOY ET AL. **SLC Target Analysis**. *LANL LA UR-01-1913*, 2001. 72
- [121] W. STEIN, A. SUNWOO, VK BHARADWAJ, DC SCHULTZ, AND JC SHEPPARD. **Thermal shock structural analyses of a positron target**. In *Particle Accelerator Conference, 2001. PAC 2001. Proceedings of the 2001*, **3**, pages 2111–2113. IEEE, 2001. 72
- [122] K. FLÖTTMANN. **ASTRA: A space charge tracking algorithm**. Astra available at <http://tesla.desy.de/~meykopff/>. 78
- [123] R. CHEHAB. **Positron sources**. In *Proceedings of the CAS, CERN 94-01*, pages 643–643, 1994. 78
- [124] F. BULOS, H. DESTAEBLER, S. ECKLUND, R. HELM, H. HOAG, H. LE BOUTET, HL LYNCH, R. MILLER, KC MOFFEIT, AND S.L.A. CENTER. **Design of a high yield position source**. *Nuclear Science, IEEE Transactions on*, **32**(5):1832–1834, 1985. 78
- [125] R. CHEHAB, G. LE MEUR, B. MOUTON, AND M. RENARD. **An adiabatic matching device for the Orsay linear positron accelerator**. *Nuclear Science, IEEE Transactions on*, **30**(4):2850–2852, 1983. 78
- [126] K. HALBACH AND RF HOLSINGER. **SUPERFISH-a computer program for evaluation of RF cavities with cylindrical symmetry**. *Particle Accelerators*, **7**(4):213–222, 1976. 79
- [127] CHENGHAI XU. *Intense Source of Positron Using Channeling Effect in Crystals*. PhD thesis, Laboratoire de l'Accélérateur Linéaire, Université Paris-Sud XI U.F.R Scientifique d'Orsay, 2012. 78
- [128] F. POIRIER, L. RINOLFI, A. VIVOLI, O. DADOUN, P. LEPERCQ, A. VARIOLA, ET AL. **Dynamics on the positron capture and accelerating sections of CLIC**. Technical report, CLIC Note 877, July, 2011. 80
- [129] J. A. CLARKE, I. R. BAILEY, E. BAYNHAM, V. BHARADWAJ, T.W. BRADSHAW, AND A. BRUMMITT. **The design of the positron source for the International Linear Collider**. In *SLAC-PUB-14686*. 84

-
- [130] L. RINOLFI, F. ZIMMERMANN, E. BULYAK, P. GLADKIKH, T. OMORI, J. URAKAWA, AND K. YOKOYA. **Superconducting positron stacking ring for CLIC**. In *Proc. 2nd International Particle Accelerator Conference, San Sebastián, Spain*, page TUPC053. IEEE, 2011. 84
- [131] T. AKAGI, M. KURIKI, S. MIYOSHI, TAKAHASHI T., ET AL. **Gamma-rays generation with 3D 4-mirror cavity for ILC polarized positron source**. In *Proc. International Particle Accelerator Conference, New Orleans, Louisiana, USA*, page WEPPD055. IEEE, 2012. 85
- [132] Y. K. WU. **Accelerator Physics Research and Light Source Development at Duke University**. *Proceedings of IPAC2010, Kyoto, Japan*. 87
- [133] HENRY R. WELLER, MOHAMMAD W. AHMED, HAIYAN GAO, WERNER TORNOW, YING K. WU, MOSHE GAI, AND RORY MISKIMEN. **Research opportunities at the upgraded HI γ S facility**. *Progress in Particle and Nuclear Physics*, **62**(1):257 – 303, 2009. 87
- [134] H. SHIMIZU ET AL. **Photon Generation by Laser-Compton Scattering Using an Optical Resonant Cavity at the KEK-ATF Electron Ring**. *Journal of the Physical Society of Japan*, **78**(7):4501, 2009. 87
- [135] MIYOSHI S. ET AL. **Photon generation by laser-Compton scattering at the KEK-ATF**. *Nuclear Instruments and Methods in Physics Research Section A*, 2010. 87, 95
- [136] F. HINODE ET AL. **ATF Accelerator Test Facility Design and Study Report No. 4**. KEK, Tsukuba, Japan, 1995. <http://lcdev.kek.jp/ATF/Pub/KEK-I-95-4.pdf>. 87, 88
- [137] H. HAYANO ET AL. **Accelerator Test Facility Study Report JFY 19996-1999**. KEK, Tsukuba, Japan, **KEK Internal report 2000-6**, 2000. 88
- [138] K. KUBO ET AL. **Extremely Low Vertical-Emittance Beam in the Accelerator Test Facility at KEK**. *Phys. Rev. Lett.*, **88**:194801, Apr 2002. 88

REFERENCES

- [139] P. BAMBADE ET AL. **Present status and first results of the final focus beam line at the KEK Accelerator Test Facility.** *Phys. Rev. ST Accel. Beams*, **13**(4):042801, Apr 2010. 89
- [140] TAKASHI NAITO, HITOSHI HAYANO, KIYOSHI KUBO, SHIGERU KURODA, TOSHIYUKI OKUGI, ET AL. **Multi-bunch Beam Extraction using Strip-line Kicker at KEK-ATF.** *Conf.Proc.*, **C100523:WEOBMH02**, 2010. 89
- [141] T.NAITO ET AL. **Timing system for Multi-Bunch/Multi-Train operation at ATF-DR.** *KEK, Tsukuba, Japan, KEK Preprint 99-144*, 1999. 89
- [142] C. BRIEGEL ET AL. **Status of the ATF Damping Ring BPM Upgrade Project.** Technical report, SLAC National Accelerator Laboratory (SLAC), 2011. 90
- [143] P. FORCK, P. KOWINA, AND D. LIAKIN. **Beam position monitors.** *CERN Accelerator School on Beam Diagnostics*, pages 187–228, 2008. 90
- [144] N. EDDY ET AL. **High Resolution BPM Upgrade for the ATF Damping Ring at KEK.** *arXiv preprint arXiv:1209.4569*, 2012. 91
- [145] More information available available at <http://www.onefive.com/femtosecond.htm>. 93
- [146] J. LIMPERT, F. ROSER, S. KLINGEBIEL, T. SCHREIBER, C. WIRTH, T. PESCHEL, R. EBERHARDT, AND A. TUNNERMANN. **The rising power of fiber lasers and amplifiers.** *Selected Topics in Quantum Electronics, IEEE Journal of*, **13**(3):537–545, 2007. 93
- [147] T. EIDAM, S. HANF, E. SEISE, T.V. ANDERSEN, T. GABLER, C. WIRTH, T. SCHREIBER, J. LIMPERT, AND A. TUNNERMANN. **Femtosecond fiber CPA system emitting 830 W average output power.** *Optics letters*, **35**(2):94–96, 2010. 93
- [148] J. LIMPERT, F. ROSER, D.N. SCHIMPF, E. SEISE, T. EIDAM, S. HADRICH, J. ROTHHARDT, C.J. MISAS, AND A. TUNNERMANN. **High repetition rate**

-
- gigawatt peak power fiber laser systems: challenges, design, and experiment.** *Selected Topics in Quantum Electronics, IEEE Journal of*, **15**(1):159–169, 2009. 93
- [149] A. TÜNNERMANN, T. SCHREIBER, AND J. LIMPert. **Fiber lasers and amplifiers: an ultrafast performance evolution.** *Applied optics*, **49**(25):F71–F78, 2010. 94
- [150] I. PUPEZA, T. EIDAM, ET AL. **Power scaling of a high-repetition-rate enhancement cavity.** *Optics letters*, **35**(12):2052–2054, 2010. 95
- [151] V. BRISSON, R. CIZERON, R. CHICHE, E. CORMIER, ET AL. **High finesse Fabry-Perot cavities in picosecond regime.** *Nuclear Instruments and Methods in Physics Research Section A*, **608**:S75 – S77, 2009. 95
- [152] N. FALLETTO, M. AUTHIER, M. BAYLAC, M. BOYER, F. BUGEON, ET AL. **Compton scattering off polarized electrons with a high-finesse Fabry-Perot Cavity at JLab.** *Nuclear Instruments and Methods in Physics Research Section A*, **459**(3):412 – 425, 2001. 95
- [153] S. BAUDRAND, M. BOUCHEL, ET AL. **A high precision Fabry-Perot cavity polarimeter at HERA.** *Journal of Instrumentation*, **5**(06):P06005, 2010. 95
- [154] K. SAKAUE, M. WASHIO, S. ARAKI, ET AL. **Observation of pulsed x-ray trains produced by laser-electron Compton scatterings.** *Review of Scientific Instruments*, **80**(12):123304–123304, 2009. 95
- [155] F. ZOMER, Y. FEDALA, N. PAVLOFF, V. SOSKOV, AND A. VARIOLA. **Polarization induced instabilities in external four-mirror Fabry-Perot cavities.** *Applied optics*, **48**(35):6651–6661, 2009. 95
- [156] R.W.P. DREVER, J.L. HALL, F.V. KOWALSKI, J. HOUGH, G.M. FORD, A.J. MUNLEY, AND H. WARD. **Laser phase and frequency stabilization using an optical resonator.** *Applied Physics B: Lasers and Optics*, **31**(2):97–105, 1983. 97

REFERENCES

- [157] S. MIYOSHI. *Development of polarized positron source by laser Compton scattering with optical resonant cavity*. PhD thesis, Graduate School of Advanced Sciences of Matter, Hiroshima University, 2011. 103, 110
- [158] P. SCHOTANUS, G. STAM, E. GERRITSE, B. UTTS, AND B. BRIAUX. **Scintillation detectors**. *SAINT-GOBAIN, CRISMATEC catalogue*, 1992. 103, 104
- [159] MR FARUKHI AND CF SWINEHART. **Barium fluoride as a gamma ray and charged particle detector**. *Nuclear Science, IEEE Transactions on*, **18**(1):200–204, 1971. 104
- [160] M. LAVAL, M. MOSZYŃSKI, R. ALLEMAND, E. CORMORECHE, P. GUINET, R. ODRU, AND J. VACHER. **Barium fluoride–inorganic scintillator for subnanosecond timing**. *Nuclear Instruments and Methods in Physics Research*, **206**(1):169–176, 1983. 104
- [161] P. DORENBOS, R. VISSER, CWE VAN EIJK, J. VALBIS, AND NM KHAIDUKOV. **Photon yields and decay times of cross luminescence in ionic crystals**. In *Nuclear Science Symposium and Medical Imaging Conference, 1991., Conference Record of the 1991 IEEE*, pages 162–166. IEEE, 1991. 104
- [162] S. AGOSTINELLI ET AL. **GEANT4: A simulation toolkit**. *Nucl. Instrum. Meth.*, **A506**:250–303, 2003. 105
- [163] **Bialkali UV photomultiplier: H3378-51 (R3377), Hamamatsu Photonics K.K., Hamamatsu, Japan**. More information available available at <http://sales.hamamatsu.com/en/products/electron-tube-division/detectors/photomultiplier-tubes/part-r3377.php>. 105
- [164] R. BRUN AND F. RADEMAKERS. **Root—an object oriented data analysis framework**. *Nuclear Instruments and Methods in Physics Research Section A*, **389**(1-2):81–86, 1997. 105
- [165] **EPICS: Experimental Physics and Industrial Control System**. EPICS available at <http://epics.aps.anl.gov/epics/>. 108
- [166] L. LANDAU. **On the energy loss of fast particles by ionisation**. *J. Phys. USSR*, **8**(4):201, 1944. 110

REFERENCES

- [167] D. GROOM. **Atomic and Nuclear Properties of Materials. Particle Data Book.** <http://pdg.lbl.gov/2011/AtomicNuclearProperties/>. 111
- [168] MATLAB[®]. **Version 7.10.0.499 (R2010a).** MATLAB[®] available from The MathWorks Inc., <http://www.mathworks.com>. 116
- [169] JOHN W. EATON. *GNU Octave Manual.* Network Theory Limited, 2002. 116